Inaugural dissertation

for

obtaining the doctoral degree

of the

Combined Faculty of Mathematics, Engineering and Natural Sciences

of the

Ruprecht - Karls - University

Heidelberg

Presented by

Daniela Kocher, MSc

Born in Tamsweg, Austria

Oral Examination: 13.05.2024

Exploring molecular mechanisms involved in tumor rebound growth after MAPKi withdrawal in pLGG

Referees: Prof. Dr. Peter Angel

Prof. Dr. med. Till Milde

Declaration

I hereby declare that I have written this dissertation myself, using only the cited literature and sources.

I hereby declare that I have not applied to be examined at any other institution, nor have I used the dissertation in this or any other form at any other institution as an examination paper, nor submitted it to any other faculty as a dissertation.

Parts of the text, figures and tables in this dissertation are adapted from Kocher *et al.*, submitted to a peer-reviewed journal and currently under review, and were originally written and generated by myself. Any text not written by myself is indicated as such and any methods not performed by myself are indicated.

Heidelberg, 15.02.2024

Daniela Kocher

Acknowledgements

I am very grateful to all the people who have supported me during the last years and have contributed to the completion of my PhD:

Prof. Dr. med. Olaf Witt, for creating a collaborative atmosphere in our department, his scientific input, and making sure to keep the translational aspects of our projects in mind.

Prof. Dr. med. Till Milde and Dr. Romain Sigaud, the best supervisors I could've asked for. You showed me what it means to be a good scientist and I am grateful for the guidance and mentorship I received from both of you.

Till, thank you for giving me the chance to work in your group and your continuous support during my PhD. You always made sure that I didn't lose focus and taught me what is important for developing and finishing a successful project.

Romain, thank you for your constant support through all the highs and lows of my PhD and for believing in me. You always took me seriously and encouraged me to develop my own ideas while making sure I did not go too far beyond the scope of my project. You taught me how to ask the right questions and showed me that I am capable of more than I thought.

I would also like to thank the members of my TAC committee for their advice and critical feedback on my project: Prof. Dr. Peter Angel, who also kindly agreed to be the first examiner of my thesis; and Prof. Dr. Tilman Brummer for sharing his expertise.

Prof. Dr. Sergio Acebrón and Prof. Dr. Stefan Wiemann for agreeing to participate in my defense committee.

I would like to express my gratitude to our collaborators who contributed to the completion of this project: Prof. Dr. Juan Pedro Martinez-Barbera, Dr. Lei Cao and Dr. Romain Guiho for providing their expertise and generating valuable in vivo samples for my project. PD. Dr. Stefan Pusch, David Vonhören and Dr. Julia Zaman for providing their expertise and assistance in generating the phospho-/proteomics data. Prof. Dr. med. Andreas von Deimling for giving us access to the mass spectrometers in his department. Dennis Friedel for processing the raw

MS data. Dr. Daniel Picard for sharing his insights on RNAseq data filtering and analysis. Dr. Sebastian Halbach and Melanie Langhammer for their input and performing the Luminex-based multiplex assay for my project. Dr. David Jones for providing equipment and critical feedback. Dr. Kendra Maass and Johanna Rettenmeier for providing input and expertise. Finally, thanks to all our collaborators within the EVEREST consortium, at the DFCI and the KiTZ for their feedback and input to my project.

A big thank you to all members of B310, current and former, for making my time in the department a fun experience, inside and out the lab, and supporting me in various ways: Ginny, Isabel, Florian, Nora, Yvonne, Anna K., Jonas, Pauline, Leo, Carina, Raquel, Dani, Simon, Johanna V., Diren, Anna La., Johanna B., Ina O., Heike, Sonja H., Simay, Anna Lo., Lisa, Marta, Kyriaki, Coco, Alex, Aileen, Marko, Clarissa, Johannes, Charlotte, Till S., Michael, Ina S., Lea, Sara, Olga, Eugene, Sonja B., Sina, Yannick, Natja, Elisabeth and Nicola. Ginny, who helped me get settled with all PhD related matters when I started and always shared her advice. Isabel, for helping me to get started in the lab and all the fun moments we had. Florian, for always listening and knowing what to say when things did not go as planned. Nora, for the great conversations and spontaneous dinner dates. Yvonne, Carina, Dani, Johanna B. and Anna La. for their support in the lab and making sure things in the lab run smoothly. Anna K., for always having an open ear and fun moments at the Happy Hours. Jonas, for his critical feedback and great BBQs. Pauline, for brightening even dull work days with her cheerful nature. Leo, for funny moments in the lab. Raquel, for her organizational skills and sharing a bit of Brazilian culture with us. Sonja, Simay, Anna Lo., Marta, Kyriaki, Lisa and Coco for fun coffee breaks or afterwork drinks. Natja, Elisabeth and Nicola for their help with all administrative problems.

Thank you to all my friends, in Heidelberg and beyond, who have been there for me and supported me on my way and made the last years a memorable experience.

Finally, I would like to thank my family for their unwavering support. I would not be where I am today without them.

Summary

Pediatric low-grade gliomas (pLGGs) are the most common primary brain tumors in children and are almost exclusively driven by alterations in the mitogen-activated protein kinase (MAPK) pathway, most commonly *BRAF* fusions and *BRAF*^{V600E} point mutations. This makes pLGGs a fitting candidate for targeted therapies using MAPK inhibitors (MAPKi), which have shown promising results in clinical trials. This led to the FDA-approval of dabrafenib and trametinib combination as front-line treatment for *BRAF*^{V600E} driven pLGGs. However, despite the efficacy of MAPKi treatment, a subset of patients experiences a rapid tumor regrowth upon treatment stop, also referred to as rebound growth, which constitutes a significant clinical challenge.

To model rebound growth *in vitro*, based on viable cell counts in response to MAPKi treatment and withdrawal, four patient-derived pLGG models were tested. Following, a multi-omics dataset of the rebound model, encompassing different MAPKi withdrawal timepoints, was generated using RNA sequencing and LC-MS/MS-based phospho-/proteomics. Using this data set, I identified putative rebound growth driving mechanisms, which were further validated *in vitro* and *in vivo*.

Of the tested models, BT-40 (*BRAF*^{V600E}, *CDKN2A/B*del) showed rebound growth, characterized by faster cell regrowth after MAPKi withdrawal compared to standard-of-care chemotherapy, thereby mimicking what is observed in patients. Using this model, I observed MAPK pathway reactivation within hours after withdrawal, associated with a transient overactivation of key MAPK molecules on transcriptional (e.g. *FOS*) and phosphorylation (e.g. pMEK) levels. Furthermore, AKT activity and expression and secretion of cytokines (in particular CCL2, CX3CL1, CXCL10 and CCL7) were increased upon MAPKi treatment and maintained during early withdrawal (until 6-24 h). While neither increased AKT activity nor cytokine expression affected rebound growth in a tumor cell intrinsic manner, upregulated cytokines mediated increased attraction of microglia cells during MAPKi treatment and withdrawal. Importantly, MAPK pathway reactivation during rebound growth and increased

expression of *CX3CL1* and *CXCL10* upon MAPKi treatment were also observed *in vivo* using the BT-40 orthotopic xenograft model.

In summary, this study suggests rapid MAPK reactivation as a tumor cell intrinsic rebound driving mechanism and modulation of MAPK activity during treatment withdrawal may be a possible strategy to target rebound growth, which should be further investigated. Furthermore, I could show increased microglia attraction, mediated by cytokines induced upon MAPKi treatment, suggesting a possible role of the immune microenvironment, in particular microglia cells, during MAPKi treatment and withdrawal, which warrants further investigation.

Zusammenfassung

Pädiatrische niedriggradige Gliome (pLGG) sind die häufigsten pädiatrischen Hirntumore und werden hauptsächlich von Mutationen im „mitogen-actived potein kinase (MAPK)“-Signalweg, am häufigsten *BRAF*-Fusionen und *BRAF*^{V600E}-Punktmutationen, angetrieben. Dadurch sind pLGGs ein geeigneter Kandidat für zielgerichtete Therapien mit MAPK-Inhibitoren (MAPKi), die in klinischen Studien vielversprechende Ergebnisse gezeigt haben. Dies führte zur FDA-Zulassung der Kombination aus Dabrafenib und Trametinib als Erstlinienbehandlung für pLGGs mit *BRAF*^{V600E} Mutation. Trotz der Wirksamkeit der MAPKi Behandlung erfährt ein Teil der Patienten, die während der Behandlung auf die Inhibitoren angesprochen haben, innerhalb kurzer Zeit ein Rezidiv. Dieses kurzfristige, schnelle, erneute Tumorwachstum wird auch als Rebound-Wachstum bezeichnet und stellt ein signifikantes klinisches Problem dar.

Um das Rebound-Wachstum *in vitro* während und nach MAPKi Behandlung zu modellieren, wurden vier Zellmodelle, die von humanen Tumoren etabliert wurden, mittels Zellzahlzählungen getestet. Anschließend wurde ein Multi-Omics Datensatz mittels RNA-Sequenzierung und LC-MS/MS-basierter Phospho-/Proteomik von dem Rebound-Modell erstellt. Basierend auf diesem Datensatz wurden Mechanismen identifiziert, die möglicherweise eine Rolle während des Rebound-Wachstums spielen könnten, und anschließend *in vitro* und *in vivo* validiert.

Von den getesteten Modellen zeigten BT-40 Zellen (*BRAF*^{V600E}, *CDKN2A/B*del) ein Rebound-Wachstum, welches durch ein früheres, erneutes Zellwachstum nach Absetzen der MAPKi Behandlung im Vergleich zu Chemotherapeutika gekennzeichnet war und somit die Beobachtungen in Patienten wiederspiegelt. Auf molekularer Ebene zeigte dieses Model eine Reaktivierung des MAPK-Signalwegs innerhalb weniger Stunden nach Behandlungsstop, welches mit einer transienten Überaktivierung zentraler MAPK-Elemente auf transkriptioneller (z.B. *FOS*) und posttranslationaler (z.B. MEK-Phosphorylierung) Ebene einherging. Zusätzlich führte MAPKi Behandlung zu einer erhöhten Aktivität des AKT-Signalweges sowie einer erhöhten Expression und Sekretion von Zytokinen, insbesondere CCL2, CX3CL1, CXCL10

und CCL7, welche auch bis 6-24 Stunden nach Behandlungsstop erhalten blieben. Weder die erhöhte AKT-Aktivität noch erhöhte Zytokinexpression beinflussten das Rebound-Wachstum auf eine tumorzellintrinsische Weise. Erhöhte Zytokinsekretion während und nach MAPKi Behandlung führte jedoch zu einer erhöhten Anziehung von Mikrogliazellen. Die schnelle Reaktivierung des MAPK-Signalwegs während des Rebound-Wachstums sowie die erhöhte Expression von *CX3CL1* und *CXCL10* während MAPKi Behandlung konnten zudem *in vivo* in einem orthotopen BT-40-Xenotransplantationsmodell nachgewiesen werden.

Zusammenfassend zeigen diese Daten eine schnelle Reaktivierung des MAPK-Signalweges als potentiellen, tumorzellintrinsischen, Rebound-antreibenden Mechanismus. Dies deutet darauf hin, dass Modulation der MAPK-Aktivität nach Behandlungsstop eine mögliche Strategie sein könnte, um das Rebound-Wachstum zu verhindern, die weiter untersucht werden sollte. Darüber hinaus konnte ich nachweisen, dass die erhöhte Zytokinproduktion, induziert durch die MAPKi Behandlung, zu einer erhöhten Anziehung von Mikrogliazellen führt. Dies legt nahe, dass Immunzellen, insbesondere Mikrogliazellen, innerhalb des Tumor-Mikromillieus eine Rolle während der MAPKi-Behandlung sowie während des Rebound-Wachstums spielen, welche in zukünftigen Studien weiter untersucht werden sollte.

Abbreviations

ACKR4	Atypical chemokine receptor 4
ACTB	Beta actin
AKT	Proteinkinase B
AKTi	AKT inhibitor
AP-1	Activator protein 1
APS	Ammonium persulfate
ATF	Activating transcription factor
ATIS	antiangiogenic therapy-induced secretome
ATP	Adenosintriphosphat
AUC	Area under the curve
AUC	Area under the curve
BATF	Basic Leucine Zipper ATF-Like Transcription Factor
BCA	Bicinchoninic acid
BRAF	v-Raf murine sarcoma viral oncogene homolog B
BSA	Bovine serum albumin
CCNU	Chlorethyl-Cyclohexyl-Nitroso-Urea
CD4+	Cluster of differentiation 4
CD8+	Cluster of differentiation 8
CDK	Cyclin-dependant kinase
CDK	Cyclin-dependant kinase
CDKN2A/B	Cyclin dependent kinase inhibitor 2A/B
cDNA	Coding desoxyribonucleic acid
c-Fos	Fos proto-oncogene
c-Jun	Jun proto-oncogene
CM	Conditioned media
C_{max}	Maximum plasma concentration
CNS	Central nervous system
CO_2	Carbon dioxide
CRAF	RAF proto-oncogene serine/threonine-protein kinase
CRC	Colorectal cancer
CRH	Corticotropin releasing hormone
CSF-1R	Colony-stimulating factor 1 receptor
Ct	Cycle threshold
DA	Diffuse astrocytoma
DAPI	4′,6-Diamidin-2-phenylindol
ddH2O	Double-distilled water
DLGNT	Diffuse leptomeningeal glioneuronal tumor
DMSO	Dimethyl sulfoxide
DNA	Deoxyribonucleic acid
DTT	Dithiothreitol
DUSP	Dual-specific phosphatase
DUSP6	Dual-specific phosphatase 6
EBI3	Epstein-Barr virus induced gene 3
ECL	Enhance chemiluminescent

EDTA	Ethylenediaminetetraacetic Acid
EGF	Epidermal growth factor
EGFR	Epidermal growth factor receptor
Elk-1	ETS Like-1 protein
ERK	Extracellular regulated kinase
ETS	E26 transformation-specific
EV	Extracellular vesicle
FACS	Fluorescence-activated cell sorting
FAM131B	Family With Sequence Similarity 131 Member B
FCS	Fetal calf serum
FDA	Food and drug administrataio
FDR	False discovery rate
FGFR	Fibroblast growth factor receptor
FOS	Fos proto-oncogene
FosB	FBJ murine osteosarcoma viral oncogene homolog B
FPKM	Fragments Per Kilobase per Million mapped fragments
Fra1	Fos-related antigen 1
Fra2	Fos-related antigen 2
GDP	Guanosindiphosphat
GFP	Green fluorescent protein
GG	Ganglioglioma
GO	Gene ontology
GPCR	G-protein coupled receptor
Grb2	Growth factor receptor-bound protein 2
GSK3a/b	Glycogen synthase kinase-3 alpha/beta
GTP	Guanosintriphosphat
H_2O	Water
HCl	Hydrogen chloride
hiPSC	Human induced pluripotent stem cell
HPLC	High-performance liquid chromatography
HRP	Horseradish peroxidase
HSP90	Heat-shock protein 90
IAA	Iodoacetamide
IC	Inhibitory concentration
IC50	50% inhibitory concentration
IC75	75% inhibitory concentration
IC_{max}	Maximal inhibitory concentration
ICI	Immune checkpoint inhibition
IgG	Immunoglobulin G
IL1a	Interleukin-1 alpha
IL1b	Interleukin-1 beta
IL8	Interleukin-8
IL9	Interleukin-9
iPSC	Induced pluripotent stem cell
JAK	Janus kinase
JNK	c-Jun N-terminal kinase

JUN	Jun proto-oncogene
Kml	Longitudinal k-means clustering
KSEA	Kinase-substrate enrichment analysis
LC	Liquid chromatography
LC-MS/MS	Liquid chromatography–mass spectrometry/mass spectrometry
LF PVDF	Low-fluorescence polyvinylidenfluorid
LIF	Leukemia inhibitory factor
Log2FC	Log2-transformed fold-change
MAPK	Mitogen-activated protein kinase
MAPKi	MAPK inhibitor
MEK	Mitogen-activated protein kinase kinase
MEKi	MEK inhibitor
MET	Hepatocyte growth factor receptor
METi	MET inhibitor
MM	Minimum media
MPAS	MAPK pathway activity score
mRNA	Messenger ribonucleic acid
MS	Mass spectrometry
MSS	MAPK inhibitor sensitivity score
mTOR	Mammalian target of rapamycin
mTORi	mTOR inhibitor
MYB	Avian myeloblastosis viral oncogene homolog
MYBL1	MYB proto-oncogene like 1
NaCl	Sodium chloride
NaOH	Sodium hydroxide
NEAA	Non-essential amino acids
neuAB	Neutralizing antibody
NF1	Neurofibromin 1
NF-kB	Nuclear factor kappa-light-chain-enhancer of activated B cells
NGS	Next-generation sequencing
NK cells	Natural killer cells
NSC	Neural stem cell
NSG	NOD scid gamma
O/N	Overnight
OIS	Oncogene-induced senescence
OPG	Optic pathway glioma
OR	Overall response
ORR	Objective response rate
OS	Overall survival
OTP	One-touch pipeline
PA	Pilocytic astrocytoma
PAK	Serine/threonine-protein kinase
PARP	Poly (ADP-ribose) polymerase
PBS	Phosphate-buffered saline
PC	Principal component
PCA	Principal component analysis

PCR	Polymerase chain reaction
PD-1	Programmed cell death protein 1
PD-L1	Programmed death-ligand 1
PE	Phycoerythrin
PF4V1	Platelet factor 4 variant 1
PFS	Progression-free survival
PI	Propidium iodine
PI3K	Phosphoinositide 3-kinases
PI3Ki	PI3K inhibitor
PIM	Proto-oncogene serine/threonine-protein kinase
PK	Pharmakokinetics
pLGG	Pediatric low-grade glioma
PLNTY	Polymorphus low-grade neuroepithelial tumor of the young
PMID	Pubmed ID
PPB	Plasma-protein-binding
pRb	Retinoblastoma protein
PROTAC	Proteolysis targeting chimera
PTM-SEA	Post-translational modification signature enrichment analysis
PXA	Pleomorphic xanthoastrocytomas
qPCR	Quantitative polymerase chain reaction
RAF	Proto-oncogene serine/threonine-protein kinase
Rag1	Recombination activating gene 1
RAS	Rat sarcoma virus
Rcf	Relative centrifugal force
RNA	Ribonucleic acid
RNAseq	RNA sequencing
ROCK	Rho kinase
Rpm	Rounds per minute
RSK	p90 ribosomal S6 kinase
RT	Room temperature
RTK	Receptor tyrosine kinase
RT-qPCR	Reverse-transcription quantitative polymerase chain reaction
S6K1	Ribosomal protein S6 kinase beta-1
SASP	Senescence-associated secretory phenotype
SD	Standard deviation
SDC	Sodium deoxycholate
SDC4	Syndecan-4
SDS	Sodium dodecyl sulfate
SDS-PAGE	SDS polyacrylamide gel electrophoresis
SEGA	Subependymal giant cell astrocytoma
SMAD2/3	Mothers against decapentaplegic homolog 2/3
SOC	Standard-of-care
Sos	Son of sevenless
SPRY	Sprouty
ssGSEA	Single-sample gene set enrichment analysis
STAT	signal transducer and activator of transcription

SV40-TAg	Simian Vacuolating Virus 40 large T antigen
TBP	TATA-binding protein
TBS	Tris-buffered saline
TBS-T	Tris-buffered saline with tween
TCEP/HCL	Tris-(2-carboxyethyl)-phosphin hydrogen chloride
TEMED	Tetramethylethylenediamine
TFA	Trifluoroacetic acid
TGF-beta	Transforming growth factor beta
TiO2	Titanium dioxide
TME	Tumor microenvironment
TNF	Tumor necrosis factor
TNFSF15	TNF superfamily member 15
TPCV	Thioguanine, procarbazine, CCNU and vincristine
TPM	Transcript per million
VCR	Vincristine
VEGFR	Vascular endothelial growth factor receptor
WB	Western blot
wd	Withdrawal
WHO	World health organization
WT	Wildtype

Table of contents

List of Figures

List of Tables

1 Introduction

1.1 Pediatric low-grade glioma

1.1.1 Clinical information

In 2020, approximately 26 000 children (<19 years) were diagnosed with cancer in Europe.[1] After leukemias, which account for approx. one third of cancer diagnosis, central nervous system (CNS) tumors are the most common tumors diagnosed in children (approx. 20% of all patients with cancer).[2,3] Amongst CNS tumors, pediatric low-grade gliomas (pLGGs) are the most common primary brain tumors, accounting for approx. 25-30% of all pediatric brain tumors (Figure 1).[4]

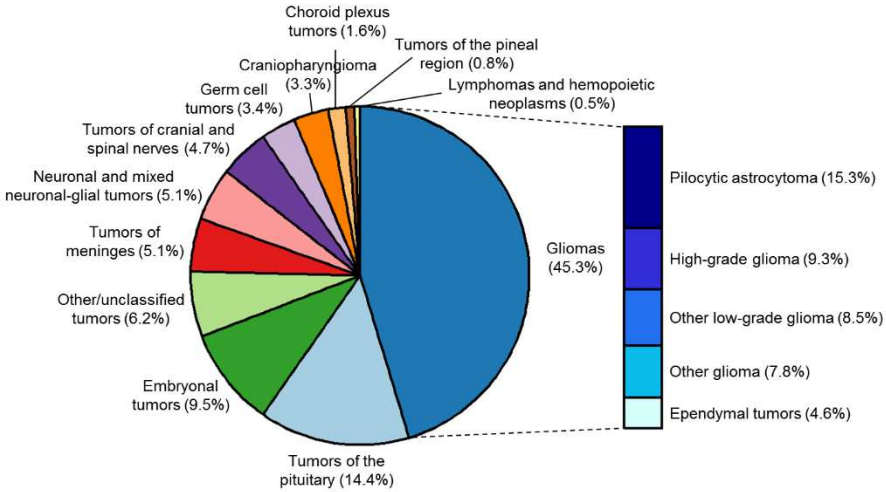

Figure 1 Distribution of brain and CNS tumor entities by histology
age: 0-19 years. CBTRUS Childhood and Adolescent Report: US Cancer Statistics (2014–2018). Adapted from Ostrom *et al.* 2022[4]

pLGGs are a diverse group of WHO grade 1-2 glial and glioneuronal tumors.[5,6] Tumor types include relatively circumscribed tumors such as pilocytic astrocytomas (PAs) or pleomorphic xanthoastrocytomas (PXAs), as well as more infiltrative tumors such as diffuse astrocytoma (DA) or angiocentric glioma.[5,6] A full list of tumor types belonging to pLGGs can be found in Table 1. pLGG tumors can arise throughout the CNS, but age-specific locations are observed.[7] In infants (< 3 years) and adolescents (12-15 years) cortical pLGGs are common, while in children (3-12 years) pLGGs commonly occur in the posterior fossa or the optic nerve.[7]

Table 1 2021 WHO classification of pediatric low-grade glioma and glioneuronal tumors
adapted from Louis *et al.* 2021[5] and Manoharan *et al.* 2023[6]

Pediatric-type diffuse low-grade gliomas	Diffuse astrocytoma, MYB- or MYBL1-altered
	Angiocentric glioma
	Polymorphous low-grade neuroepithelial tumor of the young (PLNTY)
	Diffuse low-grade glioma, MAPK pathway-altered
Circumscribed astrocytic gliomas	Pilocytic astrocytoma (PA)
	Pleomorphic xanthoastrocytoma (PXA)
	Subependymal giant cell astrocytoma (SEGA)
	Choroid glioma
Glioneuronal and neuronal tumors	Ganglioglioma (GG)
	Desmoplastic infantile ganglioglioma/ desmoplastic infantile astrocytoma
	Dysembryoplastic neuroepithelial tumor
	Diffuse glioneuronal tumor with oligodendroglioma-like features and nuclear clusters
	Rosette-forming glioneuronal tumor
	Papillary glioneuronal tumor
	Myxoid glioneuronal tumor
	Diffuse leptomeningeal glioneuronal tumor (DLGNT)
	Gangliocytoma
	Multinodular and vacuolating neuronal tumor
	Dysplastic cerebellar gangliocytoma (Lhermitte-Duclos disease)
	Central neurocytoma
	Extraventricular neurocytoma
	Cerebellar liponeurocytoma

Pediatric low-grade gliomas are very distinct from adult low-grade gliomas. Transformation into high-grade tumors, as commonly seen in adults, is rare for pLGGs, which appear very stable over time, and seem to become quiescent with transition to adulthood.[8,9] A study of long-term

survivors that reached adult-hood showed 93% 30-year overall survival (OS) for these patients.[8]

While the outcome for this type of tumors is very favorable for overall survival (15-year OS from diagnosis: approx. 90%),[10,11] progression-free survival is considerably lower (15-year PFS: approx. 50%)[10,11] (Figure 2), and in particular dependent on surgical resection status.[10] In cases where gross-total resection was possible, 10-year PFS reaches 86%, while in cases with less than gross-total or no resection it only reaches 43% or 27% respectively.[10] Therefore, patients often undergo multiple lines of therapies and suffer from complications and morbidity caused by the tumor and/or the treatment,[10] warranting the need for more effective therapies, with a focus on improving quality of life.

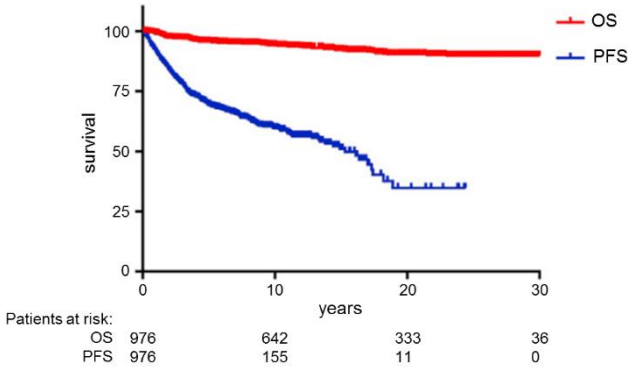

Figure 2 Overall (OS) and progression-free survival (PFS) of pLGG cohort
adapted from Ryall *et al.* 2020[11]

1.1.2 Genetic background and molecular features

pLGGs are almost exclusively driven by alterations in the extracellular regulated kinase mitogen-activated protein kinase (ERK/MAPK) pathway (Figure 3).[7] The most common alterations are structural rearrangements affecting BRAF and KIAA1549 (*KIAA:BRAF* fusion; ~45%),[11–14] most commonly observed in PAs.[7] This rearrangement results in fusion of the N'-terminus of the KIAA1549 protein and C'-terminus of the BRAF protein, containing the kinase domain.[15] The negative regulatory domain of BRAF, located at the N'-terminus is lost, thereby leading to

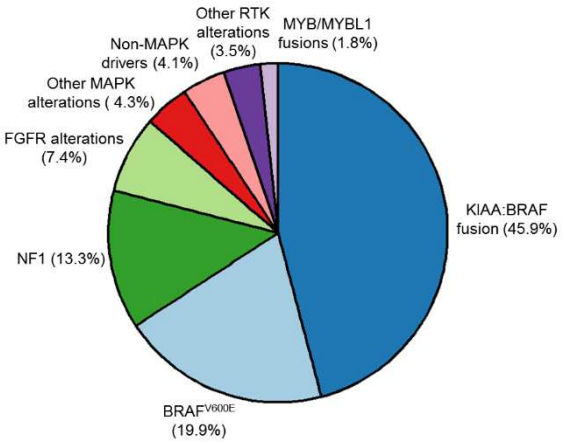

Figure 3 Genetic alterations in pLGGs
n=1192 tumor samples. Data was taken from Ryall *et al.* 2020,[11] Shapiro *et al.* 2023,[12] Hardin *et al.* 2023[13] and Sturm *et al.* 2023[14]

constitutive activation of BRAF inducing increased MAPK signaling.[15,16] Fusions of BRAF with other proteins have been described as well, although appear to arise less frequently (e.g. *FAM131B:BRAF*).[17,18] Another common alteration found in pLGGs are *BRAF*^{V600E} mutations (10-20%)[11–14] leading to constitutive activation of the kinase, which are most commonly observed in PXAs or gangliogliomas (GGs),[7] associated in the former with additional loss of *CDKN2A/B*.[5] Some studies suggest that *BRAF*^{V600E}-driven tumors have a worse outcome compared to BRAF-fusion driven tumors, in particular if associated with a co-occurring *CDKN2A/B* deletion (13-25% of all *BRAF*^{V600E}-driven pLGGs).[11,19] With increasing numbers of pLGG samples subjected to genomic analysis, further genomic alterations have been described, such as receptor tyrosine kinase (RTK) alterations (most commonly FGFR alterations and fusions) or MYB/MYBL1 fusions.[7] In addition to purely somatic driver alterations, genetic predisposition syndromes have been observed in pLGG patients as well. Most commonly, inactivating NF1 alterations (which can arise also sporadically) are observed, especially in optic pathway gliomas (OPGs).[7,20]

1.1.3 MAPK pathway

1.1.3.1 MAPK pathway regulation

The mitogen-activated protein kinase (MAPK) pathway plays an important role in the regulation of many molecular processes, such as cell proliferation, differentiation or survival, and can be activated by several stimuli (e.g. growth factors, cytokines or stress inducers).[21] Different groups of MAPKs are known: extracellular signal-regulated kinase (ERK)1/2, c-Jun N-terminal kinase (JNK), p38 and ERK5.[21] Additionally, kinases sharing similarities with components of the MAPK pathway have been described (ERK3/4 and ERK7/8), however their exact signaling mechanism is not fully understood yet.[22]

The MAPK/ERK pathway (Figure 4) is most commonly activated by growth factors binding to RTKs.[23] Activation of the receptor leads to recruitment of adapter proteins (e.g. Grb2) and upstream activators (e.g. Sos) ultimately leading to the activation of RAS, a GTPase.[24–27] RAS then activates the cascade of MAP kinases through activation of RAF,[28,29] which

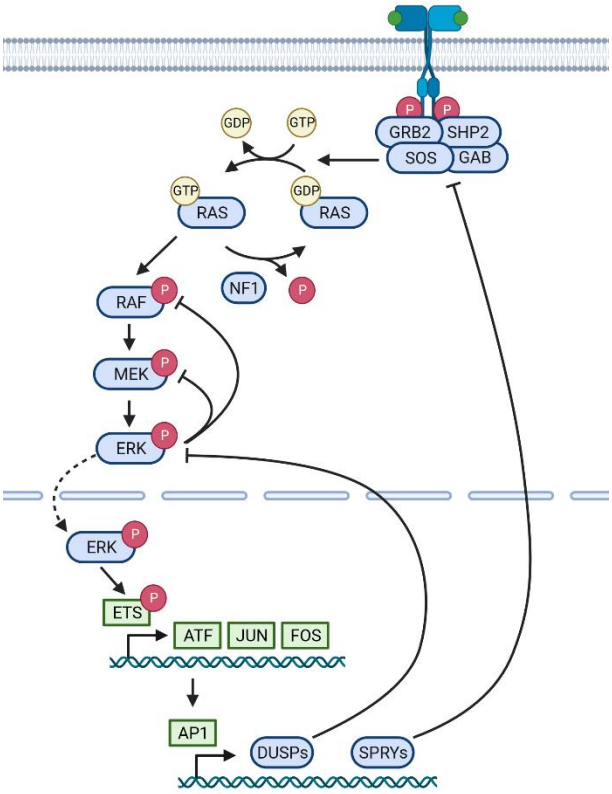

Figure 4 MAPK/ERK signaling pathway
created using BioRender.com

phosphorylates and activates MEK1/2[30] which in turn phosphorylates and activates ERK1/2[31]. In the cytoplasm, active ERK phosphorylates several target proteins,[32] including the p90 ribosomal S6 kinase (RSK).[33] Once translocated to the nucleus, ERK activates several transcription factors such as the ETS family members (e.g. Elk-1) to induce the expression of early response genes.[34–36] Early response genes induced upon ERK activation encompass mainly transcription factors, including the FOS family members (c-Fos, Fra1, Fra2, FosB),[37] JUN family members (c-Jun, JunB, JunD)[37] and ATF family members (ATF2, ATF3, ATF4, BATF, BATF3).[37] These transcription factors then dimerize to form the AP-1 transcription factor complex[21,37] and induce late ERK response genes.[23]

The activity of the MAPK pathway is tightly regulated and includes several negative feedback loops directly or indirectly mediated by ERK.[38] Active ERK can inactivate RAF[39] and MEK[40,41] via inhibitory phosphorylation. Additionally, genes induced by ERK activation include dual-specific phosphatases (DUSPs), such as DUSP6, which dephosphorylate ERK[42] or sprouty proteins (SPRY)[38] which inhibit MAPK upstream activators.[43]

The MAPK/ERK pathway plays a role in many different processes including cell proliferation, survival and differentiation. Cell cycle progression induced by ERK activation is regulated by the transcription factors c-Fos and c-Jun amongst others.[44] These factors induce the expression of cyclin D,[44] which associates with the cyclin-dependent kinase (CDK) 4/6 to promote G1- to S-phase transition by inactivation of pRb.[45] Furthermore, ERK activation can

prevent apoptosis by inhibition of the pro-apoptotic protein Bad through phosphorylation by RSK.[23,46] Lastly, ERK activation can also play a role in the differentiation of cells, depending on the cell type and context. For instance, studies showed that ERK activation is involved in the development and differentiation of neurons.[47]

1.1.3.2 MAPK pathway deregulation

Alterations leading to increased MAPK activity are found in several different cancer entities and, overall, the MAPK pathway is the most commonly altered pathway in cancer.[48] Alterations can be found upstream of the MAPK cascade and include mutations in RTKs (e.g. EGFR or FGFR) or in different components of the RAS/RAF/MEK/ERK cascade (e.g. RAS or BRAF).[49-51] The type of alteration can vary across cancer types, with the most common alteration across cancer types being oncogenic RAS mutations.[52] Inactivating mutations within *NF1*, considered a tumor suppressor gene, which is responsible for inactivating RAS via GTP hydrolysis, have a similar effect.[53] *NF1* germline mutations cause neurofibromatosis type I, a genetic tumor syndrome.[53] Acquisition of additional somatic mutations in the second, healthy, *NF1* allele (= loss of heterozygosity) leads to tumor formation in these patients.[53] Furthermore, *BRAF* point mutations, most commonly V600E, leading to constitutive activation of BRAF without the need for dimerization, are a main driver of melanoma and are also found in colorectal cancer (CRC).[52]

Conversely, MAPK/ERK activation, especially if activation is too high, can also have deleterious effects by inducing oncogene-induced senescence (OIS)[54] or cell death.[55] This is sometimes referred to as the so-called “goldi-locks” principle[56], where too little MAPK/ERK activity does not promote cell proliferation/survival, the right amount of MAPK/ERK activation induces proliferation/survival and can be involved in tumor formation but too high MAPK activation has negative effects on cell proliferation/survival and tumor formation. How exactly this fine-tuning and in particular the consequences of different MAPK activity levels are regulated is not fully understood yet.[56]

Induction of oncogene induced senescence (OIS)[54] is a characteristic feature observed in pLGGs.[57] OIS is generally considered a protective mechanism of the cell to avoid aberrant growth.[58] However, factors secreted by senescent cells (senescence associated secretory phenotype (SASP) factors) can have growth suppressing and promoting effects.[58,59] The presence of OIS is likely a reason for the slow growth and overall good outcome of these tumors, and high expression of OIS and SASP gene signatures correlates with increased PFS in PA patients.[60] On the other hand, the presence of senescent cells (only 5% of PA cells express proliferation marker Ki-67)[61] can potentially be a limiting factor in the response to chemotherapeutics as well as other targeted agents as senescent cells may be less responsive to treatments targeting cell proliferation.[60,62–64]

1.1.3.3 Targeting of the pathway

MAPK-driven tumors can be targeted using different small molecule inhibitors. These inhibitors can target components upstream of the MAP kinase cascade, such as RTKs or RAS, or components within the MAP kinase cascade. The focus here will be on inhibitors targeting different components of the MAP kinase cascade, so-called MAPK inhibitors (MAPKi).

MAPK inhibitors can broadly be divided into three categories: 1) RAF inhibitors, 2) MEK inhibitors and 3) ERK inhibitors.

One class of BRAF inhibitors, including for instance the type 1 ½ inhibitors dabrafenib or vemurafenib, specifically target *BRAF*^{V600E}.[65,66] In non-V600E-altered cells, these inhibitors cause paradoxical activation of the pathway as they facilitate dimerization (i.e. activation) of wild-type (WT) BRAF unless used at oversaturating concentrations, which are not clinically achievable.[52,65,66] Following this discovery, so-called paradox breakers (e.g. PLX7904), where developed, which inhibit BRAF independent of its alteration status and type.[65–67] Furthermore, there are also pan-RAF inhibitors available (e.g. tovorafenib) which inhibit all forms of RAF.[68] MEK inhibitors are divided into ATP competitive and ATP non-competitive inhibitors (e.g. trametinib or selumetinib).[69] The latter ones often function through allosteric inhibition and are most commonly used due to their high specificity.[69,70]

Lastly, ERK inhibitors, the newest class of MAPK inhibitors, function either as catalytic inhibitors (e.g. ulixertinib), by inhibiting ERK activity, or as dual-mechanism inhibitors, which additionally also prevent the activating phosphorylation of ERK through MEK.[71]

Resistance to MAPKi is observed, and most commonly caused by activation of parallel pathways such as the PI3K/AKT/mTOR pathway.[72] While the combination of MAPK and mTOR inhibitors (e.g. everolimus), to avoid or overcome resistance to treatment, has shown promising effects in preclinical studies,[73,74] this combination was not well tolerated in adult patients.[75] First trials in a pediatric population indicate a possibly better tolerability of this treatment combination in younger patients (clinical observation). In addition to parallel pathway activation, excessive activation of CRAF can bypass the inhibitory effect of BRAF inhibitors, thereby reducing the treatment effect.[76] This can be circumvented for instance by the use of pan-RAF inhibitors or the combination of BRAF and MEK inhibitors.

1.1.4 Pre-clinical models

To date, there are very few faithful patient-derived pLGG models available.[77,78] The induction of OIS is a limiting factor in the generation of *in vitro* and *in vivo* models.[57,78,79] An exception to this are the BT-40 cells, which were derived from a juvenile PA and harbor a *BRAF*^{V600E} mutation as well as a *CDKN2A/B* deletion.[80] Based on the genetic background of the cell line, this model is considered to show features of a PXA. These cells grow both *in vitro* and *in vivo* (subcutaneously and orthotopically) in immunocompromised mice,[80–85] as the *CDKN2A/B* deletion circumvents OIS.[86] In addition to BT-40, three more models with *BRAF*^{V600E} mutation and co-occurring *CDKN2A/B*del were generated from patient material: BXD-3635PXA,[87] derived from a grade 2 PXA and growing *in vitro* and *in vivo*, and SJ-HGGX49 and SJ-HGGX60,[88] derived from grade 3 or grade 4 high-grade gliomas respectively and growing *in vivo*. In addition to being derived from high-grade gliomas in case of SJ-HGGX49 and SJ-HGGX60, none of these models is fully characterized yet though, including e.g. methylation profiling or response to MAPK inhibition.[87,88]

In recent years, several PA-derived cell models (*KIAA:BRAF* fusion: DKFZ-BT66, DKFZ-BT308, DKFZ-BT317; *BRAF*^{V600E}: DKFZ-BT314) could be generated in our group by inhibition of OIS using the SV40 large T antigen (SV40-TAg),[63,89,90] which inhibits p53 and pRb,[91] thereby inhibiting G1/G0 cell cycle arrest (a characteristic of senescence). These models make use of a doxycycline-inducible system, meaning cells can be expanded (= proliferating state), but also studied in their senescent state upon doxycycline withdrawal.[63,89,90] Xenotransplantation of these SV40-TAg based models has not be successful so far, most likely because replicative senescence is maintained (unpublished data). In another attempt to circumvent OIS, conditional reprogramming using a ROCK inhibitor was used to generate the *NF1*-loss-driven PA-derived cell line JHH-NF1-PA.[92] Further efforts in generating patient-derived pLGG models included the use of astrocyte growth media[93] or synthetic extracellular matrices.[94] In both cases, tumor cell cultures could be established, however growth was limited to 30-50 days of culture.[93,94]

In addition to patient-derived pLGG models, there are also advances in the generation of genetic pLGG models. These were generated by introducing pLGG driver mutations into neural stem cells (NSCs)[95,96] or induced pluripotent stem cells (iPSCs)[97] and can be used both *in vitro* and *in vivo*. While at the moment, these models only cover the most common alterations (*BRAF* fusion and *NF1* mutations), genetic engineering in principle offers the possibility to introduce any alteration of interest and therefore also study rarer molecular subgroups, which are not covered by currently available patient-derived models.

These models are of first importance in order to generate reliable pre-clinical data in order to support further clinical investigation of certain targeted therapies, such as MAPKi, for the treatment of pLGG patients.[78,81]

1.1.5 Current therapies and clinical trials

Standard-of-care (SOC) therapeutic interventions for pLGGs include surgery, if possible complete resection, and chemotherapy (vincristine (VCR) and carboplatin,[98,99] monotherapy with vinblastine,[100] or a combination of thioguanine, procarbazine, CCNU and vincristine

(TPCV))[99] and most recently targeted MAPK inhibition with dabrafenib/trametinib.[6,101] Classical radiation therapy, while showing good effects on tumor control (5-year PFS: 70-90%),[102,103] is no longer considered as a standard-of-care in general, due to severe long-term side effects, especially when administered to young patients, including secondary malignancy, cognitive and growth deficits as well as endocrine and vascular complications, in particular in NF1 patients.[103,104] However, advances in technologies, such as development of proton therapy, have reduced side-effects while still maintaining tumor control and radiation therapy is still considered for the treatment of pLGG patients on a case-to-case basis.[6,105] Factors taken into account when considering radiation therapy are patient age, genetic background (particularly NF1 mutation status), tumor location, clinical course of the disease and other therapeutic options.[6,105,106]

Advances in the molecular characterization of pLGGs has opened the possibility for molecular targeted treatment strategies targeting the hyperactivation of MAPK/ERK pathway. Several MAPK inhibitors are already approved for different diseases, such as melanoma or colorectal cancer,[50] and several clinical studies have tested the use of these agents in pLGG with promising results.[6] For example, studies assessing the efficacy of the BRAF type 1 ½ inhibitor dabrafenib showed an objective response rate (ORR) of 80% (retrospective analysis)[107] and 44% (phase I/II clinical trial).[108] Furthermore, dabrafenib and trametinib combination treatment showed a superior overall response (OR, 47%), compared to chemotherapy (11%) in $BRAF^{V600E}$-driven tumors.[109] Additionally, side effects, while observed in all patients, where considered less severe for dabrafenib and trametinib treatment compared to chemotherapy, with common side effects including fever, skin toxicities, nausea and vomiting.[109] The results of this phase II study recently lead to the FDA approval of dabrafenib and trametinib combination as first-line treatment of *BRAF*^{V600E} driven pLGGs.[101] Other MAPK inhibitors currently in clinical investigation include the type 1 ½ BRAF inhibitor vemurafenib, the pan-RAF inhibitor tovorafenib or the MEK inhibitor selumetinib.[110–112] (see Table 2 for a full list of trials).

Table 2 Clinical trials investigating MAPK inhibitors in pLGG
Information was taken from the clinical trial database at https://clinicaltrials.gov (accessed 23.01.2024)
If available, PubMed IDs (PMIDs) of publications related to a trial are listed.

Compounds	pLGG entities	Phase, status	Trial number	Related publications
Trametinib and everolimus	Relapsed pLGG	I, ongoing	NCT04485559	
Dabrafenib	BRAFV600E mutant pLGG and other pediatric tumors	I/II, completed	NCT01677741	PMID: 31811016, 31506385
Selumetinib	Relapsed pLGG	I/II, completed	NCT01089101	PMID: 33631016, 31151904
Vemurafenib	Relapsed BRAFV600E-mutant pLGG	I/II, completed	NCT01748149	PMID: 32523649
Dabrafenib, trametinib, hydroxychloroquine	Relapsed BRAF-mutant pLGG	I/II, ongoing	NCT04201457	
MEK162	pLGG and other MAPK pathway related tumors	I/II, ongoing	NCT02285439	
Tovorafenib	Relapsed MAPK pathway activated pLGG	I/II, ongoing	NCT03429803	
Dabrafenib and trametinib vs. carboplatin and vincristine	First-line treatment of BRAFV600E mutant pLGG or treatment of BRAFV600E mutant relapsed pediatric high-grade gliomas	II, completed	NCT02684058	PMID: 37733309, 37643378, 37610803
Tovorafenib	Relapsed BRAF-altered pLGG	II, ongoing	NCT04775485	PMID: 37978284
Trametinib	MAPK activated or NF1 driven pLGG and plexiform neurofibroma	II, ongoing	NCT03363217	PMID: 31881853
Trametinib vs. vinblastin	Newly diagnosed non-NF1 driven and BRAF WT pLGGs	II, ongoing	NCT05180825	

Selumetinib vs. carboplatin and VCR	Newly diagnosed NF1 associated pLGG	III, ongoing	NCT03871257	PMID: 33395032
Selumetinib vs. carboplatin and VCR	Newly diagnosed non-NF1 pLGG	III, ongoing	NCT04166409	PMID: 33395032
Selumetinib vs. selumetinib and vinblastine	Relapsed pLGG	III, ongoing	NCT04576117	
Tovorafenib vs. chemotherapy (investigators choice)	pLGGs with activating RAF alteration requiring first line treatment	III, ongoing	NCT05760586	

In addition to MAPK inhibitors, there are also studies investigating the use of mTOR inhibitors, as single agents or in combination.[113–115] Of possible interest is furthermore the use of FGFR inhibitors in case of FGFR-driven tumors as preclinical data suggests sensitivity to these inhibitors.[116] Additionally, BH3 mimetics, a class of senolytic agents, have shown efficacy against senescent PA cells *in vitro*.[60,63] Clinical investigations of FGFR inhibitors or BH3 mimetics in patients with pLGGs have not been conducted yet though.

While targeted inhibitors, in particular MAPK inhibitors, are promising new therapeutic options for the treatment of pLGGs, several open questions and challenges still remain regarding the use of these inhibitors. For one, long-term effects of MAPK inhibitors are not fully understood yet.[101] Furthermore, it is not fully understood why some patients respond to MAPKi therapy and others do not, despite sharing the same molecular background, tumor entity and location.[82] And lastly, while MAPK inhibitors show promising efficacy during treatment, patients may experience rapid tumor regrowth upon treatment stop, also referred to as rebound growth.[107,117]

1.2 Tumor rebound growth

1.2.1 Rebound growth in pLGGs

Tumor rebound growth in pLGGs refers to the rapid tumor regrowth after MAPKi treatment, that is observed in a subset of patients with response to MAPKi while on treatment (Patricia O'Hare et al., Neuro Oncol., under review).[107,117] Rebound growth is to be differentiated from

classical progression, observed e.g. after SOC chemotherapy treatment, and is defined as > 25% increase in tumor size within 3 months after treatment stop (Patricia O'Hare et al., Neuro Oncol., under review; .e.g. median time to progression after dabrafenib treatment: 2.3 months).[107] Progression or relapse is referred to in cases of > 25% tumor growth > 6 months after treatment stop or occurrence of a new lesion/metastasis (Patricia O'Hare et al., Neuro Oncol., under review). For cases of tumor regrowth between three to six months after treatment stop, no consensus has been reached so far whether this should be considered rebound growth or progression (Patricia O'Hare et al., Neuro Oncol., under review). It is important to note, that patients showing rebound growth will in most cases respond again to the original MAPKi treatment,[107,118] suggesting the absence of acquired resistance mechanisms driving the rebound growth. Possible mechanisms driving rebound growth are yet to be understood.

1.2.2 Rebound growth in other tumor entities

Rebound growth has also been described in other entities following withdrawal of targeted therapy. It is important to note that there are no clear definitions regarding timeframe or percentage of tumor growth for rebound growth in other tumor entities.[119–121] However, rebound growth is commonly referred to tumor regrowth shortly after treatment cessation, while relapse is considered to happen later after a longer disease-free/controlled period.[119–122]

A study investigating anti-angiogenic therapy using a VEGFR inhibitor showed that treatment stop can lead to rebound growth.[119] This rebound growth was driven by the transient induction of a SASP-mimicking phenotype, referred to as antiangiogenic therapy-induced secretome (ATIS), which persisted during early withdrawal periods and normalized after prolonged treatment withdrawal. Inhibition of known SASP regulators mTOR or IL-6 could suppress rebound growth.[119]

Furthermore, in MET amplified tumor entities, it was shown that rebound activation of MET-driven pro-proliferative pathways may occur after treatment with ATP-competitive MET inhibitors[120]. This rebound activation was caused by a prolonged hyperphosphorylation of MET

upon inhibitor withdrawal due to receptor accumulation and loss of negative feedback regulators during treatment.[120] Use of a MET therapeutic antibody inducing proteolytic cleavage of the receptor prevented rebound growth in this study, indicating actionability of this mechanism.[120]

Lastly, rebound growth, associated with faster proliferation compared to untreated cells, was also observed in different cancer cell lines (including CRC, renal and hepatocellular carcinoma cell lines) during withdrawal of PI3K or mTOR inhibitors.[121] In this study, rebound growth was shown to be caused by AKT overactivation mediated by IGF-1R and inhibition of either could prevent rebound growth.[121]

While the above studied tumor entities and treatments are distinct from pLGGs, one could envision similar mechanisms involved in rebound growth in pLGGs after MAPKi withdrawal, e.g. a role of SASP factors or MAPK pathway overactivation due to loss of negative feedback regulation.

1.3 Tumor microenvironment

1.3.1 TME composition in pLGG

A characteristic feature of most pLGGs is a high proportion of tumor microenvironment (TME) cells.[77] The TME contains a high proportion of microglia (30-50%),[123–125] followed by macrophages (~5-10%)[123] and T cells (~5-10%).[123,126] The proportion of the latter seems to vary across pLGG subtypes, with PXAs and GGs showing higher T cell content compared to PAs.[126] The TME, specifically immune cells, play important roles in pLGG biology (Figure 5).

1.3.1.1 Microglia

Microglia cells were shown to be involved in tumor formation in murine models, as BRAF fusion-driven NSCs did not form tumors in mice lacking the chemokine receptor CCR2, which is expressed on microglia cells and involved in their recruitment.[95] Furthermore, studies using *NF1*-loss-driven OPG models have shown that reduced numbers of optic nerve microglia cells[127] and inhibition of microglia activation reduces glioma growth.[128] In addition to positive

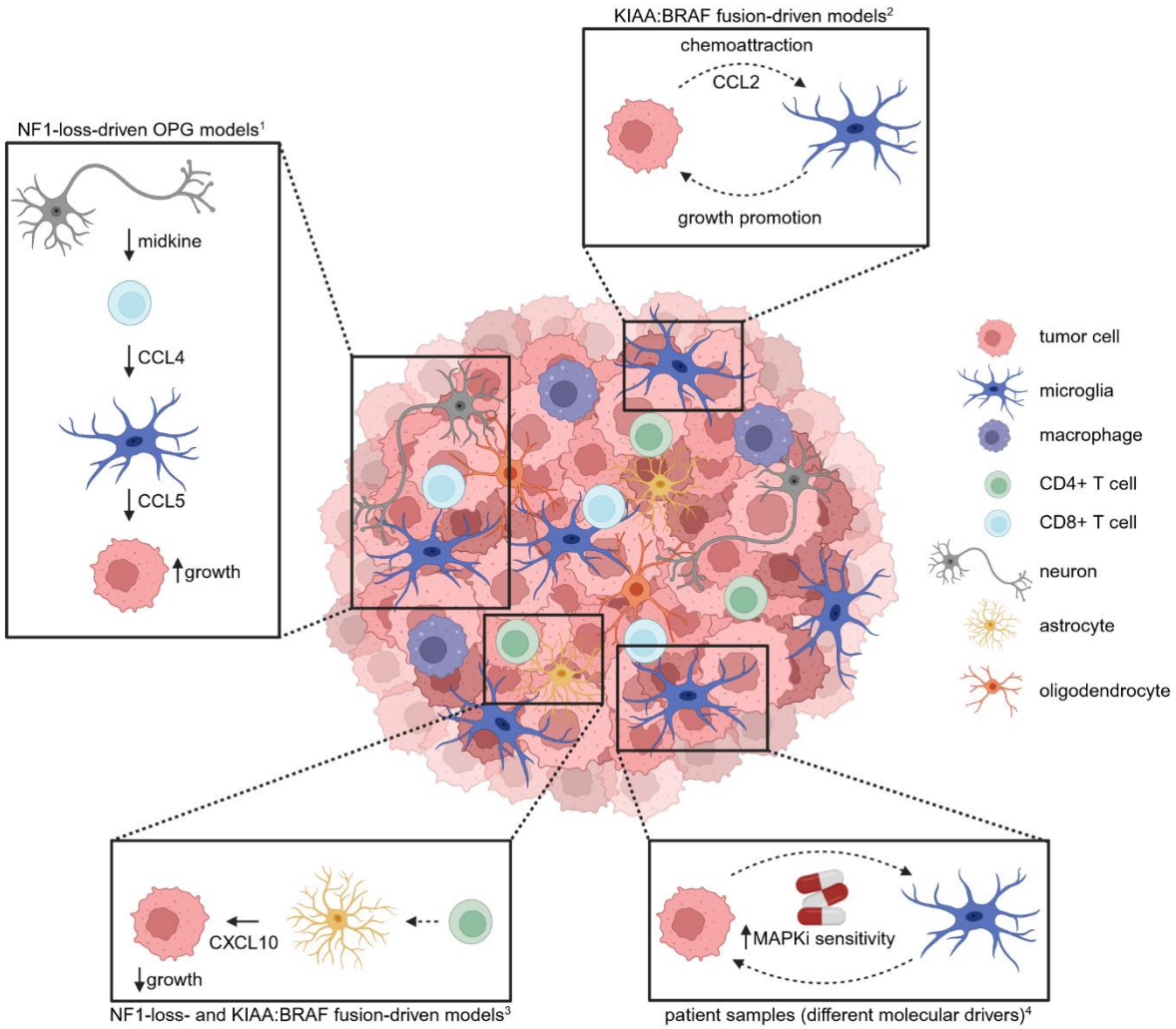

Figure 5 Interactions between tumor cells and the tumor microenvironment in pLGGs
[1] based on information from Guo, X. *et al.* 2020[129]; [2] based on information from Chen, J.Y. *et al.* 2019[95]; [3] based on information from Anastasaki, C. *et al.* 2022[97]; [4] based on information from Sigaud, R. *et al.* 2023[82]
created using BioRender.com

effects of microglia on tumor formation and growth, microglia have also been implied to play a potential role in the response to MAPK inhibitors, as it was shown that microglia infiltration correlates with a high predictive MAPK inhibitor sensitivity score (MSS).[82]

1.3.1.2 T cells

In cooperation with microglia cells, T cells have also been shown to have growth promoting effects in pLGGs. A study focusing on *NF1*-loss-driven pLGGs showed that neuronal midkine induced CCL4 expression in $CD8^+$ T cells, which in turn stimulated microglia cells to produce CCL5, a chemokine involved in pLGG stem cell survival and associated with reduced survival.[129] In contrast to $CD8^+$ T cells, $CD4^+$ T cells were shown to inhibit formation of hiPSC-

LGG xenografts through induction of CXCL10 expression in astrocytes.[97] Taken together, these data indicate complex interactions between tumor cells and TME cells, involved in different tumor promoting and suppressing processes.

In addition to effects of TME cells on tumor cells, it is also possible that tumor cells exert different effects on TME cells during tumor formation, progression, treatment and relapse.[130] Given the presence of OIS and the secretion of SASP factors, which include cytokines, an effect of tumor cells on TME cells, specifically immune cells, is likely.[130] Studies in other tumor entities have shown various effects of senescent cells (tumor or stromal) and SASP factors, including tumor suppression through recruitment of tumor-clearing immune cells,[131,132] or tumor promotion by establishing an immunosuppressive microenvironment.[133,134]

1.4 Cytokine/chemokine signaling

Cytokines are a diverse group of signaling proteins predominantly involved in inflammatory processes.[135] These proteins can be classified into different subgroups and include chemokines, interleukins, tumor necrosis factors, colony stimulating factors, interferons and transforming growth factors.[135] Of particular interest for this thesis are chemokines, in particular CCL2, CXCL10, CX3CL1 and CCL7, which will be the focus of this section

Chemokines are a group of chemotactic cytokines, which signal through G-protein coupled receptors or atypical chemokine receptors and are typically involved in stimulating the migration of various cell types, in particular immune cells.[136] They are grouped into subfamilies based on their primary amino acid sequence, specifically the arrangement of two cysteine residues at the N'-terminus: CC, CXC, CX3C and C, where X refers to the number of variable amino acids between the two cysteine residues.[137]

Chemokines play an important role in controlling immune cell trafficking between lymphoid organs, blood and peripheral tissues.[136] They are important mediators in the immune response during acute inflammation, by coordinating migration of immune cells to and from the

inflammatory site.[136] Furthermore, they are involved in immune cell differentiation and maintenance.[136]

1.4.1 Role of chemokines in cancer

Chemokines can have various tumor promoting and suppressing effects through influencing not only immune cells in the tumor microenvironment but also non-immune cells as well as tumor cells.

1.4.1.1 CCL2

While some studies, using soft-tissue sarcoma tumor samples and different cancer cell lines (including e.g. breast cancer or melanoma cells), indicate a tumor suppressive function of CCL2,[138,139] it is mostly described to promote tumor progression and metastasis through various mechanisms. For instance, CCL2 was shown to promote tumor progression and metastasis formation in chondrosarcoma or hepatocellular carcinoma both through direct effects on tumor cells, such as induction of matrix metalloproteinase expression,[140,141] as well as indirectly by affecting the microenvironment, e.g. macrophages.[142,143] Additionally, a study suggested a tumor-promoting role of CCL2[144] and CXCL10 in gliomas.[144,145]

1.4.1.2 CXCL10

Increased CXCL10 expression in breast cancer cells, induced by increased RAS activity, was further shown to promote tumor cell proliferation.[146] In contrast, CXCL10 was also shown to have antiangiogenic effects in melanoma, thereby suppressing tumor growth.[147] In addition, CXCL10 was shown to improve the anti-tumor effect of dendritic cell-based tumor vaccines in glioma[148,149] and CXCL10 plays a role in response to T cell therapy in melanoma.[150,151]

1.4.1.3 CCL7

Similarly to CXCL10, CCL7 has been implicated in promoting anti-tumor immunity by recruiting various immune cells to the TME, including dendritic cells, T cells and NK cells in non-small cell lung cancer or cervical carcinoma.[152,153] In contrast to its anti-tumor effects, CCL7 has also

been shown to promote metastasis formation for instance through recruitment of monocytic cells in renal cancer[154] or through activation of ERK/JNK signaling in CRC cells.[155]

1.4.1.4 CX3CL1

Cancer promotion through recruitment of monocytic cells, specifically M2-like macrophages, has also been shown for CX3CL1 in different entities, including testicular, breast or skin cancer.[156–158] Furthermore, CX3CL1 was also shown to promote tumorigenesis for example through promoting tumor cell proliferation in breast cancer[159] or epithelial to mesenchymal transition in prostate cancer.[160] On the other hand, CX3CL1 can also have tumor suppressing effects, mainly mediated by the attraction of tumor-suppressive immune cells such as M1-like macrophages in lung cancer[161] or T cells in renal cell carcinoma.[162]

CCL2 and CXCL10 have also been shown to play a role in pLGG biology, as described in "1.3 Tumor microenvironment" above.

2 Aim

Rebound growth after MAPKi withdrawal constitutes a significant clinical challenge that is not well understood in pLGGs. It is neither clear why only part of the patients responding to MAPKi therapy experience tumor rebound growth, nor is it known which mechanisms drive the rebound growth and how it could be inhibited. Therefore, the aim of my PhD project was to characterize possible mechanisms involved in the tumor rebound growth to provide a framework for future interventional studies.

As patient samples, collected during rebound growth, are not available as of now, the first aim of this project was the establishment of an *in vitro* rebound model using patient-derived cell lines.

Using the established *in vitro* rebound model, the second aim of the project was to investigate molecular mechanisms differentially regulated during MAPKi treatment and/or withdrawal using RNA sequencing, LC-MS/MS proteomics and phospho-proteomics analysis. Lastly, putative rebound driving mechanisms identified by multi-omics analysis, should be validated *in vitro* and *in vivo* to confirm differential regulation and possible rebound driving effect.

3 Materials and Methods

3.1 Materials

3.1.1 Cell lines and cell culture reagents

Table 3 Cell lines used

Cell line	Type	Mutations	Genetic modifications	Supplier
BT-40	Human juvenile PA-derived cell line	$BRAF^{V600E}$, CDKN2A/Bdel		A kind gift from Dr. P. Houghton, University of Texas Health Science Center at San Antonio, TX, USA
DKFZ-BT66	Human PA-derived cell line	KIAA1549:BRAF	Doxycycline inducible SV40-TAg (pFRIPZ)[89]	Generated in the CCU Pediatric Oncology, Heidelberg, Germany
DKFZ-BT308	Human PA-derived cell line	KIAA1549:BRAF	Doxycycline inducible SV40-TAg (pCW57.1 GFP-TAg)[63]	Generated in the CCU Pediatric Oncology, Heidelberg, Germany
DKFZ-BT314	Human PA-derived cell line	*BRAF*^{V600E}	Doxycycline inducible SV40-TAg (pCW57.1 GFP-TAg)[63]	Generated in the CCU Pediatric Oncology, Heidelberg, Germany
HMC3	Human microglia cell line		SV40-TAg immortalized	ATCC (cat. no. CRL-3304)

Table 4 Cell culture reagents

Article	Cat. no.	Supplier
AGM™ Astrocyte Growth Medium BulletKit™ (ABM media and supplements)	CC-3186	Lonza, Basel, Switzerland
PBS	D8537	Sigma-Aldrich, St. Louis, MO, USA
DMSO, cell culture grade	M6323.0100	Genaxxon bioscience, Ulm, Germany
Doxycycline	sc-337691	Santa Cruz, Dallas, TX, USA
FCS	F7524	Sigma-Aldrich, St. Louis, MO, USA

MEM	31095029	ThermoFisher Scientific, Waltham, MA, USA
10x NEAA	11140035	ThermoFisher Scientific, Waltham, MA, USA
RPMI 1640	21875034	ThermoFisher Scientific, Waltham, MA, USA
Sodium pyruvate (100 mM)	11360039	ThermoFisher Scientific, Waltham, MA, USA
0.05 % Trypsin-EDTA	25300054	ThermoFisher Scientific, Waltham, MA, USA
Vi-Cell XR Cell Viability Analyzer™ solutions	B94987	Beckmann Coulter, Krefeld, Germany

3.1.2 Treatment reagents and drugs

Table 5 Drugs used for *in vitro* treatment unless otherwise indicated
This table was adapted from Kocher *et al.*, under review

Inhibitor	Stock concentration [mM]	Solvent	Storage [°C]	Cat. no.	Supplier
Alpelisip	10	DMSO	-80	HY-15244	MedChemExpress
Carboplatin	27	Saline solution	4		Pharmacy of the university hospital of Heidelberg
Dabrafenib	10	DMSO	-80	S2807	Selleckchem
Dabrafenib for *in vivo* treatment	200 mg/ml	5% DMSO, 0.5% hydroxypropyl methylcellulose, 0.2% Tween-80 in water	4	HY-14660	MedChemExpress
Ipatasertib	10	DMSO	-80	HY-15186	MedChemExpress
Trametinib	10	DMSO	-80	S2673	Selleckchem
Vincristine	10	DMSO	-80	S9555	Selleckchem

Table 6 Recombinant cytokines

Cytokine	Stock concentration [µg/ml]	Solvent	Storage [°C]	Cat. no.	Supplier
CCL2	100	Sterile H_2O	-20	300-04	PeproTech, Cranbury, NJ, USA
CCL7	100	Sterile H_2O	-20	300-17	PeproTech, Cranbury, NJ, USA
CX3CL1	100	Sterile H_2O	-20	300-31	PeproTech, Cranbury, NJ, USA
CXCL10	100	Sterile H_2O	-20	300-12	PeproTech, Cranbury, NJ, USA

3.1.3 Primers

Table 7 Primers used for RT-qPCR
This table was adapted from Kocher *et al.*, under review

Gene	Forward primer 5'-3'	Reverse primer 5'-3'	Supplier
ACTB	CTGGAACGGTGAAGGTGACA	AAGGGACTTCCTGTAACAATGCA	Invitrogen, Waltham, MA, USA
CCL2 **(PMID: 30504064)**	GCTCAGCCAGATGCAATCAAT	ACTTGCTGCTGGTGATTCTTCTA	Invitrogen, Waltham, MA, USA
CCL7 (PMID: 33257678)	GTCCCCGGGAAGCTGTAATC	GCTTTGGAGTTTGGGTTTTCTT	Invitrogen, Waltham, MA, USA
CX3CL1 (PMID: 26015616)	GGATGCAGCCTCACAGTCCTTAC	GGCCTCAGGGTCCAAAGACA	Invitrogen, Waltham, MA, USA
CXCL10 **(PMID: 18495678)**	GAACTGTACGCTGTACCTGCA	TTGATGGCCTTCGATTCTGGA	Invitrogen, Waltham, MA, USA
FOS	/	/	Qiagen, Hilden, Germany (Hs_FOS_1_SG, cat. no. 249900)
TBP	AGAACAACAGCCTGCCAC	GTTGCTCTTCCAAAATAGACAGAC	Invitrogen, Waltham, MA, USA

3.1.4 Antibodies

Table 8 Antibodies and positive controls used for western blot analysis
[1] 5% BSA was commonly used, however blocking milk can also be used
[2] 5% BSA was commonly used as diluent, however these antibodies can also be diluted in 5% milk
temp. = temperature

Antibody	Blocking solution	Dilution, diluent	Incubation time (temp.)	Source/ clonality	Cat. no.	Supplier
AKT1/2	5% BSA[1]	1:1000, 5% BSA	O/N (4°C)	Rabbit polyclonal	9272	Cell Signaling Technology, Danvers, MA, USA
pAKT1/2 (S473)	5% BSA[1]	1:1000, 5% BSA	O/N (4°C)	Rabbit polyclonal	9271	Cell Signaling Technology, Danvers, MA, USA
β-Actin	5% BSA[1]	1:10000, 5% milk	O/N (4°C) or 2 h (RT)	Mouse monoclonal (clone AC-15)	A5441	Sigma-Aldrich, Munich, Germany
DUSP6	5% BSA	1:500, 5% BSA	O/N (4°C)	Rabbit polyclonal	39441	Cell Signaling Technology, Danvers, MA, USA
ERK1/2	5% BSA[1]	1:1000, 5% BSA[2]	O/N (4°C)	Rabbit monoclonal (clone 137F5)	4695	Cell Signaling Technology, Danvers, MA, USA
pERK1/2 (T202/T204)	5% BSA[1]	1:1000, 5% BSA[2]	O/N (4°C)	Rabbit monoclonal (clone 197G2)	4377	Cell Signaling Technology, Danvers, MA, USA
FRA1	5% BSA	1:1000, 5% BSA	O/N (4°C)	Rabbit monoclonal (clone D80B4)	5281	Cell Signaling Technology, Danvers, MA, USA
pFRA1 (S265)	5% BSA	1:1000, 5% BSA	O/N (4°C)	Rabbit monoclonal (clone D22B1)	5841	Cell Signaling Technology, Danvers, MA, USA

GSK3a/b	5% BSA[1]	1:1000, 5% BSA	O/N (4°C)	Rabbit monoclonal (D75D3)	5676	Cell Signaling Technology, Danvers, MA, USA
pGSK3a/b (S21/S9)	5% BSA[1]	1:1000, 5% BSA	O/N (4°C)	Rabbit polyclonal	9331	Cell Signaling Technology, Danvers, MA, USA
HSP90	5% BSA[1]	1:5000, 5% BSA[2]	O/N (4°C) or 2 h (RT)	Rabbit polyclonal	4874	Cell Signaling Technology, Danvers, MA, USA
MEK1/2	5% BSA[1]	1:1000, 5% BSA[2]	O/N (4°C)	Rabbit polyclonal	9122	Cell Signaling Technology, Danvers, MA, USA
pMEK1/2 (S217/S221)	5% BSA[1]	1:1000, 5% BSA[2]	O/N (4°C)	Rabbit monoclonal (clone 41G9)	9154	Cell Signaling Technology, Danvers, MA, USA
NF-kB p65	5% BSA	1:1000, 5% BSA	O/N (4°C)	Rabbit monoclonal (clone C22B4)	4764	Cell Signaling Technology, Danvers, MA, USA
pNF-kB p65	5% BSA	1:1000, 5% BSA	O/N (4°C)	Rabbit monoclonal (clone 93H1)	3033	Cell Signaling Technology, Danvers, MA, USA
PARP	Blocking milk	1:500, 5% BSA[2]	O/N (4°C)	Rabbit monoclonal (clone 46D11)	9532	Cell Signaling Technology, Danvers, MA, USA
S6K1	5% BSA[1]	1:1000, 5% BSA	O/N (4°C)	Rabbit polyclonal	9202S	Cell Signaling Technology, Danvers, MA, USA

pS6K1	5% BSA[1]	1:1000, 5% BSA	O/N (4°C)	Rabbit polyclonal	07-018	Sigma-Aldrich, Munich, Germany
SMAD2/3	5% milk	1:1000, 5% milk	O/N (4°C)	Rabbit monoclonal (clone D7G7)	8685	Cell Signaling Technology, Danvers, MA, USA
pSMAD2 (S465/467)/ pSMAD3 (S423/425)	5% milk	1:1000, 5% milk	O/N (4°C)	Rabbit monoclonal (clone D27F4)	8828	Cell Signaling Technology, Danvers, MA, USA
SMAD2/3 controls					12052	Cell Signaling Technology, Danvers, MA, USA
anti-mouse IgG HRP		1:10000, 5% milk	1-2 h (RT)	Goat polyclonal	115-035-003	Dianova, Hamburg, Germany
anti-rabbit IgG HRP		1:10000, 5% milk	1-2 h (RT)	Donkey polyclonal	V795A	Promega, Madison, WI, USA

Table 9 Neutralizing antibodies and IgG used for treatments

Antibody	Stock concentration [mg/ml]	Solvent	Storage [°C]	Cat. no.	Supplier
CCL2	0.5	Sterile PBS	-20	MAB279	R&D Systems, Minneapolis, MN, USA
CCL7	0.5	Sterile PBS	-20	MAB282	R&D Systems, Minneapolis, MN, USA
CX3CL1	0.5	Sterile PBS	-20	MAB3652	R&D Systems, Minneapolis, MN, USA
CXCL10	0.5	Sterile PBS	-20	MAB266	R&D Systems, Minneapolis, MN, USA
Mouse IgG	0.5	Sterile PBS	-20	MAB002	R&D Systems, Minneapolis, MN, USA

3.1.5 Biochemical reagents

Table 10 Biochemical reagents

Article	Cat. no.	Supplier
1,1,1,3,3,3-Hexafluoro-2-propanol (LC/MS grade)	83378	Biosolve B.V. Valkenswaard, Netherlands
16% formaldehyde solution (methanol free)	28908	ThermoFisher Scientific, Waltham, MA, USA
25% Ammonium hydroxide solution	40291H	Honeywell International, Charlotte, North Carolina, US
2-Chloroacetamide	C0267	Sigma-Aldrich, St. Louis, MO, USA
5M potassium hydroxide solution	24-4710	Sigma-Aldrich, St. Louis, MO, USA
Acetic acid	6755.1	Carl Roth, Karlsruhe, Germany
Acetonitrile (LC/MS grade)	1.00029	Sigma-Aldrich, St. Louis, MO, USA
Acrylamide/Bis solution (40 % w/v)	10681.01	SERVA, Heidelberg, Germany
Aprotinin	4139/10	R&D Systems, Minneapolis, MN, USA
APS	A3678	Sigma-Aldrich, St. Louis, MO, USA
Bromophenol Blue	A23331.0005	AppliChem, Darmstadt, Germany
BSA	A4612	Sigma-Aldrich, St. Louis, MO, USA
cOmpleteTM mini proteinase inhibitors	11836153001	Sigma-Aldrich, St. Louis, MO, USA
DAPI	D9542	Sigma-Aldrich, St. Louis, MO, USA
D-Luciferin	122799	PerkinElmer, Waltham, Massachusetts, US
DTT	A1101	AppliChem, Darmstadt, Germany
ECL Primer Amersham	RPN2232	GE Healthcare Dharmacon, Lafayette, CO, USA
Ethanol, absolute	20821.321	VWR chemicals, Radnor, PA, USA
Formic acid	069178	Biosolve B.V., Valkenswaard, Netherlands
Glycerol	15523	Honeywell Riedel-de-Haën, Seelze, Germany
Glycine	33226	Sigma-Aldrich, St. Louis, MO, USA

HCl	13-1683	Sigma-Aldrich, St. Louis, MO, USA
Iodoacetamide	I6125	Sigma-Aldrich
Isopropanol	20842.33	VWR chemicals, Radnor, PA, USA
Leupeptin hemisulfate	1167/25	R&D Systems, Minneapolis, MN, USA
LC/MS grade H_2O	232178	Biosolve B.V., Valkenswaard, Netherlands
Methanol	M/4000/PC17	ThermoFisher Scientific, Waltham, MA, USA
Methanol (LC/MS grade)	047192-K2	ThermoFisher Scientific, Waltham, MA, USA
NaCl	BP358-1	ThermoFisher Scientific, Waltham, MA, USA
NaOH	30620	Sigma-Aldrich, St. Louis, MO, USA
Normal goat serum	5-000-121	Dianova, Hamburg, Germany
Pepstatin A	1190/10	R&D Systems, Minneapolis, MN, USA
PhosSTOP phosphatase inhibitors	49068450001	Sigma-Aldrich, St. Louis, MO, USA
Precision Plus ProteinTM KaleidoscopeTM prestained protein standard	1610375	Bio-Rad, Hercules, CA, USA
ProLongTN Gold Antifade Mountant	P10144	ThermoFisher Scientific, Waltham, MA, USA
Propidium iodide	A2261.0025	WR chemicals, Radnor, PA, USA
qPCR Mastermix for SYBR® Green I	4309155	ThermoFisher Scientific, Waltham, MA, USA
Ribonuclease A	R6513-10MG	Sigma-Aldrich, St. Louis, MO, USA
RNaseZAP™	R2020-250ML	Sigma-Aldrich, St. Louis, MO, USA
SDC	D6750	Sigma-Aldrich, St. Louis, MO, USA
SDS pellets	2326.1	Carl Roth, Karlsruhe, Germany
Skimmed milk powder	T145.2	Carl Roth, Karlsruhe, Germany
TEMED	2367.3	Th. Geyer, Renningen, Germany
Trifluoroacetic acid (LC/MS grade)	202378	Biosolve B.V. Valkenswaard, Netherlands

Tris (Trizma Base)	T1503	Sigma-Aldrich, St. Louis, MO, USA
Tris-(2-carboxyethyl)-phosphin hydrogen chloride (TCEP/HCL)	PG82080	ThermoFisher Scientific, Waltham, MA, USA
Tri-Sodium citrate dihydrate	27833.294	VWR chemicals, Radnor, PA, USA
Triton X-100	A4975.0500	AppliChem, Darmstadt, Germany
Triton-X 100	A4975.0500	AppliChem, Darmstadt, Germany
Trypsin/Lys-C	V5072	Promega, Madison, WI, USA
Tween 20	500-018-3	MP Biomedicals, Santa Ana, CA, USA
β-mercaptoethanol	39563	SERVA, Heidelberg, Germany

3.1.6 Buffers and solutions

Table 11 Buffers and solutions

Solution (storage)	Final concentration	Recipe
APS (-20°C)	10% APS in de-ionized H2O	5g APS 50ml de-ionized water
90% acetone (RT or -20°C)	90% acetone	45 ml 100% acetone 5 ml LC/MS grade H_2O
Aprotinin solution	10mg/ml aprotinin	10 mg aprotinin 1 ml de-ionized H_2O
Array lysis buffer (per 10 cm dish)	10 µg/ml aprotinin 10 µg/ml leupeptin 10 µg/ml pepstatin	1 µl aprotinin solution 1 µl leupeptin solution 10 µl pepstatin solution 488 µl Lysis Buffer 6 (Proteome Profiler Human Phospho-Kinase Array Kit)
Blocking milk for WB (short-term: 4°C; long-term: -20°C)	20% skimmed milk 3% BSA 1% normal goat serum 0.2% Tween-20 20% FCS	200 g skimmed milk powder 30 g BSA 10 ml normal goat serum 2 ml Tween-20 200 ml FCS (not heat-inactivated) Fill-up to 1000 ml with PBS
5% BSA for WB (short-term: 4°C; long-term: -20°C)	5% BSA in TBS-T	5 g BSA 100 ml TBS-T
DAPI staining solution (prepare fresh, protect from light)	0.5 µg/ml DAPI	50 µl DAPI stock Fill-up to 10 ml with PBS

DAPI stock (-20°C, protect from light)	100 µg/ml DAPI	1 mg DAPI 10 ml de-ionized H_2O
10 mg/ml Doxycycline (-20°C, protect from light)	10 mg/ml doxycycline	100 mg doxycycline 10 ml sterile H_2O
1 mg/ml doxycycline (short-term: 4°C; long-term: -20°C; protect from light)	1 mg/ml doxycycline	1 ml 10 mg/ml doxycycline 9 ml sterile H_2O
1 M DTT (-20°C)	1 M DTT	1.54 g DTT 10 ml de-ionized, sterile H2O
500 mM DTT (prepare fresh)	500 mM DTT	38.565 mg DTT in 500 µl LC/MS grade H_2O
70% ethanol (RT)	70% Ethanol	70 ml 99.9% absolute ethanol 30 ml de-ionized H_2O
FACS staining solution, per sample (use immediately, protect from light)	50 µg/ml PI 50 µg/ml Ribonuclease A	8 µl PI stock 2 µl Ribonuclease A 400 µl FACS washing buffer
FACS washing buffer (4°C)	38 mM sodium citrate buffer	3.8 ml sodium citrate buffer 96.2 ml de-ionized H_2O
FCS (-20°C)		Heat-inactivated, 56°C for 30min
Firefly D-Luciferin solution (-20°C, protect from light)	15 mg/ml D-Luciferin	1 g D-Luciferin 66.67 ml dPBS
500 mM IAA (prepare fresh)	500 mM iodoacetamide	184.96 mg iodoacetamide in 2 ml LC/MS grade H_2O
5x Laemmli buffer (once DTT is added store at -20°C and use within a week)	10% SDS 50% glycerol 0.3125 M Tris-HCL 5 mM DTT	1 g SDS pellets 5 ml 100% glycerol 3.125 ml 1 M Tris buffer 50 µl 1 M DTT Fill-up to 10 ml with de-ionized H_2O
Leupeptin solution	10 mg/ml leupeptin hemisulfate	25 mg leupeptin hemisulfate 2.5 ml de-ionized H_2O
5% milk for WB (short-term: 4°C; long-term: -20°C)	5% milk in TBS-T	5 g milk powder 100 ml TBS-T
MS resuspension buffer (RT)	2.5% 1,1,1,3,3,3-Hexafluoro-2-propanol 0.1% Trifluoroacetic acid	2.5 ml 1,1,1,3,3,3-Hexafluoro-2-propanol (LS/MS grade) 0.1 g trifluoroacetic acid (LC/MS grade) in 100 ml LC/MS grade H_2O

Pepstatin solution	1 mg/ml pepstatin A	10 mg pepstatin A 10 ml Ethanol
4% PFA (up to 1 week at 4°C)	4% Formaldehyde	10 ml 16% formaldehyde solution (methanol free) 30 ml PBS
PI stock (4°C; protect from light)	2mg/ml PI	25 mg PI 10 ml de-ionized H_2O
Primer mix	10 µM fw. primer 10 µM rev. primer	10 µl 100 µM fw. primer 10 µl 100 µM rev. primer 80 µl nuclease-free H_2O
Proteomics elution buffer (RT)	80% acetonitrile 1.25% Ammonium hydroxide	80 ml acetonitrile 5 ml 25% Ammonium hydroxide solution 15 ml LC/MS grade H_2O
Proteomics reduction buffer (prepare fresh)	400 mM 2-Chloroacetamide 100 mM Tris-(2-carboxyethyl)-phosphin hydrogen chloride (TCEP/HCL) 400 mM Potassium hydroxide	37.4 mg 2-Chloroacetamide 28.8 mg TCEP/HCL 80 µl 5M Potassium hydroxide
Proteomics wash buffer 1 (RT)	1% trifluoroacetic acid	1 g trifluoroacetic acid (LC/MS grade) in 100 ml LC/MS grade H_2O
Proteomics wash buffer 2 (RT)	0.2% trifluoroacetic acid	200 µg trifluoroacetic acid (LC/MS grade) in 100 ml isopropanol (LC/MS grade)
qPCR mastermix (per sample)		10 µl qPCR Mastermix for SYBR® Green I 2 µl primer mix 3 µl nuclease-free H_2O
10X running buffer (RT)	25mM Tris 192 mM Glycine 0.1% SDS	30.3 g Tris 144.1 g 10 g SDS pellets Fill-up to 1000 ml with de-ionized H_2O
1X running buffer (RT)		100 ml 10x running buffer 900 ml de-ionized H_2O
SDB-RPS equilibration buffer 1 30% methanol (RT)	30% methanol	30 ml methanol (LC/MS grade) 70 ml LC/MS grade H_2O
SDB-RPS equilibration buffer 2 (RT)	0.2% trifluoroacetic acid	200 µg trifluoroacetic acid (LC/MS grade) in 100 ml LC/MS grade H_2O

SDC lysis buffer (short-term: -20°C)	4% SDC	0.4 g SDC 10 ml LC/MS grade H_2O
20% SDS	20% SDS	20 g SDS pellets Fill-up to 100 ml with de-ionized H_2O
SDS lysis buffer stock (-20°C)	2% SDS 10% glycerol Stacking gel buffer	10 ml SDS solution (20%) 10 ml glycerol (100%) 12.4 ml stacking gel buffer Fill-up to 100 ml with de-ionized H_2O
SDS lysis buffer (-20°C, use within 2 weeks)		10 ml SDS lysis buffer stock 1 tablet PhosSTOP phosphatase inhibitors 1 tablet cOmplete™ mini proteinase inhibitors 10 µl 1 M DTT
Separating gel buffer pH8.8 (RT)	1.5 mM Tris	36.34 g Tris Fill-up to 200 ml with de-ionized H_2O set pH to 8.8 by drop-wise addition of HCl
Sodium citrate buffer (4°C)	1 M tri-sodium cytrate dihydrate	25.8 g tri-sodium cytrate dihydrate 100 ml de-ionized H_2O
Stacking gel buffer pH 6.8 (RT)	0.5 mM Tris	12.12 g Tris Fill-up to 100 ml de-ionized H_2O set pH to 6.8 by drop-wise addition of HCl
10x TBS (RT)	200 mM Tris 1.37 M NaCl	120 g Trizma Base 400 g NaCl Fill-up to 5000 ml with de-ionized H_2O set pH to 7.6 by drop-wise addition of HCl
TBS for proteomics (RT)	1X TBS	10 ml 10x TBS 90 ml LS/MS grade H_2O
TBS-T (RT)	1x TBS 0.1% Tween-20	100 ml 10x TBS 1 ml Tween-20 Fill-up to 1000 ml with de-ionized H_2O
1% TFA (RT)	1% Trifluoroacetic acid	100 µl Trifluoroacetic acid 9.9 ml isopropanol (LC/MS grade)

1 M Tris buffer (RT)	1 M Tris-HCL	12.114g Tris Fill-up to 100 ml with de-ionized H_2O set pH to 6.8 by drop-wise addition of HCl
0.5% Triton X (RT)	0.5% Triton X-100	250 µl 100% Triton X-100 49.75 ml PBS
Trypsin/Lys-C mix (-0°C)	0.5 µg/µl Trypsin/Lys-C	100 µg lyophilized Trypsin/Lys-C 200 µl resuspension buffer (provided with enzyme mix)

3.1.7 Consumables

Table 12 Consumables

Article	Supplier
Cell scraper	Sarstedt, Nürnbrecht, Germany
Conical tubes, 15 ml and 50 ml	ThermoFisher Scientific, Waltham, MA, USA
Cotton swabs	Isana, Rossmann, Hannover, Germany
Cryovials	Carl Roth, Karlsruhe, Germany
D300e Digital dispenser dispenshead casettes T8+	Tecan, Männerdorf, Switzerland
Falcon® 5ml round bottom polystyrene tubes	ThermoFisher Scientific, Waltham, MA, USA
Falcon® Permeable Support for 24-well Plate with 8.0 µm Transparent PET Membrane	Corning, Kaiserslautern, Germany
Falcon® Permeable Support for 6-well Plate with 0.4 µm Translucent High Density PET Membrane	Corning, Kaiserslautern, Germany
Falcon® 24-well TC-treated Cell Polystyrene Permeable Support Companion Plate, with Lid, Sterile	Corning, Kaiserslautern, Germany
Falcon® 6-well TC-treated Polystyrene Permeable Support Companion Plate, with Lid, Sterile	Corning, Kaiserslautern, Germany
Glassware	SCHOTT AG, Mainz, Germany
Greiner Bio-One 96-well sterile cell culture plate with flat bottom, black with transparent bottom	Greiner Bio-One, Frickenhausen, Germany
Kimtech wipes	Kimberly-Clark Kimtech Science, Irving, TX, USA

Menzel-Gläser Coverslips, 21x60 mm #1	ThermoFisher Scientific, Waltham, MA, USA
Menzel-Gläser Polysine® Slides, 25x75x1 mm	ThermoFisher Scientific, Waltham, MA, USA
Parafilm® M	Benis, Braine-l'Alleud, Belgium
PCR tube strips and domed caps	ThermoFisher Scientific, Waltham, MA, USA
Pipette filter tips, 10 µL, 20 µL, 100 µL, 200 µL, 1000 µL	Nerbe plus, Winsen/Luhe, Germany
PVDF membrane	Bio-Rad, Hercules, CA, USA
Safe-Lock reaction tubes, 0.5 ml, 1.5 ml, 2.0 ml, 5 ml	Eppendorf, Hamburg, Germany
Scalpels	VWR International, Radnor, PA, USA
SDB-RPS extraction disk	Merck Millipore, Burlington, MA, USA
Serological pipettes, 5 ml, 10 ml, 25 ml, 50 ml	Sigma-Aldrich, St. Louis, MO, USA
Sterile filter, 0.2 µm	Merck Millipore, Burlington, MA, USA
Syringe 10 ml, 10 ml	Terumo, Tokyo, Japan
Tissue culture dishes, 6 cm, 10 cm	TPP Techno Plastic Products AG, Trasadingen, Switzerland
Tissue culture flasks, 25 cm^2, 75 cm^2, 175 cm^2	Greiner Bio-One, Frickenhausen, Germany
Tissue culture plates, 6 well, 24 well	Corning, Kaiserslautern, Germany
ViCell 4 ml tubes	Beckmann Coulter, Brea, CA, USA

3.1.8 Kits

Table 13 Kits

Article	Cat. no.	Supplier
Agilent RNA 6000 Nano Kit	5067-1511	Aligent, Santa Clara, CA, USA
Agilent RNA 6000 Nano Ladder	5067-1529	Aligent, Santa Clara, CA, USA
Amersham ECL Prime Western Blotting Detection Reagent	RPN2232	GE Healthcare Dharmacon, Lafayette, CO, USA
Bio-Plex Pro HuCSP standard	12007919	Bio-Rad, Hercules, CA, US
Bio-Plex Pro Human Chemokine standard	171DK0001	Bio-Rad, Hercules, CA, US
Bio-Plex Pro Reagent Kit 3	71304090M	Bio-Rad, Hercules, CA, US

CellTiterGlo 2.0	G9243	Promega, Madison, WI, USA
High-Select™ TiO2 Phosphopeptide Enrichment Kit	A32993	ThermoFisher Scientific, Waltham, MA, USA
PierceTM BCA Protein Assay Kit	23227	ThermoFisher Scientific, Waltham, MA, USA
Pierce™ Quantitative Colorimetric Peptide Assay Kit	23275	ThermoFisher Scientific, Waltham, MA, USA
Proteome Profiler Human Phospho-Kinase Array Kit	ARY003C	R&D Systems, Minneapolis, MN, USA
QIAamp® DNA Mini Kit		Qiagen, Hilden, Germany
qPCR Mastermix for SYBR® Green I	4309155	ThermoFisher Scientific, Waltham, MA, USA
RevertAid First Strand cDNA Synthesis Kit	K1622	ThermoFisher Scientific, Waltham, MA, USA
RNA ScreenTape	5067-5576	Aligent, Santa Clara, CA, USA
RNA ScreenTape Ladder	5067-5578	Aligent, Santa Clara, CA, USA
RNA ScreenTape Sample Buffer	5067-5577	Aligent, Santa Clara, CA, USA
RNase free DNase Set	79254	Qiagen, Hilden, Germany
RNeasy Mini Kit	74104	Qiagen, Hilden, Germany
Trans-Blot Turbo RTA Mini 0.45 µM LF PVDF Transfer Kit	1704274	Bio-Rad, Hercules, CA, US
Venor® GenM Classic Mycoplasma Detection Kit	11-1250	Minerva Biolabs, Berlin, Germany

Table 14 Bioplex custom multiplexes
All reagents were bought from Bio-Rad, Hercules, CA, US
Singleplexes were combined to custom multiplexes (multiplex 1 or 2) as indicated
This table was adapted from Kocher *et al.*, under review

Target	Cat. no.	Standard used	Multiplex
CCL2	171B5021M	Bio-Plex Pro HuCSP standard	1
CCL11	171B5015M	Bio-Plex Pro HuCSP standard	1
CXCL1	171B6007M	Bio-Plex Pro HuCSP standard	1
CXCL10	171B5020M	Bio-Plex Pro HuCSP standard	1
IL-1A	171B6001M	Bio-Plex Pro HuCSP standard	1
IL-1B	171B5001M	Bio-Plex Pro HuCSP standard	1
IL-8	171B5008M	Bio-Plex Pro HuCSP standard	1

IL-9	171B5009M	Bio-Plex Pro HuCSP standard	1
LIF	171B6011M	Bio-Plex Pro HuCSP standard	1
CCL7	171BK38MR2	Bio-Plex Pro Human Chemokine standard	2
CCL17	171BK53MR2	Bio-Plex Pro Human Chemokine standard	2
CX3CL1	171BK18MR2	Bio-Plex Pro Human Chemokine standard	2
CXCL2	171BK23MR2	Bio-Plex Pro Human Chemokine standard	2
CXCL5	171BK14MR2	Bio-Plex Pro Human Chemokine standard	2
CXCL6	171BK19MR2	Bio-Plex Pro Human Chemokine standard	2
TNF-alpha	171BK55MR2	Bio-Plex Pro Human Chemokine standard	2

3.1.9 Instruments and devices

Table 15 Instruments and devices

Instrument	Supplier
2100 Bioanalyzer	Aligent, Santa Clara, CA, USA
ABI 7500 real time PCR cycler	Applied Biosystems, Foster City, CA, USA
Analytical balance "BP 121S"	Sartorius, Göttingen, Germany
Azure c400 imaging system	Azure Biosystems, Dublin, CA, USA
BarnsteadTM GenPureTM xCAD Plus Ultrapure water purification system	ThermoFisher Scientific, Waltham, MA, USA
BD FACS Canto II analyzer	Becton, Dickinson and Company, Heidelberg, Germany
Benchtop centrifuge Micro Star 17R	VWR International, Radnor, PA, USA
Bio-Plex 200 System	Bio-Rad, Hercules, CA, US
CellCamper® Mini	neoLab Migge GmbH, Heidelberg, Germany
Centrifuge 5810 R	Eppendorf, Hamburg, Germany
Cryo freezing container Nalgene® Cryo 1°C "Mr. Frosty"	ThermoFisher Scientific, Waltham, MA, USA
D300e Digital dispenser	Tecan, Männerdorf, Switzerland
Einkanal-Mikroliterpipette Transferpette® S, 0.1-2.5 µl, 0.5-10 µl, 2-20 µl, 20-200 µl, 100-1000 µl	BRAND GMBH + CO KG, Wertheim, Germany
Electrophoresis chamber Mini-Protean® Tetra System	Bio-Rad, Hercules, CA, USA
Eppendorf Mastercycler gradient	Eppendorf, Hamburg, Germany
Epson perfection V700 photo scanner	EPSON, Nagano, Japan
Fluorescence microscope Eclipse Ts2	Nikon, Minato, Japan
FLUOstar Omega automated plate reader	BMG Labtech, Ortenberg, Germany
FLUOstar OPTIMA automated plate reader	BMG Labtech, Ortenberg, Germany

Hamilton syringe	Hamilton Company, Reno, NV, USA
Heat sealer "Folio"	Severin Elektro, Sundern, Germany
Heating block Thermomixer® Comfort	Eppendorf, Hamburg, Germany
Incubator Heraeus B6420	Heraeus, Leverkusen, Germany
IVIS Lumina III In Vivo imaging system	PerkinElmer, Waltham, MA, US
Light microscope CKX31	Olympus, Hamburg, Germany
LSM 710 confocal microscope	Zeiss, Oberkochen, Germany
Magnetic stirrer with heating MR-3001	Heidolph Instruments, Schwabach, Germany
Microwave Severin MW 7869	Severin Elektro, Sundern, Germany
Multi-axle rotating mixer TRM 56	IDL GmbH, Nidderau, Germany
Nano-Drop ND-1000 spectrophotometer	PEQLab, Erlangen, Germany
NovaSeq 6000 System	Illumina, San Diego, CA, USA
pH meter SevenCompact	Mettler-Toledo, Gießen, Germany
Pipetboy acu 2	INTEGRA Biosciences, Zizers, Switzerland
Power supply EV231	PEQLab, Erlangen, Germany
Power supply PowerPacTM Basic Power Supply	Bio-Rad, Hercules, CA, USA
Precision balance 440-47N	Kern & SOHN, Balingen, Germany
Qubit Fluorometer	ThermoFisher Scientific, Waltham, MA, USA
Refrigerator with freezer	Liebher, Biberach and der Riß, Germany
Rocking platform WT 16	Biometra, Göttinger, Germany
TapeStation System	Aligent, Santa Clara, CA, USA
Test tube shaker Reax Top	Heidolph Instruments, Schwabach, Germany
timsTOF Pro 2	Bruker Daltonics, Billerica, MA, US
Tip probe sonicator "Sonopuls HD2070"	Bandelin, Berlin, Germany
Tissue culture incubator "C200"	Labotect, Rosdorf, Germany
Tissue culture incubator "CB220"	Binder GmbH, Tuttlingen, Germany
Tissue culture sterile bench "MaxiSafe 2030i"	ThermoScientific, Waltham, MA, USA
Tissue culture sterile bench "Safe2020"	ThermoScientific, Waltham, MA, USA
TissueLyser II	Qiagen, Hilden, Germany
Trans-Blot Turbo Transfer System	Bio-Rad, Hercules, CA, US
Ultra-low temperature freezer	ThermoFisher Scientific, Waltham, MA, USA
Ultrasonic bath "Sonorex RK 52"	Bandelin, Berlin, Germany
Vacuum concentrator "Concentrator plus"	Eppendorf, Hamburg, Germany

Vi-CELL XR automated cell counter	Beckmann Coulter, Brea, CA, USA
Vortexer IKA VF2	IKA Janke & Kunkel, Staufen im Breisgau, Germany
VWR ® Shaking water bath (18L)	VWR chemicals, Radnor, PA, USA

3.1.10 Databases and online tools

Table 16 Databases used

Database	Website
Ensembl	https://www.ensembl.org/index.html
MSigDB v7.5.1	https://www.gsea-msigdb.org/gsea/msigdb/index.jsp
NCBI	https://www.ncbi.nlm.nih.gov/
PTMsigDB collection v2.0.0	https://www.gsea-msigdb.org/gsea/msigdb/ptmsig_genesets.jsp
UniProt	https://www.uniprot.org/

Table 17 Online tools used

Online tool	Website
KSEA App	https://casecpb.shinyapps.io/ksea/
GenePattern	https://cloud.genepattern.org/gp/pages/login.jsf
Ensembl biomart tool	https://www.ensembl.org/biomart/martview/f56b42a8d6d680d78eb80477314a5257

3.1.11 Software

Table 18 Software used

Software	Supplier
ABI 7500 software v2.3	Applied Biosystems, ThermoFisher Scientific, Waltham, MA, USA
Azure c400 acquisition software	Azure Biosystems, Dublin, CA, USA
BioRender	BioRender
CellProfiler v.4.1.3	Broad Institute, Cambridge, MA, USA
ClueGo v2.5.9 (Cytoscape plugin)	Laboratory of Integrative Cancer Immunology, Paris, France
Cytoscape v3.9.1	Cytoscape Consortium
D300e Digital dispenser control software	Tecan, Männerdorf, Switzerland
FlowJoTM v10.9.0	FlowJo, LLC, Ashland, OR, USA
GraphPad Prism v8.0.2	GraphPad Software Inc, San Diego, CA, USA
ImageJ v2.9.0	National Institutes of Health

Living Image Software Version 4.4	PerkinElmer, Waltham, MA, US
MaxQuant software v1.6.17.0	Max Planck Institute of Biochemistry, Martinsried, Germany
Mendeley	Mendeley Ltd
Microsoft Office 2019	Microsoft, Redmond, WA, USA
Omega Microplate reader software v5.11R4	BMG Labtech, Ortenberg, Germany
OPTIMA Microplate reader software v2.20R2	BMG Labtech, Ortenberg, Germany
R 4.2.2	The R Foundation, Vienna, Austria
RStudio v2023.12.0	RStudio, Boston, MA, USA
Vi-CELLTM XR 2.03 software	Beckmann Coulter, Brea, CA, USA

3.2 Methods

3.2.1 Cell culture

BT-40 cells[84] were a kind gift from Prof. Houghton. DKFZ-BT66,[64] DKFZ-BT308[63] and DKFZ-BT314[63] were generated in our group. The microglia cell line HMC3 was purchased from the ATCC.

Cell lines were authenticated through SNP or STR profiling using Multiplex Cell Authentication by Multiplexion GmbH (Heidelberg, Germany). The purity of cell lines was evaluated using the Multiplex cell Contamination Test by Multiplexion GmbH (Heidelberg, Germany). Furthermore, cells were checked monthly for human mycoplasma contaminations by PCR with the Venor® GeM Kit.

3.2.1.1 Maintenance and passaging

Cells were maintained in the respective culture media as indicated in Table 19 in a humidified atmosphere containing 5% CO_2 at 37°C. For DKFZ-BT66, DKFZ-BT308 and DKFZ-BT314, 1 µg/ml doxycycline was added to the culture media to maintain cells in a proliferative state (induced by SV40-TAg expression). For all cell lines, media was replenished every 2-3 days and cells were passages when they reached a certain confluence as indicated in Table 19. For passaging, cells were washed 1-2 times with PBS before detaching using 0.05% Trypsin-EDTA. After 5-10 minutes at 37°C, when cells were detached, trypsin was inactivated with

media (twice the amount of trypsin) and seeded in new cell culture vessels at varying ratios (see Table 19).

Table 19 Cell culture conditions

Cell line	Culture media	Freezing media (cell number)	Max. confluence (splitting ratio)	Max. no. of passages used
BT-40	RPMI + 10% FCS	RPMI + 20% FCS + 10% DMSO (3-5x10^6 cells; thaw in T75 flask)	80-90% (up to 1:20)	20
DKFZ-BT66	ABM + supplements Optional: 1 µg/ml doxycycline	ABM + supplements + 10% DMSO (3-5x10^6 cells; thaw in T75 flask)	90-100% (up to 1:10)	15
DKFZ-BT308	ABM + supplements Optional: 1 µg/ml doxycycline	ABM + supplements + 10% DMSO (3-5x10^6 cells; thaw in T75 flask)	90-100% (up to 1:10)	15
DKFZ-BT314	ABM + supplements Optional: 1 µg/ml doxycycline	ABM + supplements + 10% DMSO (3-5x10^6 cells; thaw in T75 flask)	90-100% (up to 1:10)	15
HMC3	MEM + 10% FCS + 1x NEAA + 1 mM Sodium Pyruvat	MEM + 10% FCS + 10% DMSO (1.5-3x10^6 cells; thaw in T75 flask)	70-80% (up to 1:10)	25

3.2.1.2 Freezing and thawing

For freezing, cells were counted using the ViCELL XR (settings see Table 20) and resuspended in freezing media (Table 19), aliquoted into cryovials, transferred to a - 80°-freezer in a MrFrosty or CellCamper for at least 24h. Afterwards cells were either stored at -80°C for short-term storage (< 1 year) or in liquid nitrogen for long-term storage.

For thawing, vials with frozen cells were placed in a 37°C water bath for 30 sec and then resuspended in warm (37°C) cell culture media until completely thawed. Following, cells were

spun down at 1200 rpm for 5 min, resuspended in fresh media and seeded in an appropriate cell culture vessel (Table 19). To remove dead cells and debris after thawing, media was changed the next day.

3.2.1.3 Seeding for experiments

For seeding, cells were detached as described above (3.2.1.1 Maintenance and passaging) and counted using the ViCELL XR using the settings in Table 20. Seeding densities for all experiments and conditions can be found in Table 21. If not otherwise indicated, BT-40, DKFZ-BT308 (proliferating) and DKFZ-BT314 (proliferating) were seeded for experiments two days prior to experiment start in complete media (containing all supplements) and upon experiment start switched to minimum media. For BT-40 cells, minimum media contained only 2% FCS. For, DKFZ-BT308 and DKFZ-BT314, minimum media contained only 2% FCS and no EGF and insulin supplements. DKFZ-BT66 (proliferating) were also seeded two days prior to experiment start in complete media and experiments were also performed in complete medium. In case DKFZ-BT66, DKFZ-BT308 and DKFZ-BT314 were studied in senescent mode, cells were seeded five days before experiment start in complete media without doxycycline. Upon start of an experiment, DKFZ-BT308 and DKFZ-BT314 were switched to minimum media without doxycycline, DKFZ-BT66 remained in complete media without doxycycline.

Table 20 ViCELL XR counting settings
This table was adapted from Kocher *et al.*, under review

Parameter	Setting
Cell brightness	85%
Cell sharpness	100
Viable cell spot brightness	65%
Viable cell spot area	5%
Minimum circularity	0
Decluster degree	Medium
Minimum diameter	5 microns
Maximum diameter	50 microns
Images	50
Aspirate cycles	1
Trypan blue mixing cycles	3

Table 21 Seeding densities
wd = withdrawal; This table was adapted from Kocher *et al.*, under review

Experiment	Format	Cell line	Condition	Cell number
Metabolic activity assay	96-well-plate	BT-40		$0.03x10^6$
Cell counting for growth curve analysis	6-well-plate	BT-40		$0.2x10^6$
		DKFZ-BT66 proliferating		$0.1x10^6$
		DKFZ-BT66 senescent		$0.2x10^6$
		DKFZ-BT308 and DKFZ-BT314 senescent and proliferating		$0.1x10^6$
Sample generation for qPCR and WB analysis	6-well-plate	BT-40	5 days DMSO + wd	$0.2x10^6$
			5 days treatment + wd	$1x10^6$
RNAseq sample generation	6 cm dish	BT-40	5 days DMSO + wd	$0.6x10^6$
			5 days dabrafenib + wd	$1.5x10^6$
Sample generation for LC-MS/MS proteomics and phosphoproteomics	10 cm dish (3 per sample)	BT40	5 days DMSO + wd	$2x10^6$
			5 days dabrafenib + wd	$5x10^6$
Multiplexed ELISA assay	6 cm dish	BT-40	5 days DMSO + wd	$0.4x10^6$
			5 days dabrafenib + wd	$1.5x10^6$
Kinase phosphorylation array	10 cm dish (3 per sample)	BT-40	5 days DMSO + wd	$0.4x10^6$
			5 days dabrafenib + wd	$1.5x10^6$
Conditioned media collection	6 cm dish	BT-40	5 days DMSO + wd	$0.4x10^6$
			5 days dabrafenib + wd	$1.5x10^6$
Transwell co-culture	6-well-plate	BT-40		$0.2x10^6$
	6-well transwells	HMC3		$0.08x10^6$
Transwell migration assay	24-well transwells	HMC3		$0.1x10^6$

3.2.2 Drug treatments and withdrawal

All inhibitors used for *in vitro* experiments are listed in Table 5.

3.2.2.1 Drug treatment

For treatment, drugs were diluted in cell culture media to the desired final concentration, making sure that DMSO concentrations do not exceed 0.5%. In case of treatment with dabrafenib, media was changed every other day, except for 72 h treatment for metabolic activity assay (3.2.3 Metabolic activity assay for IC50 determination), to ensure constant inhibition.

3.2.2.2 Treatment withdrawal

For treatment withdrawal, cells were carefully washed three times with PBS, incubated for 15 min in medium at 37 °C, followed by three PBS washes and lastly addition of fresh medium. Time of withdrawal was counted from the timepoint fresh medium is added after the last PBS wash.

3.2.3 Metabolic activity assay for IC50 determination

For metabolic activity assays, BT-40 were seeded as indicated in Table 21 in RPMI containing 2% FCS and allowed to settle overnight (O/N). The next day, cells were treated using the D300e Digital Dispenser. In case of DMSO-solved drugs, DMSO concentrations were normalized to the highest-class volume across all treatment conditions to ensure comparability, and final DMSO concentrations were set to not exceed 0.5%. For water-based drugs, Triton X-100 was added to a final concentration of 0.1% before loading on D300e dispense heads and normalized to the highest-class volume across all treatment conditions. 72 h after treatment start, metabolic activity was measured using CellTiter-Glo 2.0. 100 µl reagent were added to each well containing 100 µl of cell culture media, contents were mixed on an orbital plate shaker for 2 min to induce cell lysis followed by 10 min incubation at RT to allow for stabilization of luminescent signal. Following, luminescence signal was measured using the FLUOstar OPTIMA automated plate reader. Cell viability was calculated relative to solvent

control. Dose-response-curves were plotted and IC50/IC75 values were calculated using GraphPad Prims (v8.0.2) with a 4-parameter dose-response model.

3.2.4 Cell counting for growth curve analysis

Cells were seeded as indicated in Table 21 and counted using the Vi-CELL XR using the settings described in Table 20. The mean viable cell number of two technical replicates for each time point and condition was calculated and plotted.

3.2.5 Cell cycle analysis by flow cytometry

For cell cycle analysis, cells were seeded as indicated in Table 21 and harvested through trypsinization using 1 ml trypsin after five days treatment. Once detached, cells were further resuspended in 10 ml medium, yielding 11 ml cell suspension of which 1 ml was aliquoted for cell counting using the Vi-CEL XR (settings see Table 20). The remaining cell suspension was centrifuged for 5 min at 1200 rpm and the supernatant was decanted, leaving approx. 200µl for resuspension of the cells prior to fixation. Cells were fixed and permeabilized by dropwise addition of 1 ml 70% ethanol (ice-cold) while vortexing. After incubation for 1-2 h on ice, cells were centrifuged at 4°C for 5 min at 1200 rpm, washed using 1 ml ice-cold FACS washing buffer (Table 11) and centrifuged at 4°C at 1400 rpm for 5 min. Next, cells were resuspended in 400 µl FACS staining solution (Table 11) and incubated at 37°C for 20 min with gentle shaking in the dark. Of note, in case of highly variable cell numbers across treatment conditions, volume of FACS staining solution was adjusted to ensure equal staining efficacy, meaning e.g. if $1x10^6$ cells were resuspended in 400 µl staining solution, $2x10^6$ cells were resuspended in 800 µl. After staining, cells were centrifuged at 1400 rpm for 5 min at 4 °C, resuspended in 130 µL ice-cold PBS and subjected to measurement by BD FACS Canto II analyzer. 20 000 single cells were analyzed and PI fluorescence was acquired using the PE filter setting. Analysis was performed using the FlowJo® analysis software (v10.9.0). FACS experiments were carried out at the Flow Cytometry Core Facility, DKFZ, Heidelberg, Germany.

3.2.6 Quantitative reverse transcription real-time PCR (RT-qPCR)

3.2.6.1 RNA isolation

For RT-qPCR, RNA was extracted using the RNeasy Mini Kit with on-column DNA digestion according to the manufacturer's instructions. In case of cell culture samples, cells were seeded as indicated in Table 21 and following treatment directly lysed in the cell culture vessel. In case of tumor tissue samples, the TissueLyser II was used for mechanical tissue dissociation with two cycles at 20 Hz for 2 min. Following isolation, RNA concentrations were determined using a NanoDrop spectrometer.

3.2.6.2 cDNA synthesis

cDNA was synthesized from 100 ng RNA input using the RevertAid First Strand cDNA Synthesis Kit following the manufacturer's protocol using random hexamer primers.

3.2.6.3 RT-qPCR

RT-qPCR was performed in a 96-well qPCR reaction plate using 15 µl ml qPCR mastermix (Table 11), 5 µl cDNA (1:10 diluted) and water up to 20 µl. Primers used are listed in Table 7. The reaction was run and signal amplification measured using an ABI 7500 Real Time PCR cycler with ABI 7500 Software (v2.3.) with settings described in Table 22.

Table 22 RT-qPCR run setup

Temperature [°C]	Time
50	2 min
95	10 min
40 cycles	
95	15 s
60	1 min
Melting curve (continuous)	
95	15 sec
60	1 min
95	30 sec
60	15 sec

The ΔΔCt method was used for relative quantification with *ACTB* and *TBP* as housekeeping genes for all *in vitro* samples. For *in vivo* xenograft tumor samples only *ACTB* was used as *TBP* primers were not human specific and would also recognized mouse mRNA, falsifying the quantification. In case genes of interest were undetected in some samples, Ct values for these samples were set to 40 (max. number of cycles).

3.2.7 Protein extraction and immunoblotting

3.2.7.1 Protein extraction and sample preparation

Cells were seeded as indicated in Table 21. For protein extraction, cells were washed with PBS followed by lysis directly in the well using SDS lysis buffer (150-200 µl per well in case of 6-well plate; Table 11). Next, lysates were incubated at 95°C for 5 min with gentle shaking (350 rpm), centrifuged at 14 000 rpm for 5 min at 4°C to clear any debris and supernatants were transferred into a new reaction tube.

Protein concentration was determined using the Pierce™ BCA Protein Assay Kit according to the manufacturer's instructions using a 1:5 diluted sample aliquot. After BCA reaction, absorbance was measured at 570 nm with background correction at 650 nm using the FLUOstar OPTIMA automated plate reader. Protein concentrations were calculated based on a BSA standard-curve using OPTIMA Microplate reader software. For western blot analysis, 15-30 µg protein were used. Sample were prepared for SDS polyacrylamide gel electrophoresis by dilution in SDS lysis buffer and addition of 1 µl of a saturated bromophenolblue solution and were boiled at 95°C for 5 min. In case protein samples harvested with the array lysis buffer (Table 11) were used, samples were prepared by dilution in de-ionized H_2O and addition of 1 µl of a saturated bromophenolblue solution and 5X Laemmli buffer (1/5 of the total sample volume, Table 11).

3.2.7.2 SDS polyacrylamide gel electrophoresis (SDS-PAGE) and immunoblotting

For SDS-PAGE, 7% or 10% acrylamide separating gels topped with stacking gels were used (Table 23). Electrophoresis chambers were assembled, filled with 1x SDS running buffer (Table 11), and samples or 7 µl Precision Plus Protein™ Kaleidoscope™ were loaded. Gels

were then run at 80 V for approx. 15 min until samples passed through the stacking gel, then voltage was increased to 120 V for protein separation until bromphenolblue running front reached the end of the gel.

Table 23 Separating and stacking gel recipe

Reagent	7% separating gel	10% separating gel	Stacking gel
De-ionized H_2O	3.8 ml	3 ml	1.538 ml
Running gel buffer (Table 11)	1.875 ml	1.875 ml	-
Stacking gel buffer (Table 11)		-	625 µl
20% SDS (Table 11)	37.5 µl	37.5 µl	12.5 µl
40% Acrylamide/Bis solution (Table 10)	1.7 ml	2.5 ml	335 µl
10 % APS (Table 11)	75 µl	75 µl	25 µl
TEMED	5 µl	5 µl	2.5 µl

After SDS-PAGE, proteins were transferred from the gel to a PVDF membrane using the Trans-Blot Turbo RTA Mini 0.45 µM LF PVDF Transfer Kit with the Trans-Blot Turbo Transfer System for 7 min at 1.3 A (one gel) or 2.5 A (two gels) and up to 25 V.

3.2.7.3 Immunodetection

After immunoblotting, membranes were blocked either in blocking milk (Table 11) or 5% BSA (Table 11) depending on the primary antibody used (Table 8) for 1h at RT. Following, membranes were incubated with primary antibody either O/N at 4°C or for 1-2h at RT as specified in Table 8. Secondary antibody (Table 8) incubation was done for 1-2h at RT. After primary antibody and secondary antibody incubation, membranes were washed with TBS-T (Table 11) three times for 10 min. HRP-conjugated secondary antibodies were then detected using the Amersham ECL Prime Western Blotting Detection Reagent according to the manufacturer's instructions with the Azure c400 image system. Images were quantified using ImageJ.

3.2.8 RNA sequencing, data processing and analysis

3.2.8.1 Sample generation

BT-40 were seeded as indicated in Table 21. Samples were harvested and RNA isolated as describe in “3.2.6.1 RNA isolation”. RNA sample integrity after isolation was assessed using the 2100 Bioanalyzer and Agilent RNA 6000 Nano Kit according to the manufacturer’s instructions.

3.2.8.2 RNA sequencing

RNA sequencing was performed by the NGS Core Facility at the DKFZ and the text passage below was provided by the core facility.

“Sequencing libraries were prepared using the Illumina TruSeq mRNA stranded Kit following the manufacturer's instructions. In brief, mRNA was purified from 500 ng of total RNA using oligo(dT) beads. Following, poly(A)+ RNA was fragmented to 150 bp, converted to cDNA, end-repaired, adenylated on the 3′ end, adapter ligated and amplified with 15 cycles of PCR. The final libraries were validated using Qubit and TapeStation. 2x 100 bp paired-end sequencing was performed on the Illumina NovaSeq 6000 according to the manufacturer's instructions.”

3.2.8.3 Data processing and filtering

FASTq files generated from the RNAseq run were submitted to the OTP RNAseq pipeline[163] for read-trimming, alignment to the hg19/GRCh37 human genome and calculation of raw read counts, TPM and FPKM values. Afterwards, data was filtered to only include protein-coding genes, using the Ensembl biomart tool. Additionally, lowly expressed genes (TPM < 1 in all samples) were excluded.

3.2.9 LC-MS/MS proteomics and phosphoproteomics data generation and processing

3.2.9.1 Proteomics and phosphoproteomics sample generation

For proteomics and phosphoproteomics analyses cells were seeded as indicated in Table 21. For protein extraction, cells were washed once with TBS and lysed directly in the plate using

hot SDC lysis buffer (Table 11). Following, samples were boiled at 95°C, sonicated using a tip probe sonicator (1 s pulses, 40% power for 1 min) and precipitates were cleared by centrifugation at 14000 rpm for 10 min. Protein concentration was measured with the PierceTM BCA Protein Assay Kit according to the manufacturer's instructions using 1:4 diluted samples. After BCA reaction, absorbance at 570 nM with background correction at 650 nm was measured using the FLUOstar OPTIMA automated plate reader and protein concentrations were calculated based on a BSA standard-curve using OPTIMA Microplate reader software.

3.2.9.2 Proteomics sample processing

For proteomics analysis, 50 µg protein in 90 µl SDC lysis buffer (Table 11) was used as input for the sample processing. To reduce and alkylate cysteine residues, 10 µl proteomics reduction buffer (Table 11) was added, followed by incubation at 45°C and 1000 rpm for 5 min. Next, proteins were digested using Trypsin/Lys-C mix (enzyme:protein ratio 1:50, Table 11) overnight (16-18 h) at 37°C and 1400 rpm. Trypsin was inactivated using 500 µl (=5 volumes) 1% TFA (Table 11). 20 µg of digested protein (= 240 µl digested protein solution) was then used for peptide clean up on self-made SDB-RPS stage tips. These SDB-PRS stage tips were prepared by stuffing a 200 µl pipette tip (without filter) with 3 layers of an SDB-RPS extraction disk using a modified blunt-end syringe (5 ml, 14 gauge). For centrifugation, a custom 3D-printed adapter was used. SDB-RPS stage tips were equilibrated prior to peptide loading using 150 µl acetonitrile (Table 11), followed by 150 µl SDB-RPS equilibration buffer 1 (Table 11), followed by 150 µl SDB-RPS equilibration buffer 2 (Table 11), which were subsequently spun through the stage tips at 1500 rcf for 7 min. Next, the peptide solution was loaded and SDB-RPS stage tips were centrifuged at 1500 rcf for 50 min. After peptide loading, washing was performed using 150 µl proteomics wash buffer 1 (Table 11) followed by 150 µl Proteomics wash buffer 2 (Table 11), which were subsequently spun through at 1500 rcf for 7 min. Finally, peptides were eluted in two elution steps each using 45 µl proteomics elution buffer (Table 11) at 1500 rcf for 7 min. Eluted peptides were dried using a vacuum concentrator at 45 °C and suspended in 10 µl MS resuspension buffer (Table 11). After sonication in an ultrasound bath

for 15 min, peptide concentration was determined using the Pierce™ Quantitative Colorimetric Peptide Assay Kit according to the manufacturer's instructions and measured using the FLUOstar. Peptide concentrations were calculated based on a standard-curve using the Omega microplate reader software. A total amount of 0.5 µg was subjected to LC-MS/MS analysis.

3.2.9.3 Phosphoproteomics sample processing

For phosphoproteomics analysis, 500 µg protein in 500 µl SDC lysis buffer (Table 11) were used. To reduce disulfide-bonds 10 µl 500 mM DTT (Table 11) were added and samples were incubated at 57°C for 20 min. Following, 40.8 µl 500 mM IAA (Table 11) were added and samples were incubated at RT for 30 min in the dark to alkylate free cysteine residues. For sample clean-up, proteins were precipitated using acetone. For this, 2.5 ml (=5x the sample volume) ice-cold 100% acetone were added to the samples, mixed by vortexing and incubated at -20°C for 1h. Afterwards, samples were centrifuged at 3000 rcf at 4°C for 5 min. Supernatant was decanted and the pellet resuspended in 500 µl ice-cold 90% acetone (Table 11), followed by centrifugation at 3000 rcf at 4°C for 5 min. Supernatant was discarded and tubes were left open until remaining acetone was evaporated. Then the pellet was resuspended in 500 µl SDC lysis buffer (Table 11) and proteins were digested using Trypsin/Lys-C mix (enzyme:protein ratio 1:100, Table 11) overnight (16-18 h) at 37°C and 1400 rpm. After overnight incubation, 5 µl formic acid were added to inactivate trypsin and precipitates were cleared through centrifugation at 21000 rcf for 5 min. Following, the supernatant was transferred to a new reaction tube and peptides were dried using a vacuum concentrator at 45°C for 1.5 h. Dried peptides were then resuspended in 150 µL Binding/Equilibration Buffer provided with the High-Select™ TiO2 Phosphopeptide Enrichment Kit and phospho-peptides were enriched using this kit according to the manufacturer's instructions. Enriched phospho-peptides were then dried using a vacuum concentrator at 45°C for 30 min and resuspended in 10 µl MS resuspension buffer (Table 11). After sonication in an ultrasonic bath for 15 min, sample quality was checked using a NanoDrop spectrometer. For LC-MS/MS analysis 2 µl of the peptide solution was used.

3.2.9.4 LC-MS/MS data acquisition

Loading of samples into the mass spectrometer and parameter setup was done by Stefan Pusch and David Vonhören (Clinical Cooperation Unit Neuropathology, DKFZ) and the text in this section is adapted from information and text passages provided by David Vonhören.

First, samples were separated by a NanoElute HPLC system using a 90 min gradient. Following, samples were subjected to MS/MS analysis using a timsTOF pro mass spectrometer using the following settings: Ion accumulation and ramp time were set to 50 ms, ions with a mobility ranging from 1/K0 = 0.85-1.3 V s cm^{-2} were included. Precursors reaching an intensity threshold of 1500 arbitrary units (a.u.) were classified as suitable. Resequencing of low-abundance precursors was performed, taking dynamic exclusion of 40 s into account, until a value of 20000 a.u. was reached. Ions with a mass range of 100-1700 m/z were selected for MS/MS fragmentation. A 2 Th window or a 3 Th window was used for ions with m/z < 700 or mz > 700 respectively. Quadropole switching events were synchronized with the precursor elution profile for isolation. Collision energy for dissociation was lowered linear as a function of increasing ion mobility, ranging from 59 eV (1/K0 = 1.6 V s cm^{-2}) to 20 eV (1/K0 = 0.6 V s cm^{2}). Single charged precursor ions were excluded using a polygon filter.

3.2.9.5 Data processing with MaxQuant

Data processing using MaxQuant was done by Dennis Friedel (Department of Neuropathology, University Heidelberg) and the text passage below was provided by him.

“For raw MS data processing the command line version of the MaxQuant software (v1.6.17.0)[164] was used on a Linux machine with 128 physical cores (AMD EPIC 75032 32-Core Processor) and 256Gb of RAM. Spectra were searched against the human Uniprot database of canonical protein sequences downloaded in March 2022. Default settings were used for the parameters enzyme specificity, FDR on peptide spectral match, protein level precursor as well as fragment ion mass tolerance remained on default settings. For whole proteome analysis the variable modifications Aminoacid deamidiation (NQ), Oxidation (M) and Acetyl (Protein N-term) and MaxQuant internal normalization algorithm MaxLFQ and the

search algorithm “Match between runs” were turned on. For the phosphoproteome analysis serine, threonine and tyrosine phosphorylation (STY) was included to the variable modification, the MaxLFQ and the search algorithm “Match between runs” remained off.”

3.2.9.6 Further data processing and filtering

Proteomics data was further processed before analysis using the R package “DEP” (v1.18.0).[165] First, data was filtered to exclude proteins only identified by a modification site, reverse hits or possible contaminants. Additionally, only proteins detected in at least 2/3 replicates per condition were kept for further analysis. Lastly, missing values were imputed through random draws from a gaussian distribution centered around a minimal value.

Phosphoproteomics data was further processed before analysis using the R package “PhosR” (v1.6.0).[166,167] First, data was filtered to exclude reverse hits and possible contaminants. Additionally, only peptides detected in at least 2/3 replicates per condition were kept for further analysis. Missing values were imputed through site- and condition-specific as well as tail-based imputation. Lastly, phosphoproteomics data was batch-corrected using a set of stably phosphorylated sites[166,167] and implementation of the Removing Unwanted Variation-III method.[168]

3.2.10 Analysis of cytokine secretion using Luminex-based multiplex assay

Samples for this assay were harvested by myself. The Luminex-based multiplex assay was carried out by Melanie Langhammer and Sebastian Halbach (Institute of Molecular Medicine and Cell Research (IMMZ), Faculty of Medicine, University of Freiburg).

For conditioned media (CM) harvesting, BT-40 cells were seeded as indicated in Table 21. CM for each condition and timepoint was collected from three 6 cm dishes, yielding approx. 9 ml of CM per condition. Cells were counted at the time of CM harvesting using the Vi-CELL XR using the settings described in Table 20. To clear cellular debris, CM was centrifuged at 1500 rpm for 15 min and stored at -80 °C in aliquots until use.

For the Luminex-based multiplex assay, two custom detection antibody multiplexes were used as indicated in Table 14. For both multiplexes, the Bio-Plex Pro Reagent Kit 3 was used with either the Bio-Plex Pro HuCSP standard or the Bio-Plex Pro Human Chemokine standard (as indicated in Table 14). The assay was measured using the Bio-Plex 200 System.

Protein concentrations in pg/ml were normalized to viable cell counts to account for differences in cell densities across the different conditions and timepoints.

The area under the curve (AUC) of cytokine secretion during withdrawal was calculated using the "approxfun" and "integrate" function of the R package "stats" (v4.2.2)[169] with default settings. The AUC-log2FC was calculated as follows:

$AUC - log2FC = log2(AUC_{dabra\,wd} + 1) - log2(AUC_{DMSO\,wd} + 1)$, where $AUC_{dabra\,wd}$ and $AUC_{DMSO\,wd}$ refer to the AUC of cytokine secretion during dabrafenib or DMSO withdrawal respectively.

3.2.11 Kinase phosphorylation array

BT-40 cells were seeded as indicated in Table 21. For protein extraction, cells were lysed directly in the dish using 500 µl array lysis buffer (Table 11) with gentle rocking at 4°C for 30 min. Lysates were transferred to a reaction tube, centrifuged at 14000 rcf for 5 min and supernatants transferred to a new reaction tube. Protein concentration was determined using the Pierce™ BCA Protein Assay Kit according to the manufacturer's instructions using a 1:5 diluted sample aliquot. After BCA reaction, absorbance was measured at 570 nm with background correction at 650 nm using the FLUOstar OPTIMA automated plate reader (BMG Labtech) and protein concentrations were calculated based on a BSA standard-curve using OPTIMA Microplate reader software.

The Proteome Profiler Human Phospho-Kinase Array Kit was used according to the manufacturer's protocol using 400 µg of protein lysate per array set. Arrays were visualized using the Azure c400 imaging system. First, the detection reagents provided with the kit were used. Following, a second visualization was performed using the Amersham ECL Prime

Western Blotting Detection Reagent to achieve better signal intensity. Quantification was done using ImageJ.

3.2.12 Stimulation with recombinant cytokines

Cells were treated for 1 h with 100 ng/ml of recombinant human CCL2, CX3CL1, CXCL10, CCL7 or a combination of all four.

3.2.13 Treatment with neutralizing antibodies

For cell count experiments, cells were either treated with neutralizing antibodies in combination with dabrafenib or after dabrafenib treatment. For western blot analysis, cells were treated with neutralizing antibodies for 24 h after dabrafenib treatment. Antibodies neutralizing CCL2 (0.5 µg/ml), CX3CL1 (0.25 µg/ml), CXCL10 (0.25 µg/ml) and CCL7 (0.1 ng/ml) or mouse IgG (2 µg/ml) were used.

3.2.14 BT-40 – HMC3 transwell co-culture

For co-culture experiments, cells were seeded as indicated in Table 21. Transwell inserts were placed in wells containing only media but no cells for seeding and upon experiment start transferred to wells containing BT-40 cells. After seven days of co-culture (medium change every 2-3 days) viable cell numbers of BT-40 cells in the bottom wells of the transwell chamber were counted using the Vi-CELL XR using the settings described in Table 20. The mean viable cell number of two technical replicates for each time point and condition was calculated and plotted.

3.2.15 Migration assay

3.2.15.1 Conditioned media collection for transwell assay

BT-40 cells were seeded as indicated in Table 21 for CM collection. CM was collected after five days of treatment, 24 h after the last media change, and 24 h after treatment withdrawal. After collection, CM was centrifuged for 5 min at 1200 rpm and filtered using a 0.22 µM sterile filter to clear cellular debris.

3.2.15.2 Transwell migration assay

Three days prior to experiment start, 70-80% confluent HMC3 were split 1:4 and switched to RPMI containing 2% FCS. For the transwell migration assay, transwell inserts (24-well format, 8 µM pore size) were placed into 24-well companion plates. HMC3 cells were seeded into the upper transwell chamber ($0.1x10^6$ cells in 100 µl) and allowed to settle for 30 min in the cell culture incubator. Then, 600 µl CM or media with different FCS concentrations (0% as negative control, 2% as control, 10% as positive control) were added to the bottom well of the transwell chamber. For cytokine-neutralization experiments, neutralizing antibodies were added to the CM and the CM-antibody mixture was incubated in a heatblock at 37°C for 30 min prior to addition of CM-antibody mixture to the bottom of the transwell chamber (1 µg/ml anti-CCL2, 0.5µg/ml anti-CX3CL1, 0.5 µg/ml anti-CXCL10 and 0.2 ng/ml anti-CCL7 or 2 µg/ml mouse IgG). Cells were allowed to migrate overnight (16-18 h) before fixation and staining.

3.2.15.3 Fixation, staining and imaging

After O/N incubation, media inside the transwells was discarded and transwells were gently washed using PBS. Then, transwells were transferred to a new plate containing 500 µl/well 4% PFA (Table 11) for fixation for 15 min. Following, transwells were washed by dipping 3-5 times into PBS. Next, cells in the inside of the transwell (i.e. non-migrated cells) were removed with a cotton swab and cell debris was removed by dipping 3-5 times into PBS. Then, transwells were placed into wells containing 500 µl 0.5% Triton-X (Table 11) for 20 min for cell permeabilization. Following, cells were washed by dipping 3-5 times into PBS, transwells were place in wells containing 500 µl DAPI staining solution (Table 11) and incubated for 5 min in the dark. Following, cells were washed by dipping 3-5 times into PBS and once into ddH_2O. Then, membranes were cut out of the transwell using a scalpel, transferred to glass slides and mounted in ProLong Gold Antifade Mountant, with the bottom side of the membrane (i.e., the side containing the migrated cells) facing up towards the coverslip. After overnight curation of the mounting media at RT in the dark, slides were imaged using the Zeiss LSM 710 confocal microscope in the Light microscopy facility at the DKFZ.

Number of migrated cells (i.e., number of DAPI stained nuclei on the bottom side of the transwell membrane) were counted either manually using ImageJ or automated using CellProfiler. The CellProfiler pipeline for automated counting was generated by Sonja Herter (CCU Pediatric Oncology, DKFZ).

3.2.16 BT40 *in vivo* rebound model sample generation and analysis

In vivo sample generation (3.2.16.1-3.2.16.3) was carried out at the University College London by Lei Cao (Developmental Biology and Cancer Programme, UCL GOS Institute of Child Health) and the text in these sections is adapted from information and text passages provided by Lei Cao and Romain Guiho (Developmental Biology and Cancer Programme, UCL GOS Institute of Child Health). All mouse procedures were performed under license (PP8308129), following UK Home Office Animals (Scientific Procedures) Act 1986 and local institutional guidelines (UCL ethical review committee) and ARRIVE guidelines.

3.2.16.1 Intracranial tumor cell transplantation

For generation of BT-40 orthotopic xenografts, six-week-old female NOD scid gamma (NSG) mice, purchased from Charles River UK, were used. $1.5x10^5$ BT-40 cells (expressing luciferase and GFP) were injected intracranially using a Hamilton syringe, at the following coordinates: bregma + 1 mm anterior, 1.5 mm lateral and 3 mm ventral. Tumor growth was monitored through bioluminescence imaging. For this, 150 mg/kg Firefly D-Luciferin was injected subcutaneously 10 min before imaging using the IVIS Lumina III In Vivo imaging system. Images were analyzed using the Living Image Software.

3.2.16.2 Dabrafenib treatment and withdrawal

Treatment was started for each animal individually once bioluminescence signal reached a radiance of $>10^7$ photons/sec/cm^2/sr. Animals were treated once daily per oral for six days with 100 mg/kg dabrafenib.

3.2.16.3 Sample harvesting

Samples during dabrafenib treatment were harvested 2 h after the last dabrafenib administration. Treatment withdrawal samples were harvested three days after the last dabrafenib administration. Untreated control samples were isolated when bioluminescence signal reached a radiance of $>10^7$ photons/sec/cm^2/sr. Tumor tissue was dissected under fluorescent guidance, flash frozen and stored at -80°C until further use for subsequent RNA extraction.

3.2.16.4 Sample analysis

RNA isolation, cDNA synthesis and RT-qPCR were performed as described in "3.2.6 Quantitative reverse transcription real-time PCR (RT-qPCR)". All primers used for RT-qPCR (Table 7) were human-specific.

3.2.17 Statistics, data analysis and visualization

Statistical analysis was either performed using GraphPad Prism (v8.0.2) or R Studio (R version 4.2.2). All experiments were performed in at least three independent biological replicates unless otherwise specified and number of replicates is indicated in the respective figure legends. Furthermore, the statistical tests performed are indicated in the respective figure legend. Unless otherwise specified, significance was defined as p-value or adj-p-value ≤ 0.05.

Graphical depiction of results was done using GraphPad Prism and R Studio using the R package "ggplot2" (v3.4.2)[170] unless otherwise specified.

3.2.17.1 RNAseq data analysis

Principal component analysis (PCA) was performed using log2-transformed TPM+1 values with the "prcomp" function of the R package "stats" (v4.2.2)[169] with default settings and visualized using the R package "ggbiplot" (v0.6.2).[171]

The MPAS score was calculated using FPKM values as previously described.[172] In brief, the gene expression z-score of ten MAPK-specific genes was calculated within each sample (*PHLDA1, SPRY2, SPRY4, DUSP4, DUSP6, CCND1, EPHA2, EPHA4, ETV4,* and *ETV5*).[172]

Then the MPAS score was calculated using the following formula: $MPAS - score = \frac{\sum_i^z}{\sqrt{n}}$, where z_i is the z-score of each gene and n is the number of genes (i.e. 10).[172]

Using the raw read counts, differential gene expression (including fold-changes, standard error, p-value and adj-p-value) was calculated using the DeSeq2 module (version 3)[173] on GenePattern[174] with default settings.

Longitudinal k-means clustering of differentially expressed genes, using log2FCs, was performed using the R package "kml" (v2.4.6)[175] with 20 iterations, only including genes with an adj-p-value ≤ 0.01 for at least one timepoint. Up to 20 clusters were tested and five clusters were chosen because this yielded the highest Calinski-Harabasz index.[176]

GO-term enrichment analysis of genes in up- or downregulated clusters, based on the longitudinal k-means clustering (mean cluster log2FC < -1.5 or > 1.5), was performed and visualized using ClueGo (v2.5.9)[177] in CytoScape (v3.9.1).[178] Enrichment of molecular function ontology terms was calculated using the right-sided hypergeometric test with Bonferroni step down p-value correction. GO-term groups were defined based on shared genes (Kappa Score: 0.4) and named based on the GO-Term with the highest percentage of mapped genes.

ssGSEA analysis using TPM values was performed using the ssGSEA module (v10.1.0)[179] on GenePattern[174] with default settings except for min. gene set size which was set to 1. Gene sets related to proliferation, cell cycle, RTKs and MAPK signaling were taken from the MSigDB (v7.5.1) C2 subcollection CP (Broad Institute). Gene sets were annotated in groups by Romain Sigaud (CCU Pediatric Oncology, DKFZ) and myself. ssGSEA scores were transformed into z-scores and visualized in a heatmap using the R package "ComplexHeatmap" (v2.12.1).[180,181]

3.2.17.2 Proteomics data analysis

Principal component analysis (PCA) was performed using log2-transformed, imputed protein intensities as described in "3.2.17.1 RNAseq data analysis".

The MAPK activity score based on proteomics data contained a set of proteins shown to be downregulated upon MAPK inhibition.[182] The activity score was calculated using log2-transformed, imputed protein intensities using ssGSEA analysis as described in "3.2.17.1 RNAseq data analysis".

Differential protein expression was calculated from log2-transformed, imputed protein intensities using the R package "DEP" (v1.18.0)[165] with default settings. This package was run under R version 4.1.3.

Longitudinal k-means clustering of differentially expressed proteins, using log2FC, was performed as described in "3.2.17.1 RNAseq data analysis". Two clusters were chosen because this yielded the highest Calinski-Harabasz index.[176]

GO-term enrichment analysis of proteins in up- or downregulated clusters, based on the longitudinal k-means clustering (mean cluster log2FC < -1.5 or > 1.5), was performed and visualized as described in "3.2.17.1 RNAseq data analysis".

3.2.17.3 Phosphoproteomics data analysis

Principal component analysis (PCA) was performed using log2-transformed, imputed peptide intensities as described in "3.2.17.1 RNAseq data analysis".

As phosphophroteomics-based MAPK activity score the MEK1 PTM-SEA signature from the PTMsigDB collection (v2.0.0)[183] was use. The activity score was calculated using log2-transformed, imputed peptide intensities using ssGSEA analysis as described in "3.2.17.1 RNAseq data analysis".

Differential phosphorylation was calculated based on log2-transformed, imputed peptide intensities using the R package "PhosR" (v1.6.0).[166,167]

For KSEA analysis, only phospho-peptides with a significant regulation at a given timepoint relative to control (adj-p-value ≤ 0.05) were used. Kinase enrichment z-scores and p-values were calculated with the KSEA app using the PhosphoSitePlus and NetworkKIN kinase-

substrate datasets and default parameters.[184–187] z-scores were visualized in a heatmap using the R package “ComplexHeatmap” (v2.12.1).[180,181]

4 Results

4.1 *In vitro* rebound modelling

In order to investigate possible rebound driving mechanisms, I first tested several patient-derived pLGG *in vitro* models to establish a MAPKi withdrawal rebound model which fulfills the following three criteria:

1) Response upon MAPKi treatment (i.e. decreased cell proliferation or increased cell death)
2) Cell regrowth upon treatment withdrawal
3) Cell regrowth after MAPKi withdrawal is faster than after withdrawal of chemotherapy

4.1.1 *In vitro* rebound model development

To develop an *in vitro* MAPKi withdrawal rebound model, four patient-derived models, listed in Table 24, were tested.

Table 24 Patient-derived *in vitro* models

Cell line	Alteration	Patient tumor	Cellular state
DKFZ-BT66[64]	*KIAA1549:BRAF*	Pilocytic astrocytoma	Senescent or proliferating (induced by SV40-TAg expression)
DKFZ-BT308[63]	*KIAA1549:BRAF*	Pilocytic astrocytoma	Senescent or proliferating (induced by SV40-TAg expression)
DKFZ-BT314[63]	*BRAF*^{V600E}	Pilocytic astrocytoma	Senescent or proliferating (induced by SV40-TAg expression)
BT-40[80]	*BRAF*^{V600E}, *CDKN2A/B*del	Juvenile pilocytic astrocytoma	Proliferating

MAPK inhibitors used for rebound model generation included the BRAF type 1 ½ inhibitor dabrafenib, which was used in *BRAF*^{V600E}-driven models, and the MEK inhibitor trametinib, which was used in *KIAA:BRAF* fusion-driven models. As SOC chemotherapy controls, vincristine (VCR) and carboplatin as single or combination treatment were used. Drug concentrations were chosen within clinically achievable ranges, based on pharmacokinetic (PK) data (Table 25), focusing on maximum plasma concentration (C_{max})[188–190] and plasma-protein-binding (PPB), as well as effect *in vitro*. Effect *in vitro* was assessed based on

metabolic activity in BT-40 and a MAPK-reporter assay[85] in DKFZ-BT66[81], as metabolic activity is not an applicable read-out for the SV40TAg-based models.[81,85,89]

Table 25 Pharmacokinetic data for drugs used
Plasma-protein-binding was taken from DrugBank[52] ($unbound\ Cmax = Cmax \times \frac{100-PPB}{100}$).
This table was adapted from Kocher *et al.*, under review

Inhibitor	C_{max} [nM]	Plasma-protein-binding (%)	Unbound C_{max} [nM]	Reference for C_{max}
Dabrafenib	2856.2	99.7	8.57	PMID: 37441736
Trametinib	36.07	97.4	0.94	PMID: 37441736
Vincristine	69.43	75	17.36	PMID: 32635465
Carboplatin	59000	25-50	29500-44250	PMID: 8137457

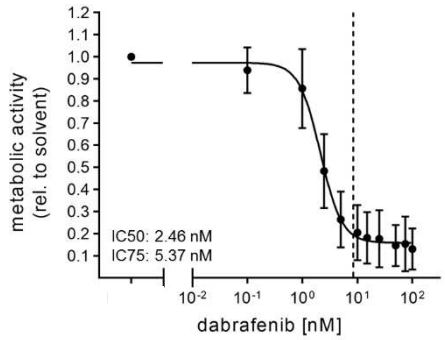

Figure 6 Dabrafenib dose-response curve in BT-40
Metabolic activity was measured after treatment for 72 h with increasing dabrafenib concentrations. Metabolic activity is depicted relative to solvent control (DMSO) as mean±SD of three independent biological replicates. Dashed line indicates unbound C_{max} concentration. Absolute inhibitory concentrations (IC)50 and IC75 values were calculated using a 4-parameter dose-response model
This figure was adapted from Kocher *et al.*, under review

Dabrafenib concentrations tested during the rebound model development were 5 nM and 10 nM. 5 nM corresponded to the absolute inhibitory concentration (IC)75 in BT-40 based on metabolic activity (Figure 6) and is within the unbound fraction of the C_{max} (Table 25). 10 nM dabrafenib corresponded to the IC_{max} (Figure 6) and is within the C_{max} (Table 25). For trametinib, 1 nM and 5 nM were chosen, as they are within clinically achievable ranges (Table 25) and lead to > 50% MAPK pathway inhibition in DKFZ-BT66 as previously shown by our group (DKFZ-BT66 proliferating state: IC50 = 2.1 nM; DKFZ-BT66 senescent state: IC50 = 0.5 nM).[81]

Treatment of the three PA-derived cell models BT-66, -308, and -314 did not decrease cell proliferation or induce cell death compared to untreated cells in either state (senescent or proliferating), as observed by viable cell counts (Figure 7). Furthermore, no changes in viable cell numbers (i.e., no rebound) were observed after treatment stop (Figure 7). Due to the lack of effect during MAPKi treatment (i.e., rebound model criteria #1) and the absence of regrowth

or increased proliferation (i.e., rebound growth) upon treatment withdrawal (i.e., rebound model criteria #2), these models were not suitable to study rebound growth *in vitro* and could therefore not be used further in this study.

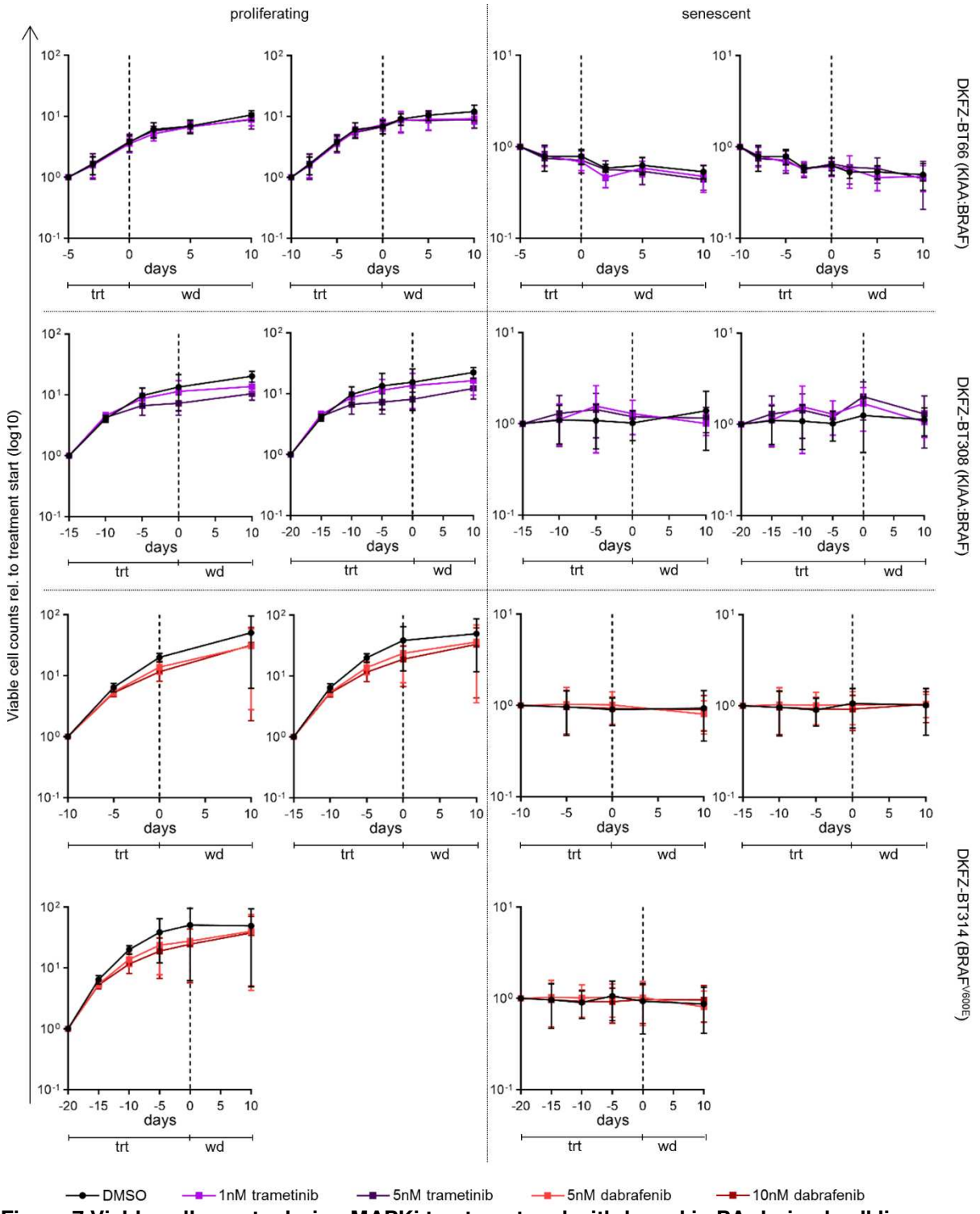

Figure 7 Viable cell counts during MAPKi treatment and withdrawal in PA-derived cell lines
Cells were treated (trt) with trametinib or dabrafenib, as indicated, for different durations followed by ten days of withdrawal (wd). Dashed lines in the graphs indicate withdrawal timepoint. Viable cell counts are normalized to treatment start (first timepoint shown in each graph). Data is shown on a logarithmic scale (base 10) as mean±SD (n=3 independent biological replicates)
This figure was adapted from Kocher *et al.*, under review

In contrast, treatment of BT-40 cells with 5 nM dabrafenib for five or ten days decreased cell proliferation as indicated by static viable cell numbers (Figure 8). Treatment with 10 nM dabrafenib for five or ten days additionally lead to decreased viable cell numbers compared to treatment start (Figure 8), suggesting cell death. Tumor cell regrowth was observed within ten days after dabrafenib withdrawal in all conditions except ten days treatment with 10 nM dabrafenib (Figure 8).

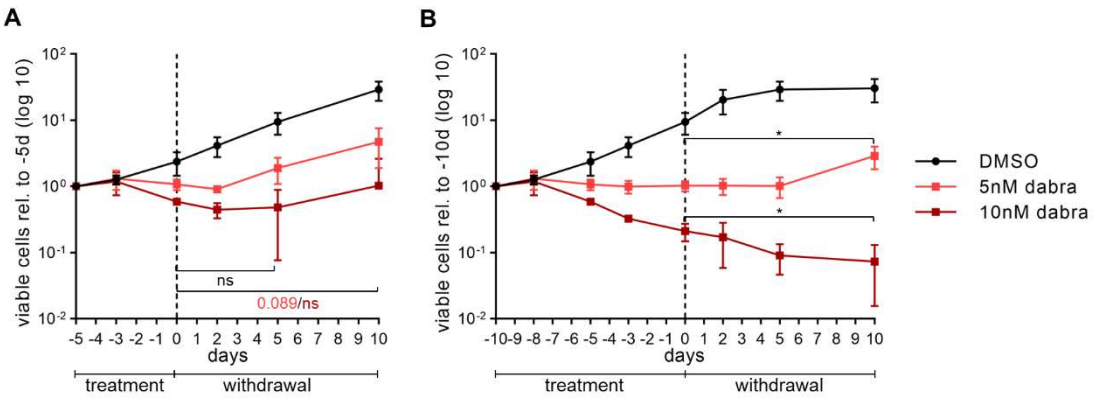

Figure 8 BT-40 viable cell counts during dabrafenib treatment and withdrawal
BT-40 were treated for five (A) or ten (B) days with dabrafenib (dabra) followed by ten days of withdrawal. Dashed line indicates withdrawal timepoint. Viable cell counts are normalized to treatment start (-5d (A) or -10d (B)). Data is shown on a logarithmic scale (base 10) as mean±SD (n=3 independent biological replicates). Unpaired two-sided t-test; ns: not significant; no indication: not tested
Part (A) of this figure was adapted from Kocher *et al.*, under review

As BT-40 fulfilled the first two criteria of a successful rebound model, I next investigated, whether regrowth after dabrafenib withdrawal is faster compared to SOC chemotherapy withdrawal. As SOC chemotherapy treatment, 0.75 nM VCR or 40 µM carboplatin, both corresponding to the respective metabolic IC50 (Figure 9) and within clinically achievable concentrations (< unbound C_{max}; Table 25), were used. Furthermore, combination of 1 nM VCR and 4 µM carboplatin, corresponding to the combination metabolic IC50 when combined in the ratio of the unbound C_{max} of each drug (Figure 9), was used. All three treatments decreased cell proliferation during five or ten days of treatment, while regrowth upon treatment withdrawal within ten days only occurred in case of five days treatment with 0.75 nM VCR (Figure 10), indicating a delay in tumor cell recovery after SOC chemotherapy withdrawal compared to dabrafenib withdrawal.

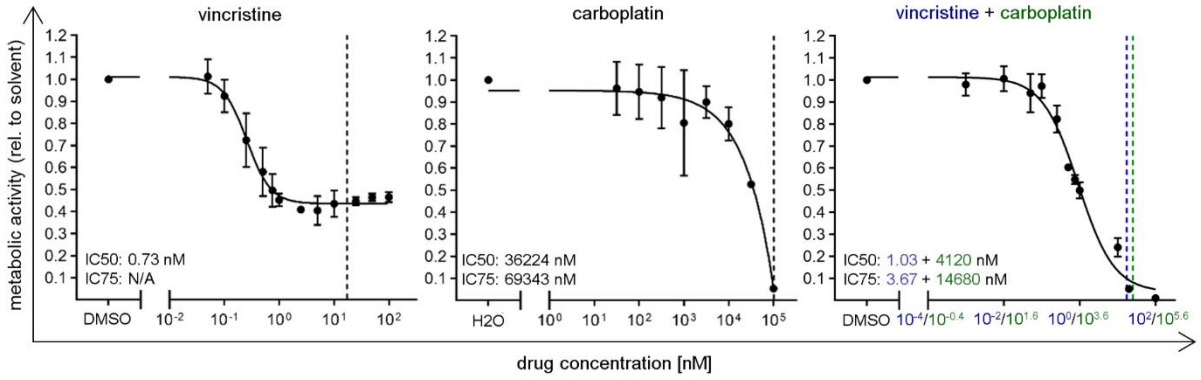

Figure 9 Chemotherapy dose-response curves in BT-40
Metabolic activity was measured after treatment for 72 h with increasing concentrations of vincristine and carboplatin as single agents or in a combination (ratio: 1:4000). Metabolic activity is depicted relative to solvent control (DMSO or H_2O) as mean±SD of three biological replicates. Dashed line indicates unbound C_{max} concentrations. Absolute inhibitory concentrations (IC)50 and IC75 values were calculated using a 4-parameter dose-response model. N/A: not applicable
This figure was adapted from Kocher *et al.*, under review

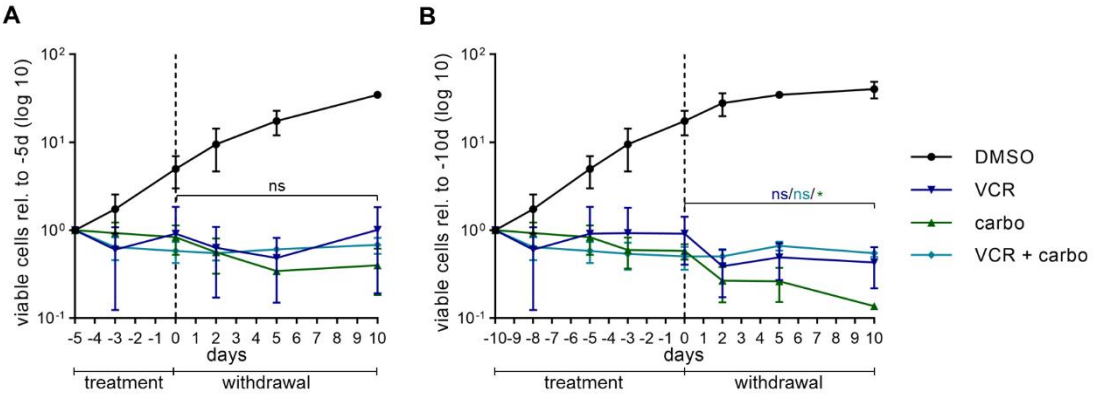

Figure 10 BT-40 viable cell counts during chemotherapy treatment and withdrawal
BT-40 were treated for five (A) or ten (B) days with 0.75 nM vincristine (VCR), 40 µM carboplatin (carbo) or 1 nM VCR and 4 µM carboplatin followed by withdrawal. Dashed line indicates withdrawal timepoint. Viable cell counts are normalized to treatment start (-5d (A) or -10d (B)). Data is shown on a logarithmic scale (base 10) as mean±SD (n=3 independent biological replicates). Unpaired two-sided t-test; * p-value ≤ 0.05; ns: not significant; no indication: not tested
Part (A) of this figure was adapted from Kocher *et al.*, under review

Accordingly, cell regrowth during withdrawal after treatment with 5 nM (but not 10 nM) dabrafenib was significantly increased compared to SOC chemotherapy treatment (Figure 11), thereby mimicking what is observed in patients with tumor rebound. As tumor cell regrowth was only faster than SOC after 5 nM dabrafenib treatment withdrawal and regrowth was most immediate after five days of treatment (Figure 11) this condition was used to further study rebound growth *in vitro*.

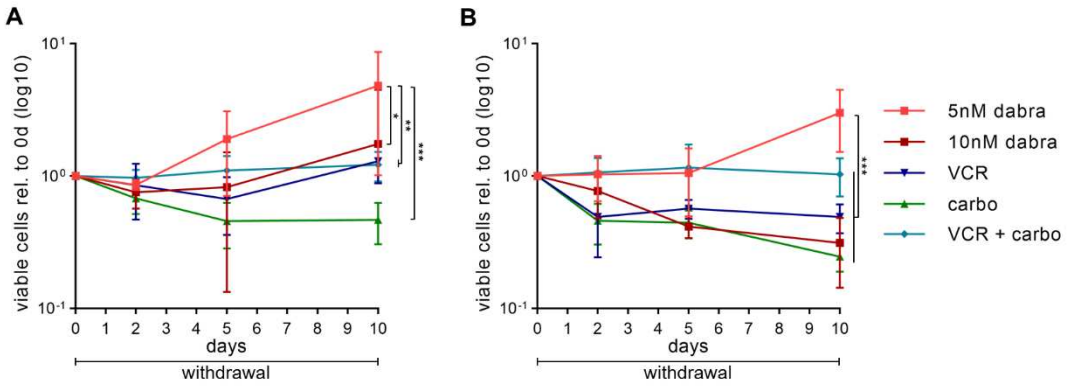

Figure 11 Cell re-growth after treatment withdrawal
Viable cell counts of BT-40 during treatment withdrawal after treatment for five (A) or ten (B) days. Cells were pretreated with dabrafenib (dabra), 0.75 nM vincristine (VCR), 40 µM carboplatin (carbo) or 1 nM VCR and 4 µM carbo; viable cell counts are normalized to the withdrawal timepoint (five (A) or ten (B) days of treatment) for each condition. Data is shown on a logarithmic scale (base 10) as mean±SD (n=3 independent biological). Two-way ANOVA, Bonferroni post-hoc test, * adj-p-value ≤ 0.05 ** adj-p-value ≤ 0.01 *** adj-p-value ≤ 0.001; no indication: not significant
Part (A) of this figure was adapted from Kocher *et al.*, under review

Rebound growth in BT-40 was additionally confirmed using 0.27 nM dabrafenib and 0.03 nM trametinib combination treatment, corresponding to combination metabolic IC50 when combined in the ratio of the unbound C_{max} of each compound (Figure 12A, Table 25), as this treatment was recently FDA-approved for the treatment of *BRAF*^{V600E}-driven pLGGs.[101] In line with effects observed upon dabrafenib treatment and withdrawal, cell proliferation was decreased during treatment and cell regrowth was observed after treatment withdrawal, starting two days after withdrawal (Figure 12B).

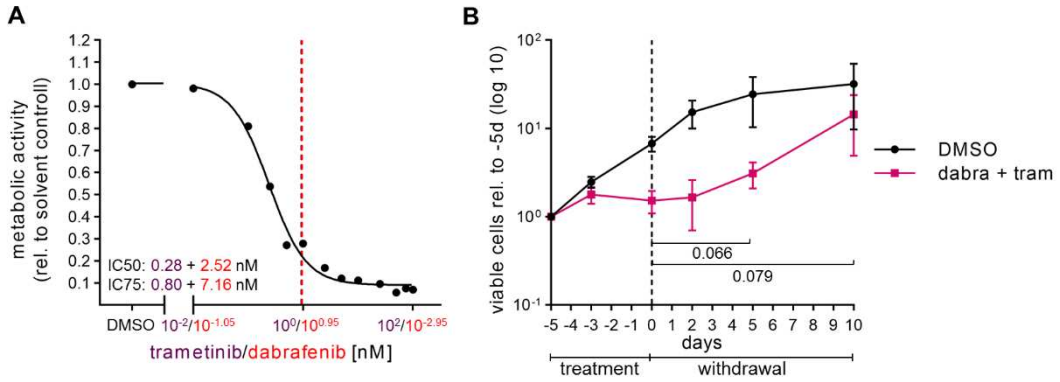

Figure 12 Dabrafenib and trametinib combination treatment and withdrawal in BT-40
(A) Metabolic activity was measured after treatment for 72 h with increasing concentrations of dabrafenib and trametinib combined in a 9:1 ratio. Metabolic activity is depicted relative to solvent control (DMSO) as mean±SD of three independent biological replicates. Dashed line indicates unbound C_{max} concentrations. Absolute inhibitory concentrations (IC)50 and IC75 values were calculated using a 4-parameter dose-response model
(B) Viable cell counts of BT-40 during treatment and withdrawal using 2.7 nM dabrafenib (dabra) and 0.3 nM trametinib (tram). Dashed line indicates withdrawal timepoint. Viable cell counts are normalized to treatment start (-5d). Data is shown on a logarithmic scale (base 10) as mean±SD (n=3 independent biological replicates). Unpaired two-sided t-test; no indication: not tested
This figure was adapted from Kocher *et al.*, under review

Taken together, the BT-40 MAPKi withdrawal rebound model fulfills all criteria of a suitable rebound model and was therefore used to further study rebound growth *in vitro*.

4.1.2 Effects of MAPK inhibition and chemotherapy treatment on cell cycle progression and cell death

After successful rebound model generation, I analyzed the effect of the different treatments on cell cycle progression and apoptosis induction in the BT-40 model. Cell cycle analysis showed a significant increase in the G1/G0 phase during MAPK inhibition (Figure 13A), in line with the role of MAPK signaling in cell cycle progression,[44,45] with no significant increase in PARP cleavage (Figure 13B-C), a marker for programmed cell death.[191] In contrast, chemotherapy treatment induced a significant increase of the sub-G1/G0 population, indicating DNA fragmentation likely due to cell death,[192] as well as an enrichment of the G2/M population in

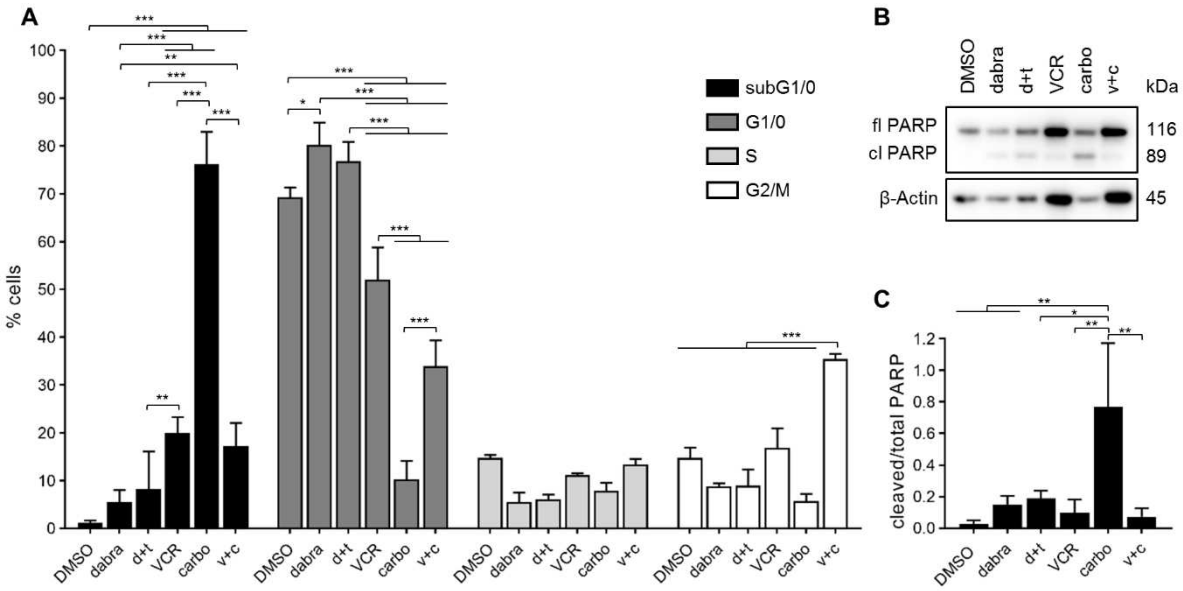

Figure 13 Cell cycle arrest and apoptosis induction
(A) Cell cycle analysis using FACS after treatment for five days with 5 nM dabrafenib (dabra), 2.7 nM dabrafenib and 0.3 nM trametinib (d+t), 0.75 nM vincristine (VCR), 40 µM carboplatin (carbo) or 1 nM vincristine and 4 µM carboplatin (v+c). Percentage of single cell population in the different cell cycle phases are shown as mean±SD (n=3 independent biological replicates). One-way ANOVA, Tukey post-hoc test, * adj-p-value ≤ 0.05 ** adj-p-value ≤ 0.01 *** adj-p-value ≤ 0.01; no indication: not significant
(B-C) Western blot analysis of full-length (fl) and cleaved (cl) PARP after treatment for five days with 5 nM dabrafenib (dabra), 2.7 nM dabrafenib and 0.3 nM trametinib (d+t), 0.75 nM vincristine (VCR), 40 µM carboplatin (carbo) or 1 nM vincristine and 4 µM carboplatin (v+c). Blots shown are representative of three biological replicates (B). Quantification (C) is shown as mean±SD (n=3 independent biological replicates). One-way ANOVA, Tukey post-hoc test, * adj-p-value ≤ 0.05 ** adj-p-value ≤ 0.01; no indication: not significant
This figure was adapted from Kocher *et al.*, under review

case of VCR and carboplatin combination (Figure 13A). PARP cleavage was observed in all chemotherapy treatment conditions, however only significantly increased compared to control in cells treated with 40 µM carboplatin (Figure 13B-C), in line with the strongest increase in the subG1/G0 population.

In summary, these data indicate that MAPKi treatment causes cell cycle arrest with no significant cytotoxic effect, while chemotherapy leads to more cytotoxicity.

4.1.3 Effects of MAPKi withdrawal on MAPK pathway reactivation

Molecular analysis of MAPK pathway activity using WB and qPCR analysis in BT-40 showed near complete pathway inhibition after five days of treatment with 5 nM dabrafenib (Figure 14). This is indicated by decreased phosphorylation of MEK, ERK and FRA1 as well as decreased

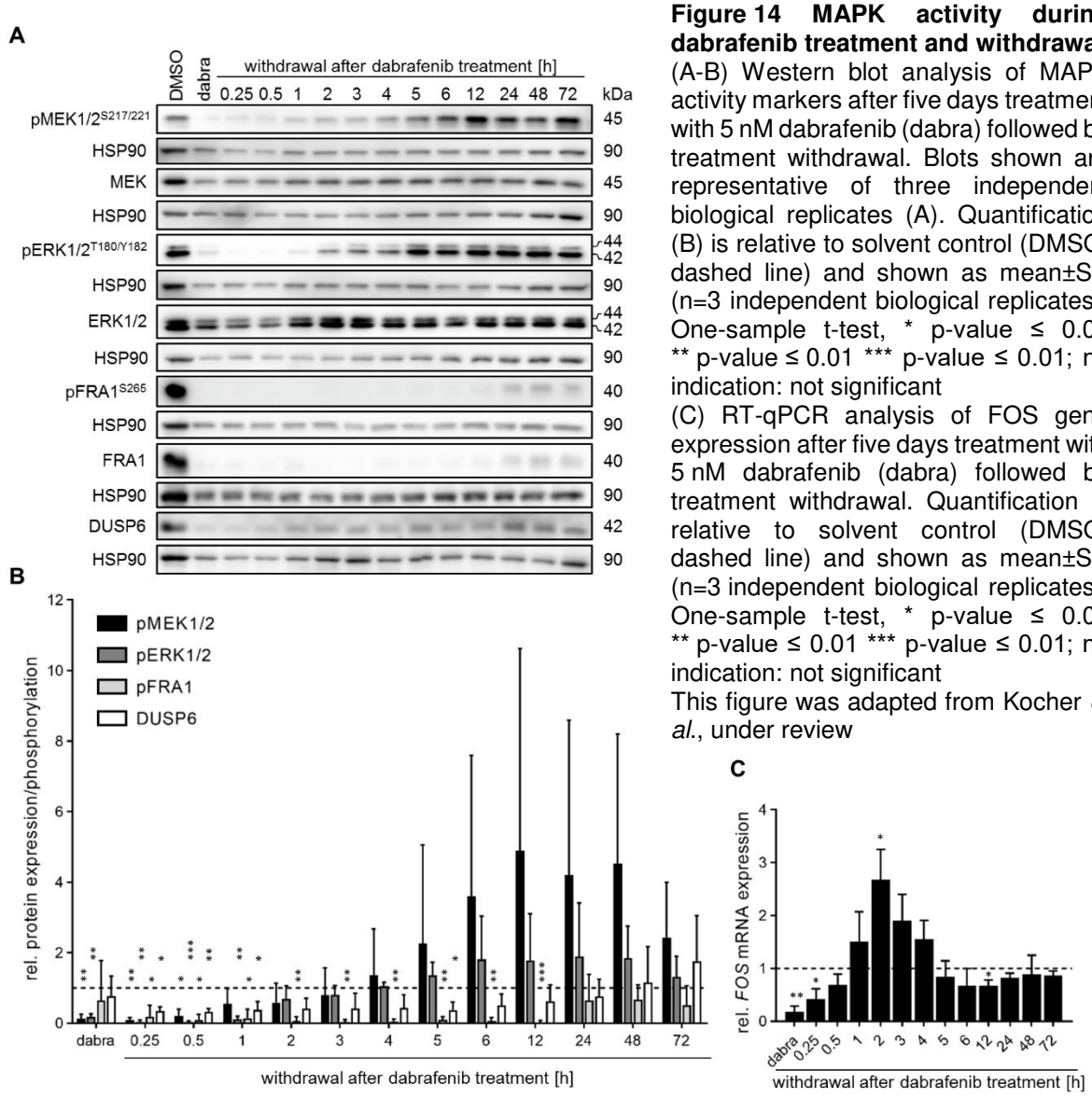

Figure 14 MAPK activity during dabrafenib treatment and withdrawal
(A-B) Western blot analysis of MAPK activity markers after five days treatment with 5 nM dabrafenib (dabra) followed by treatment withdrawal. Blots shown are representative of three independent biological replicates (A). Quantification (B) is relative to solvent control (DMSO; dashed line) and shown as mean±SD (n=3 independent biological replicates). One-sample t-test, * p-value ≤ 0.05 ** p-value ≤ 0.01 *** p-value ≤ 0.01; no indication: not significant
(C) RT-qPCR analysis of FOS gene expression after five days treatment with 5 nM dabrafenib (dabra) followed by treatment withdrawal. Quantification is relative to solvent control (DMSO; dashed line) and shown as mean±SD (n=3 independent biological replicates). One-sample t-test, * p-value ≤ 0.05 ** p-value ≤ 0.01 *** p-value ≤ 0.01; no indication: not significant
This figure was adapted from Kocher *et al.*, under review

FRA1 and DUSP6 protein and *FOS* gene expression (Figure 14). The strong reduction in FRA1 protein expression and phosphorylation in particular indicates sustained MAPK inhibition.[36] Upon dabrafenib withdrawal, pathway reactivation is observed within hours. MEK and ERK phosphorylation reached baseline levels three hours after withdrawal (Figure 14A-B), with MEK phosphorylation showing a trend for a transient increase above control levels (4-fold increase, 6-48 h after withdrawal). Together with the 2.5-fold increased *FOS* gene expression 2 h after withdrawal (Figure 14C), this indicates a possible transient overactivation of the MAPK pathway upon MAPKi withdrawal. Of note, an increased phosphorylation of ERK was not observed, likely due to the parallel re-expression of DUSP6 (Figure 14A-B), a negative regulator of pERK.[193] While MAPK reactivation occurred later (6 h) after dabrafenib and trametinib withdrawal compared to dabrafenib alone, overall reactivation patters are comparable (Figure 15).

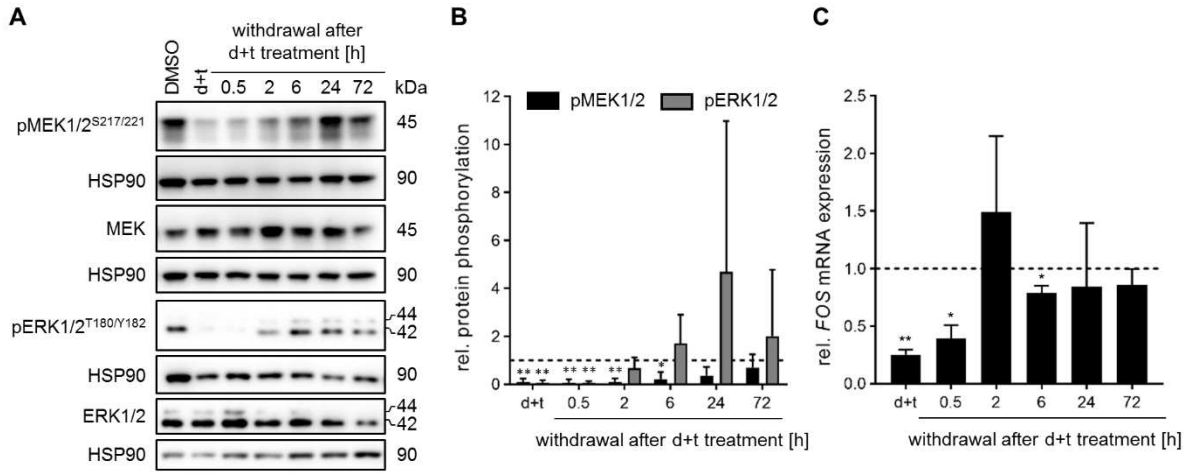

Figure 15 MAPK activity during dabrafenib and trametinib combination treatment and withdrawal
(A-B) Western blot analysis of MAPK activity markers after five days treatment with 0.3 nM trametinib and 2.7 nM dabrafenib (d+t) followed by treatment withdrawal. Blots shown are representative of three independent biological replicates (A). Quantification (B) is relative to solvent control (DMSO; dashed line) and shown as mean±SD (n=3 independent biological replicates). One-sample t-test, * p-value ≤ 0.05 ** p-value ≤ 0.01 *** p-value ≤ 0.01; no indication: not significant
(C) RT-qPCR analysis of *FOS* gene expression after five days treatment with 0.3 nM trametinib and 2.7 nM dabrafenib (d+t) followed by treatment withdrawal. Quantification is relative to solvent control (DMSO; dashed line) and shown as mean±SD (n=3 independent biological replicates). One-sample t-test, * p-value ≤ 0.05 ** p-value ≤ 0.01; no indication: not significant

Importantly, increased MAPK activity was not observed upon DMSO withdrawal (Figure 16), indicating that the observed effects are not induced by the withdrawal procedure. Furthermore, chemotherapy treatment and withdrawal did not induce consistent changes in MAPK activity apart from fluctuations in *FOS* expression during VCR withdrawal (Figure 17). Taken together, this suggests that the rapid MAPK reactivation, associated with a transient increased activity, is a MAPKi withdrawal specific effect, which could possibly be involved in the rebound growth.

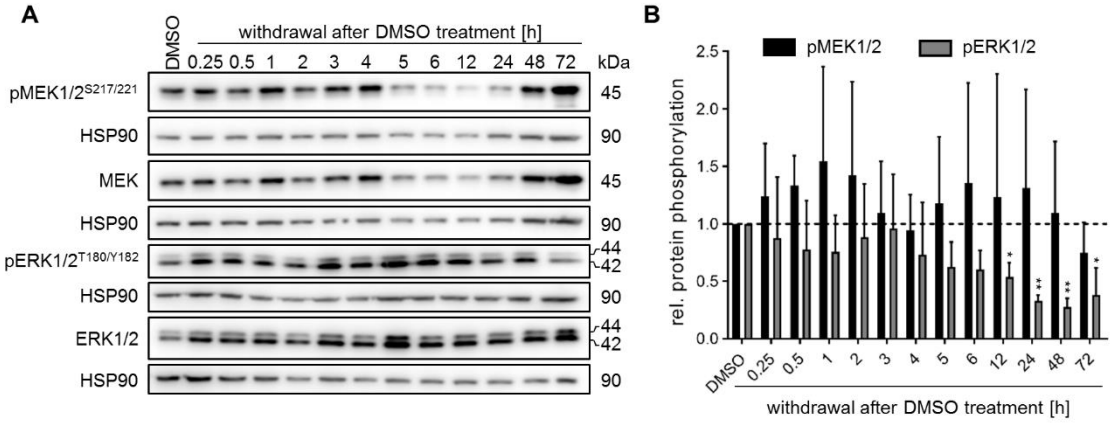

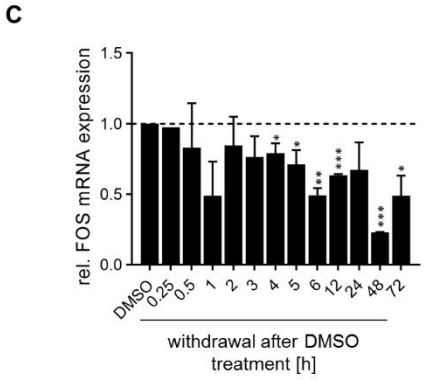

Figure 16 MAPK activity upon DMSO withdrawal
(A-B) Western blot analysis of MAPK activity markers after five days treatment with DMSO followed by withdrawal. Blots shown are representative of three biological replicates (A). Quantification (B) is relative to five days DMSO treatment (dashed line) and shown as mean±SD (n=3 independent biological replicates). One-sample t-test, * p-value ≤ 0.05 ** p-value ≤ 0.01; no indication: not significant
(C) RT-qPCR analysis of FOS gene expression after five days treatment with DMSO followed by withdrawal. Quantification is relative to DMSO treatment (dashed line) and shown as mean±SD (n=3 independent biological replicates). One-sample t-test, * p-value ≤ 0.05 ** p-value ≤ 0.01, *** p-value ≤ 0.001; no indication: not significant
This figure was adapted from Kocher *et al.*, under review

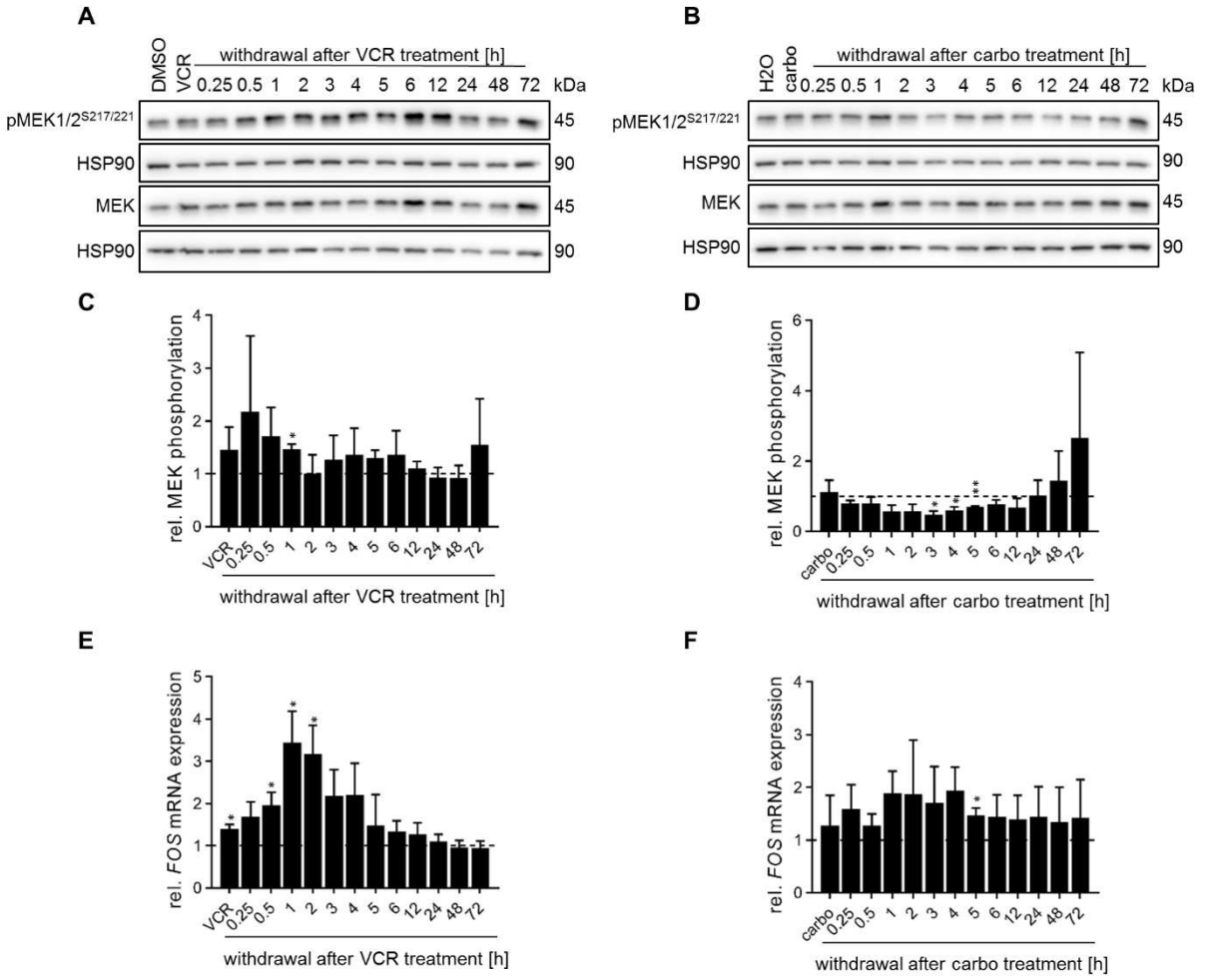

Figure 17 MAPK activity upon SOC chemotherapy treatment and withdrawal
(A-D) Western blot analysis of MEK phosphorylation after five days treatment with 0.75 nM vincristine (VCR) (A, C) or 40 µM carboplatin (carbo) (B, D) followed by withdrawal. Blots shown are representative of three biological replicates (A-B). Quantification (C-D) is relative to solvent control (DMSO or H_2O; dashed line) and shown as mean±SD (n=3 independent biological replicates). One-sample t-test, * p-value ≤ 0.05 ** p-value ≤ 0.01; no indication: not significant
(E-F) RT-qPCR analysis of FOS gene expression after five days treatment with 0.75 nM vincristine (VCR) (E) or 40 µM carboplatin (carbo) (F) followed by withdrawal. Quantification is relative to solvent control (DMSO or H_2O; dashed line) and shown as mean±SD (n=3 independent biological replicates). One-sample t-test, * p-value ≤ 0.05; no indication: not significant
This figure was adapted from Kocher *et al.*, under review

4.2 Multi-omics analysis identifying putative rebound driving mechanisms

Following the initial characterization of the BT-40 rebound model, I aimed at identifying molecular mechanisms driving rebound growth by generating a multi-omics dataset covering key dabrafenib withdrawal timepoints using RNA sequencing (RNAseq), LC-MS/MS based proteomics and phospho-proteomics. Timepoints for multi-omics analysis (Figure 18) were

identified based on the data described in “4.1 *In vitro* rebound modelling” and included five days treatment with 5 nM dabrafenib followed by:

1) 0.5 h withdrawal, to observe immediate changes in the phospho-proteome, not influenced by changes in gene/protein expression during withdrawal
2) 2 h withdrawal, where increased *FOS* expression was observed, to investigate early changes in gene expression
3) 6 h withdrawal, which correlates with increased MEK phosphorylation, to investigate putative other increasingly activated signaling pathways
4) 24 h withdrawal, to observe possible consequences of increased *FOS* expression and MEK phosphorylation. Additionally, cell regrowth started at 48 h of withdrawal, suggesting putative rebound driving mechanisms should latest be active 24 h after withdrawal.
5) 72 h withdrawal, when all MAPK activation markers have reached baseline expression and cells are normally proliferating

Time-matched DMSO treatment and withdrawal samples were used to control for possible effects induced by the withdrawal procedure.

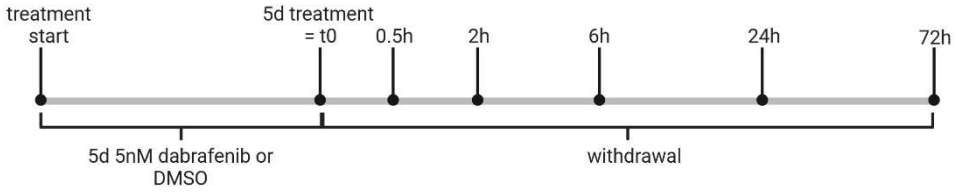

Figure 18 Multi-omics sample generation timeline
created using BioRender.com

4.2.1 Controlling for possible batch effects in multi-omics data

After omics data generation, each dataset was inspected for possible batch effects induced e.g. by sample generation at different timepoints and different BT-40 batches (i.e., biological replicates) or order of sample processing/analysis (in case of LC-MS/MS analysis).

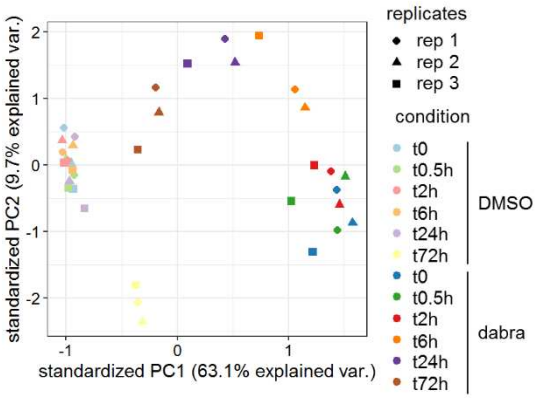

Figure 19 Principal component analysis of RNAseq samples
Principle component (PC) analysis of RNAseq samples harvested after five days treatment (=t0) with DMSO (solvent control) or 5 nM dabrafenib (dabra) followed by withdrawal (t0.5h-t72h).

Principal component analysis (PCA) of RNAseq data showed clustering of samples based on condition (treatment vs. control) and timepoint after dabrafenib withdrawal (Figure 19). Different biological replicates for each condition and timepoint did not cluster apart, indicating the absence of a batch effect induced by sample generation (Figure 19). Furthermore, control samples clustered together across withdrawal timepoints apart from samples harvested 72 h after DMSO withdrawal (Figure 19), providing a first hint that the withdrawal procedure did not influence gene expression at early timepoints (up to 24 h).

Proteomics analysis yielded approx. 6000 proteins in each sample and no increasing or decreasing patterns were observed over the course of the LC-MS/MS run (Figure 20A). Furthermore, PCA showed no obvious clustering of biological replicates but rather clustering of samples based on condition and dabrafenib withdrawal time (Figure 20B). This pattern is similar to the clustering observed in the RNAseq dataset (Figure 19), although with a less distinct clustering likely due to the lower variance explained by PC1 and PC2 in the proteomics

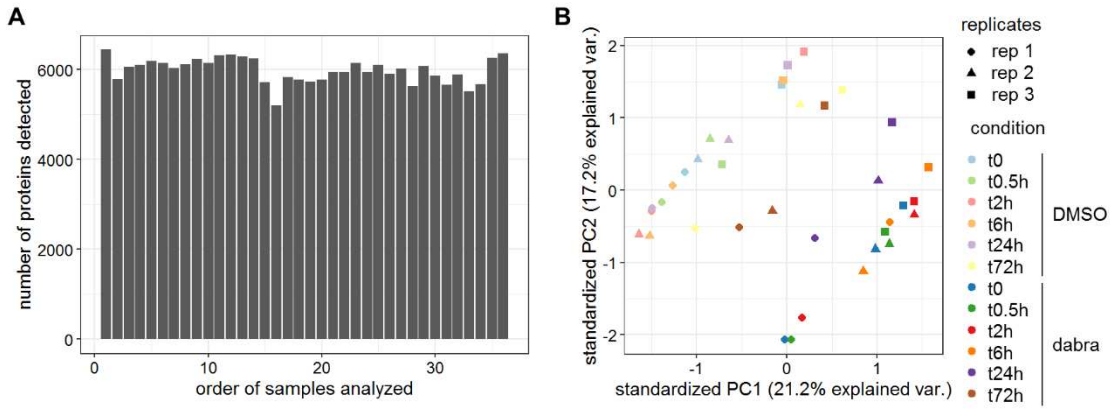

Figure 20 Quality check of LC-MS/MS proteomics analysis data
(A) Number of proteins detected in each sample before any filtering or clean-up steps were performed. Samples are depicted in the order they were subjected to LC-MS/MS analysis.
(B) Principal component (PC) analysis of LC-MS/MS proteomics samples harvested after five days treatment (=t0) with DMSO (solvent control) or 5 nM dabrafenib (dabra) followed by withdrawal (t0.5h-t72h).

dataset (Figure 20B). Taken together, no indications of a batch effect were observed in the proteomics data.

In contrast to the proteomics dataset, the phospho-proteomics dataset showed high variation in peptide-count across samples, spanning from ~3300 to ~25000 (Figure 21A). Considering the order in which the samples were subjected to the MS/MS analysis, it became evident that in the first 19 samples, a lower number of peptides was detected (approx. 5000 peptides), compared to the later samples (approx. 17000 peptides). While the variance explained by PC1 and PC2 in the PCA was < 20 %, to some extent a clustering based on the sample analysis order can be observed (Figure 21B). As samples were subjected to LC-MS/MS analysis in a random order, this batch effect is likely induced by the MS/MS analysis order. To reduce this

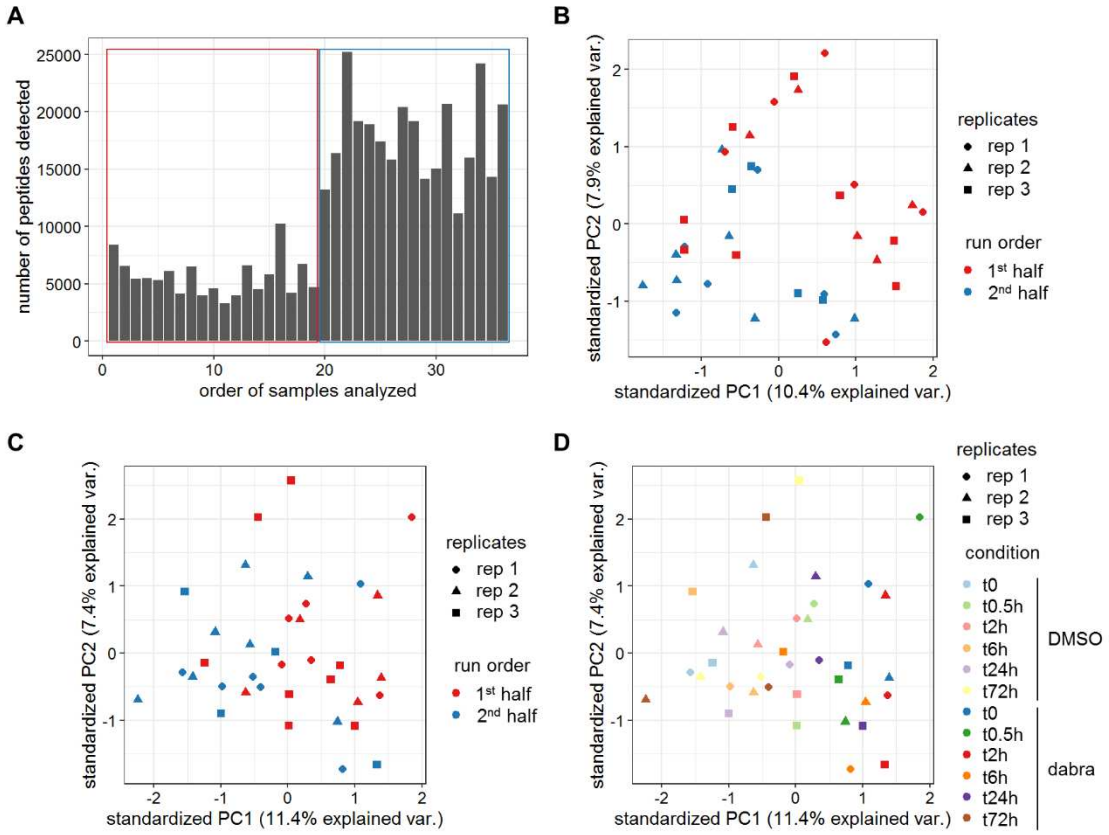

Figure 21 Quality check of LC-MS/MS phospho-proteomics analysis data
(A) Number of peptides detected in each sample before any filtering or clean-up steps were performed. Samples are depicted in the order they were subjected to LC-MS/MS analysis.
(B-D) Principal component (PC) analysis of LC-MS/MS proteomics samples harvested after five days treatment (=t0) with DMSO (solvent control) or 5 nM dabrafenib (dabra) followed by withdrawal (t0.5h-t72h). (B) PCA before batch-correction was performed. (C-D) PCA after batch-correction was performed. Data in both panels is the same, however different groups (run order or condition) are indicated by colors.

effect, batch correction was performed using the Removing Unwanted Variation-III method[168] based on a set of stably phosphorylated sites.[166,167] As shown by PCA, batch correction did reduce the variation induced by the LC-MS/MS analysis order (Figure 21C). Clustering of samples based on condition (treatment vs. control) was observed in the batch-corrected phospho-proteomics dataset (Figure 21D), although clusters are not as distinct as for the RNAseq (Figure 19) and proteomics datasets (Figure 20B), likely due to the low variance explained by PC1 and PC2 in the phosphoproteomics dataset (Figure 21D). Clustering based on time of dabrafenib withdrawal is not evident in the PCA of the phospho-proteomic dataset, possibly due to the high variation in the dataset as PC1 and PC2 explain < 20% of the variance (Figure 21D).

In summary, no indications of batch effects were observed in the RNAseq and proteomics data. The batch effect observed in the phosphoproteomics data could be corrected. Overall, all three omics layers showed clustering of samples based on condition (treatment vs. control) and furthermore based on dabrafenib withdrawal time in case of the RNAseq and proteomics datasets.

4.2.2 Investigation of possible effects induced by the withdrawal procedure

As mentioned previously, time-matched DMSO withdrawal controls were included to control for possible effects induced by the withdrawal procedure. At early withdrawal timepoints (up to 24 h) DMSO controls showed no significant changes in gene expression and protein phosphorylation and only few significant changes in protein expression (Figure 22A). Only at 72 h of withdrawal an increased number of significant changes in gene and protein expression, but not phosphorylation, were observed. However, these changes were likely not induced by the withdrawal procedure but are due to contact inhibition, as indicated by depletion of cell-cycle related gene signatures and decreased proliferation starting after 24 h of withdrawal (Figure 22B-C).

Taken together, this indicates no effect of the withdrawal procedure on differential gene expression, protein expression or phosphorylation. Therefore, in the following analysis, five days DMSO was used as a reference.

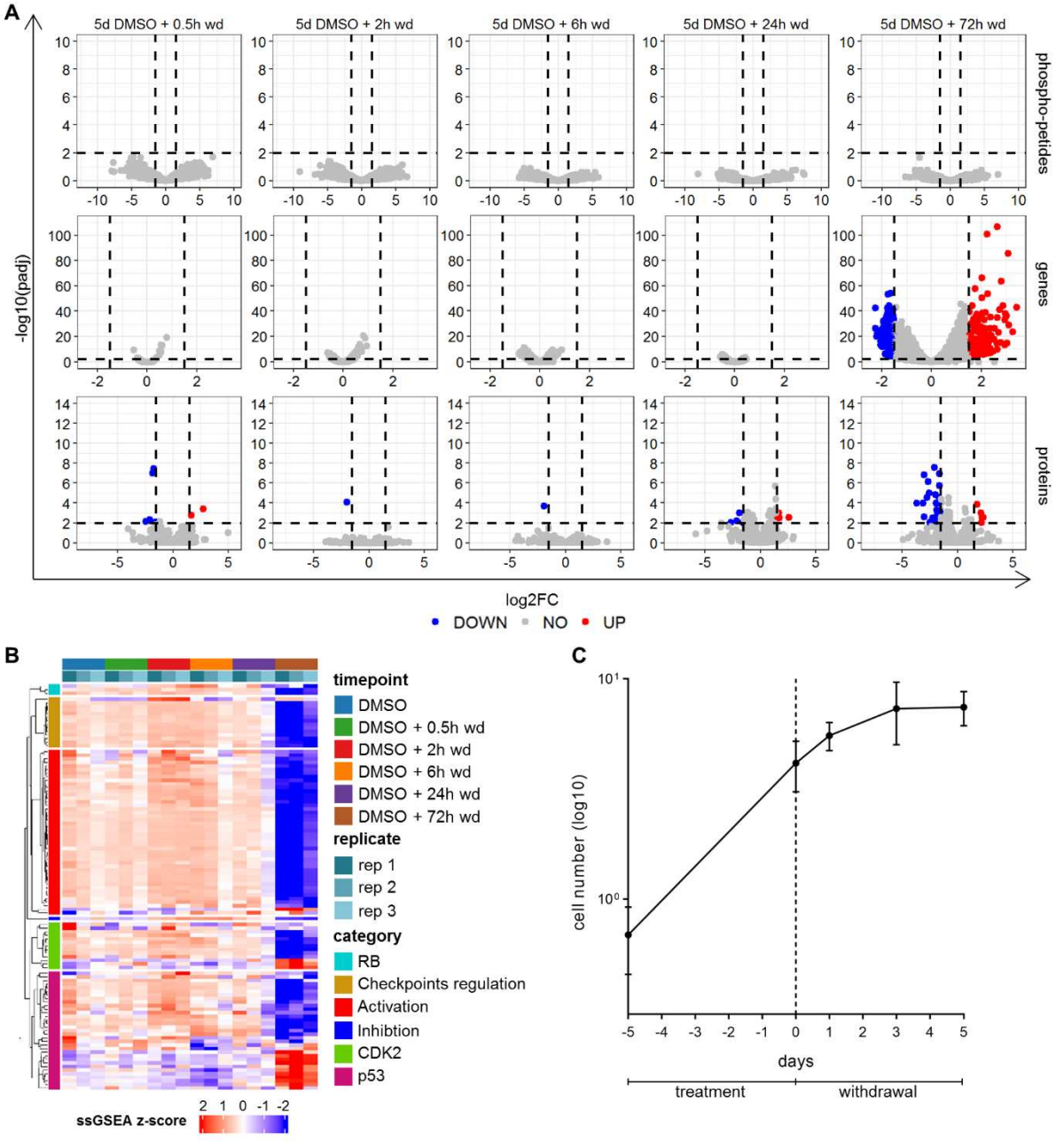

Figure 22 Multi-omics analysis of differential regulation upon DMSO treatment and withdrawal
(A) Volcano plots showing differentially regulated phospho-peptides, genes and proteins during withdrawal (wd) after treatment with DMSO for five days. log2FCs are calculated relative to five days DMSO treatment. Horizontal dashed line indicates significance cut-off of adj-p-value < 0.01. Vertical dashed lines indicate log2FC cut-off -/+ 1.5. n=3 independent biological replicates
(B) Heatmap showing ssGSEA z-scores for cell cycle related gene signatures taken from the MSigDB C2 subcollection CP (canonical pathways) in RNAseq samples harvested during withdrawal (wd) after treatment with DMSO for five days.
(C) Viable cell counts during treatment and withdrawal using DMSO for the seeding density used to generate the samples for multi-omics analysis. Dashed line indicates the timepoint of withdrawal. Data is shown on a logarithmic scale (base 10) as mean±SD (n=3 independent biological replicates)

4.2.3 Investigation of differentially regulated mechanisms

Decreased MAPK activity was observed using omics specific activity signatures in all three layers, confirming on-target activity of dabrafenib treatment (Figure 23). Furthermore, in line with aforementioned data, reactivation of the MAPK pathway was observed within hours to one day (protein phosphorylation: 2 h; gene expression: 6 h; protein expression: 24 h) and associated with a transient overactivation on the level of gene expression and protein phosphorylation (Figure 23). Taken together, this further validates the rapid MAPK reactivation and transient overactivation observed upon MAPKi withdrawal.

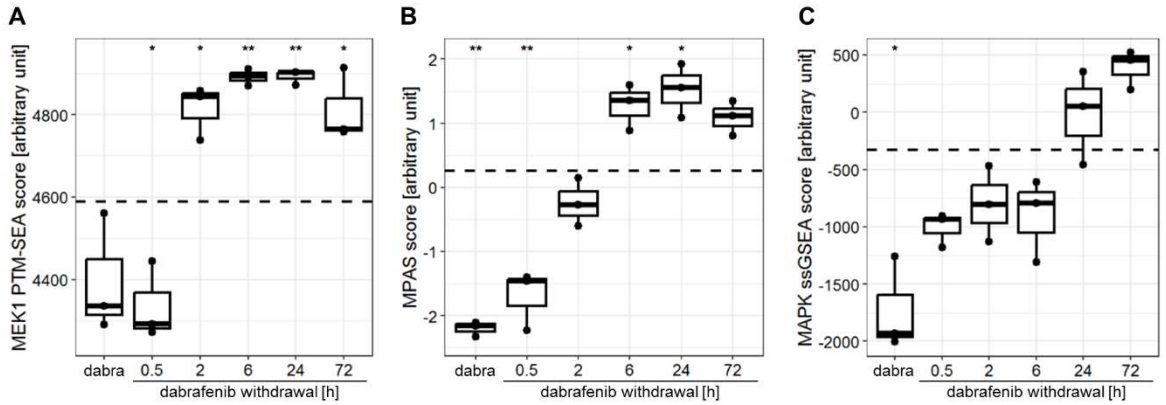

Figure 23 MAPK activity measured using omics specific signatures
MAPK pathway activity scores after five days treatment with 5 nM dabrafenib (dabra) followed by withdrawal measured using the MEK1 PTM-SEA score for phospho-proteomics data (A), the MPAS score for RNAseq data (B) and a proteomics-based MAPK ssGSEA-score for proteomics data (C). Boxplots depict the median, first and third quartiles. Whiskers extend from the hinge to the largest/smallest value no further than 1.5 * IQR from the hinge (where IQR is the interquartile range). Dashed line indicates the mean of the solvent control (five days DMSO). Two-tailed unpaired t-test, * p-value ≤ 0.05 ** p-value ≤ 0.01; no indication: not significant (n=3 independent biological replicates) This figure was adapted from Kocher *et al.*, under review

Conversely, longitudinal k-means (kml) clustering of differentially regulated genes, proteins and phospho-peptides showed no major cluster of transiently up- or downregulated genes, proteins or phospho-peptides during dabrafenib withdrawal (Figure 24), indicating that the main differential regulation was induced during dabrafenib treatment. This differential regulation was maintained for at least 24 h of withdrawal (mean of highest differentially regulated clusters ≥ 1.5 or ≤ -1.5; Figure 24).

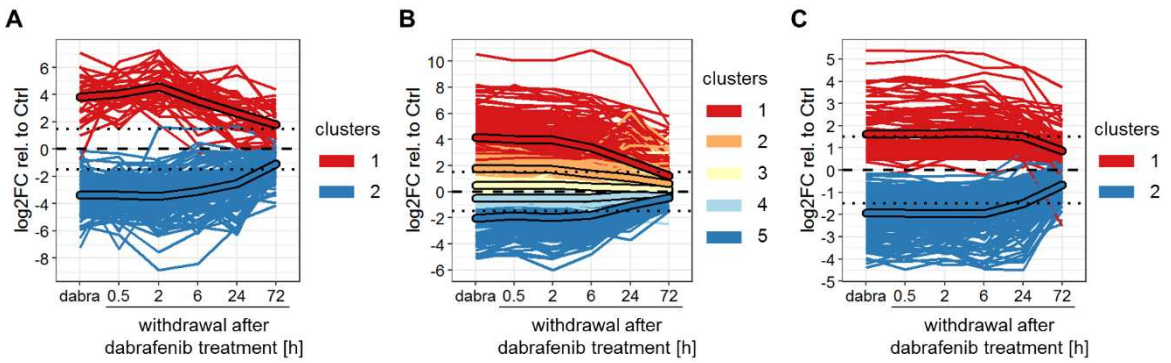

Figure 24 Longitudinal k-means clustering
Longitudinal k-means clustering of differentially regulated phospho-peptides (A), genes (B), proteins (C) and after five days treatment with 5 nM dabrafenib (dabra) followed by withdrawal relative to solvent control (five days DMSO; dashed line). Only genes, proteins and phospho-peptides with an adjusted p-value < 0.01 for at least one timepoint were included in the analysis. Unframed lines represent single genes, proteins or phospho-peptides, framed lines show cluster means. Dotted line: log2FC = +/-1.5 (n=3 independent biological replicates)
This figure was adapted from Kocher *et al.*, under review

GO-term enrichment analysis showed significant enrichment of terms related to cytokine signaling and TGF-beta signaling within the upregulated genes (kml-clusters 1 and 2, Figure 24B) and proteins (kml-cluster 1, Figure 24C) respectively (Figure 25A-B, Supplementary Table 1-2). Enrichment of cytokine-related GO-terms was additionally associated with the increased gene expression of 21 cytokines, indicated by a log2FC > 2 (adj. p-value < 0.01) at 6 h of dabrafenib withdrawal (Supplementary Figure 1). At this timepoint, cytokines possibly involved in rebound growth should be transcribed in order to be translated and secreted to induce rebound growth starting 48 h after withdrawal. Increased TGF-beta signaling, indicated by the GO-term enrichment analysis, was further predicted by kinase-substrate enrichment analysis (KSEA) of significantly regulated phospho-peptides (adj. p-value < 0.01 at a given time-point; Figure 25E). Additionally, KSEA analysis suggested increased AKT activity as well as increased activity of JAK/STAT downstream effectors PIM and PAK upon dabrafenib treatment and early withdrawal (up to 6 h; Figure 25E). Furthermore, ssGSEA analysis of RNAseq data showed enrichment of signatures related to RTKs and MAPK upstream activators upon dabrafenib treatment but in particular during withdrawal (Supplementary Figure 2). Activity of either, which is regulated by phosphorylation, was not further indicated by the phospho-proteomics dataset (Figure 25E).

In contrast, GO-terms enriched within the downregulated genes (kml-clusters 4 and 5, Figure 25B) and proteins (kml-cluster 2, Figure 24C) were related to DNA replication and cell-cycle activity (Figure 25C-D, Supplementary Table 3-4). Accordingly, significantly decreased

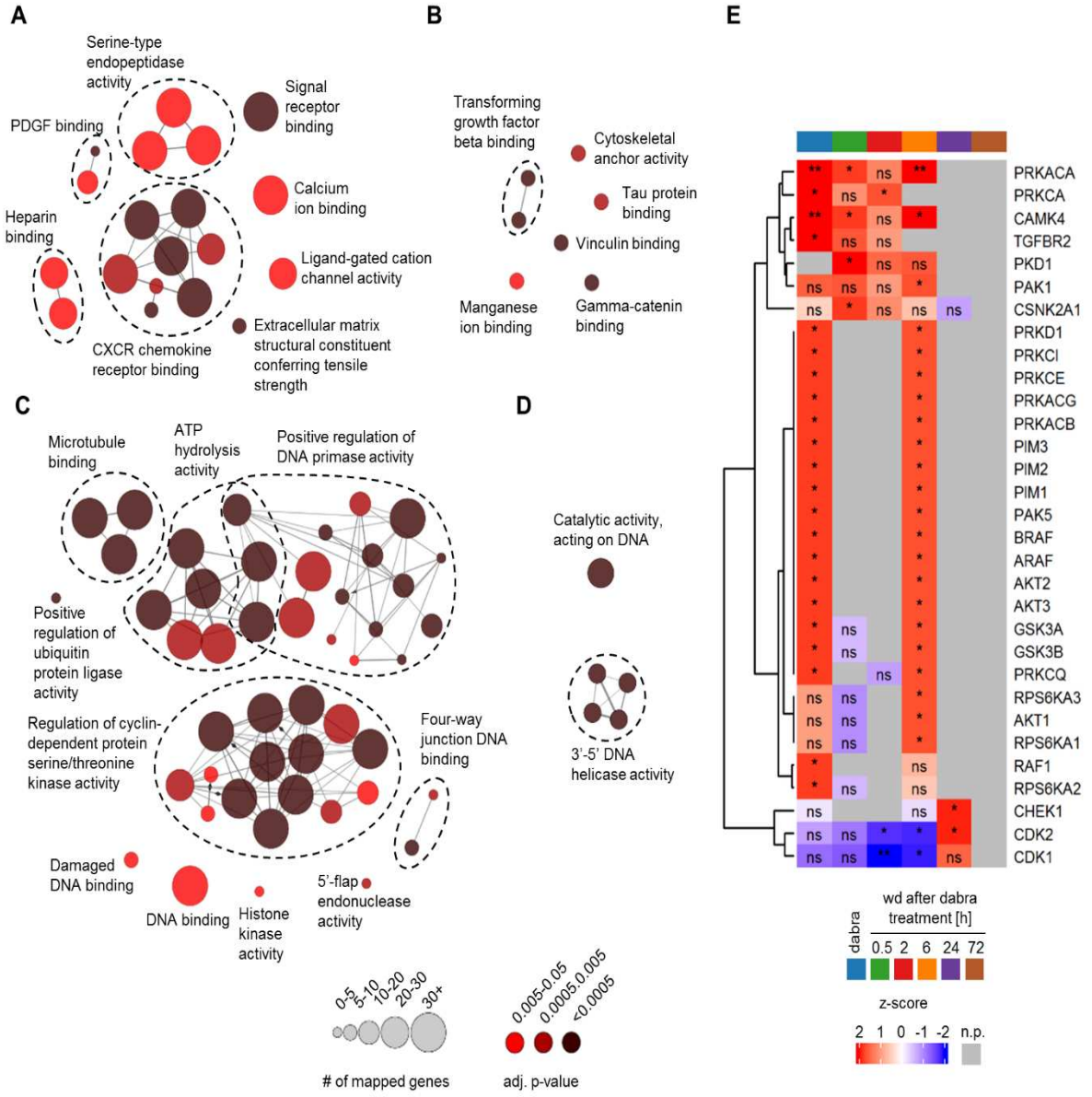

Figure 25 Multi-omics analysis of mechanisms differentially regulated upon dabrafenib treatment and withdrawal

(A-D) GO-term enrichment analysis of upregulated genes (clusters 1 and 2 from Figure 24B) (A), and proteins (cluster 1 from Figure 24C) (B) or downregulated genes (clusters 4 and 5 from Figure 24B) (C), and proteins (cluster 1 from Figure 24C) (D). Only terms with significant enrichment (adj-p-value ≤ 0.05; Bonferroni step-down correction) are shown. GO-term groups are defined by overlapping genes and named based on the GO-Term with highest percentage of mapped genes

(E) Kinase-substrate-enrichment-analysis (KSEA) of differentially regulated phospho-peptides relative to solvent control after five days treatment with 5 nM dabrafenib (dabra) followed by withdrawal (wd). Only phospho-peptides with a significant regulation (adj-p-value < 0.01 at a given timepoint) were included in the analysis. * adj-p-value ≤ 0.05 ** adj-p-value ≤ 0.01; ns: not significant; n.p.= no prediction (n=3 independent biological replicates)

This figure was adapted from Kocher *et al.*, under review

CDK activity up to 6 h of withdrawal was predicted by KSEA analysis of significantly regulated phospho-peptides (Figure 25E). Overall, this data is in line with cell cycle arrest during MAPKi treatment (Figure 13) and decreased proliferation until two days of withdrawal (Figure 8A).

To summarize, the data above suggests MAPKi induced upregulation of cytokines and the activation of several signaling pathways (AKT, TGF-beta and JAK/STAT) as possible mechanisms involved in rebound growth. Upon treatment withdrawal, reactivation and transient overactivation of the MAPK pathway and reactivation of cell cycle related pathways was observed, while MAPKi induced changes were still maintained during early withdrawal (up to 24 h).

4.2.4 Validation of differentially regulated mechanisms

Table 26 AUC-log2FCs of cytokine secretion during dabrafenib withdrawal
log2FC = log2($AUC_{dabrafenib\ wd}$ +1) - log2($AUC_{DMSO\ wd}$+1)
AUC = area under the curve,
wd = withdrawal
This table was adapted from Kocher *et al.*, under review

Cytokine	AUC log2FC
CCL11	5.52
CX3CL1	3.80
CCL2	3.68
CCL7	2.38
IL1b	2.15
CCL17	1.81
LIF	1.51
CXCL10	1.14
CXCL2	1.10
TNF	1.08
CXCL5	1.00
CXCL6	0.83
IL8	0.59
CXCL1	0.47
IL9	-1.08
IL1a	-2.59

To validate mechanisms shown to be upregulated upon dabrafenib treatment and maintained during withdrawal in the multi-omics dataset, I first investigated the secretion of cytokines upregulated during treatment and withdrawal using a commercially available Luminex-based multiplex assay (covering 16 of the 21 upregulated cytokines (mRNA)). Upon dabrafenib treatment, several cytokines showed increased secretion compared to control, which was maintained during withdrawal (Supplementary Figure 3). Furthermore, during dabrafenib withdrawal, 11/16 cytokines showed a > 2-fold increased secretion compared to DMSO withdrawal (AUC-log2FC > 1; Table 26). Of these eleven cytokines, secretion of CCL2, CX3CL1, CXCL10 and CCL7 was significantly increased upon dabrafenib withdrawal compared to DMSO 24 h after withdrawal

(Figure 26), which is one day before cells start to proliferate again (Figure 8A). Increased mRNA expression of *CCL2, CX3CL1, CXCL10* and *CCL7* was confirmed using RT-qPCR also upon dabrafenib and trametinib combination treatment and withdrawal (Figure 27).

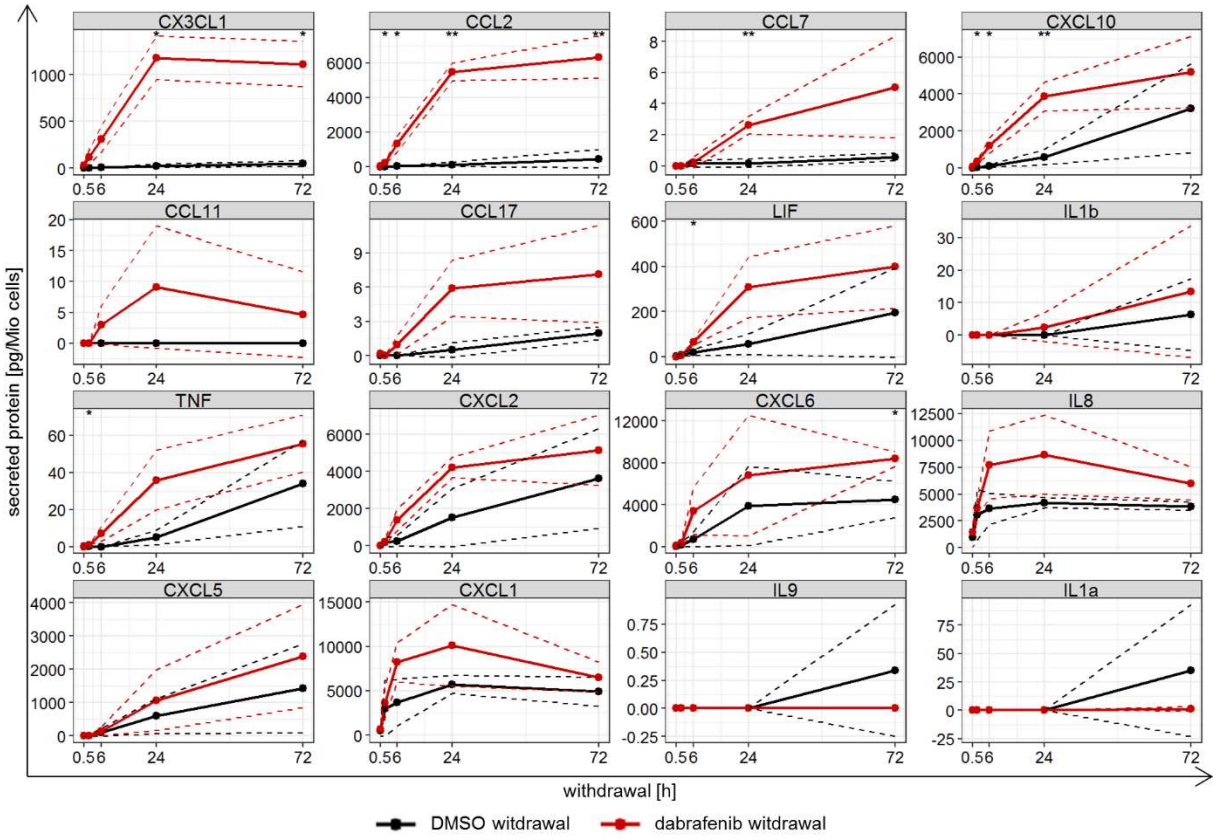

Figure 26 Cytokine secretion during dabrafenib withdrawal in BT-40
Luminex-based multiplex assay showing secretion during withdrawal after treatment for five days with either DMSO (solvent control) or 5 nM dabrafenib. Data for 24 h dabrafenib withdrawal is the same as shown in Supplementary Figure 3. Data is shown as mean±SD (n=3 independent biological replicates). Two-tailed unpaired t-test, * p-value ≤ 0.05 ** p-value ≤ 0.01; not indicated: not significant
This figure was adapted from Kocher *et al.*, under review

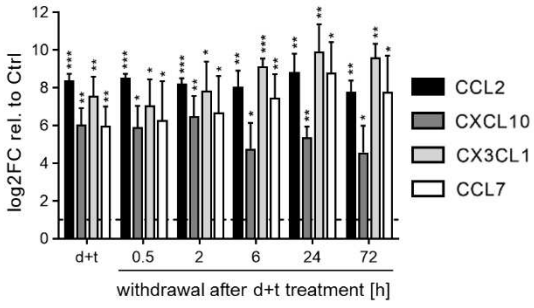

Figure 27 Cytokine expression during dabrafenib and trametinib combination treatment and withdrawal
RT-qPCR analysis of cytokine gene expression after five days treatment with 2.7 nM dabrafenib and 0.3 nM trametinib (d+t) followed by treatment withdrawal. Quantification is relative to solvent control (DMSO; dashed line) and shown as mean±SD (n=3 independent biological replicates). *CCL7* was undetected in solvent control samples, for these samples Ct values were set to 40 (max. number of cycles). One-sample t-test, p-value ≤ 0.05 ** p-value ≤ 0.01 *** p-value ≤ 0.01; no indication: not significant
This figure was adapted from Kocher *et al.*, under review

In addition to validating increased cytokine expression and secretion, a kinase phosphorylation array and WB analysis were performed to validate increased activation of signaling pathways suggested by the multi-omics data. Increased AKT activation, indicated by increased GSK3a/b phosphorylation, was confirmed by the kinase array (Figure 28A). Furthermore, this was confirmed by WB analysis showing increased AKT phosphorylation upon treatment, which was maintained until 6 h after dabrafenib withdrawal (Figure 28B-C). Changes in NF-kB activity, involved in the expression of different cytokines[194,195] and a possible down-stream mediator of the AKT pathway,[195,196] was not observed (Supplementary Figure 4). Of note, AKT activity was also increased upon dabrafenib and trametinib combination treatment and maintain until 24 h of withdrawal (Figure 28D-E).

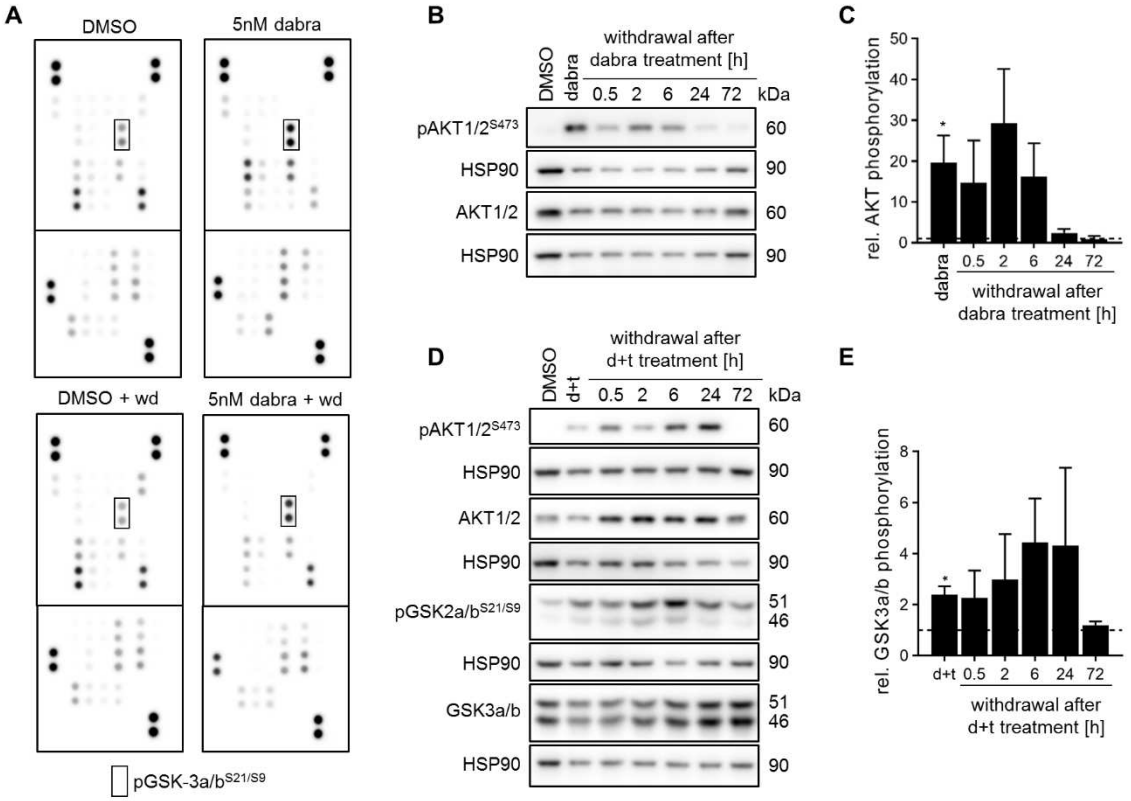

Figure 28 Increased AKT activity during MAPKi treatment and withdrawal
(A) Kinase phosphorylation array of samples treated for five days with 5 nM dabrafenib (dabra) or DMSO (solvent control) followed by 24 h withdrawal (wd). Arrays consist of two membranes, each target is detected in technical duplicates. Images shown are representatives of two biological replicates.
(B-E) Western blot analysis of AKT activity markers after five days treatment with 5 nM dabrafenib (dabra) (B-C) or 0.3 nM trametinib and 2.7nM dabrafenib (d+t) (D-E) followed by withdrawal. Blots shown are representative of three independent biological replicates (B, D). Quantification (C, E) is relative to solvent control (DMSO; dashed line) and shown as mean±SD (n=3 independent biological replicates). One-sample t-test, * p-value ≤ 0.05; no indication: not significant
This figure was adapted from Kocher *et al.*, under review

In contrast, the kinase array and WB analysis did not indicate increased JAK/STAT or canonical TGF-beta signaling respectively (Supplementary Figure 5).

Taken together, these data suggest increased AKT signaling and increased CX3CL1, CCL2, CXCL10 and CCL7 expression and secretion, induced upon MAPKi and maintained during withdrawal, which may be possible mechanisms involved in rebound growth.

4.3 Investigation of putative tumor cell intrinsic rebound driving mechanisms

Increased AKT signaling is known to have tumor promoting effects,[197–202] suggesting a possible rebound driving effect of increased AKT signaling induced by MAPKi treatment. Furthermore, CCL2, CX3CL1, CXCL10 and CCL7 have been shown to be tumor promoting through direct effects on tumor cells.[140,141,146,159,160] As some receptors for these cytokines[203] are expressed in BT-40 (Supplementary Figure 6), increased secretion of these cytokines is another possible tumor cell intrinsic rebound driving mechanism.

4.3.1 Investigation of a possible connection between upregulated AKT activity and cytokine expression upon dabrafenib treatment and early withdrawal

As AKT signaling has been shown to both induce cytokine expression[204,205] or be activated by cytokines,[206–208] I first investigated whether AKT signaling and cytokine expression are connected in the BT-40 rebound model. Inhibition of CCL2, CXCL10, CX3CL1 and CCL7, individually or combined, during dabrafenib withdrawal using neutralizing antibodies (neuABs) did not decrease GSK3a/b phosphorylation (Figure 29A-B). In line with this, stimulation of untreated BT-40 with recombinant cytokines did not induce increased AKT or GSK3a/b phosphorylation (Figure 29C-D). Furthermore, inhibition of AKT signaling using the PI3K inhibitor alpelisib, despite showing on-target activity (Supplementary Figure 7A-B), did not reduce cytokine gene expression induced by dabrafenib treatment (Figure 29E).

Taken together, these results indicate the independence of increased cytokine expression and AKT signaling induced by MAPKi treatment in the BT-40 model.

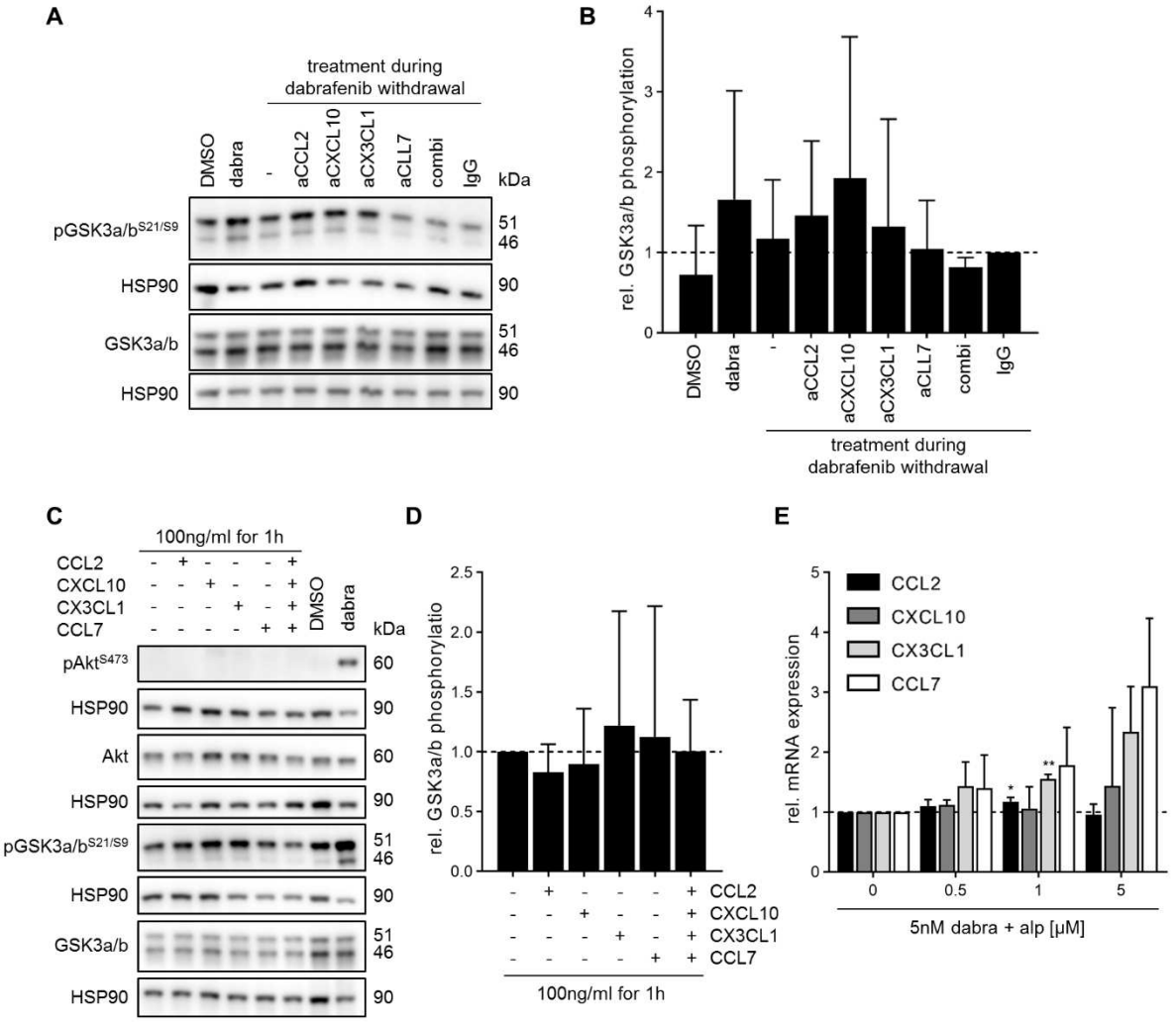

Figure 29 Cytokine expression and increased AKT activity are non-related mechanisms
(A-B) Western blot analysis of GSK3a/b phosphorylation after five days treatment with 5 nM dabrafenib (dabra) followed by 24 h of withdrawal (-) or treatment with antibodies neutralizing CCL2 (aCCL2, 0.5 µg/mL), CX3CL1 (aCX3CL1, 0.25 µg/mL), CXCL10 (aCXCL10, 0.25 µg/mL) and CCL7 (aCCL7, 0.1 ng/mL) individually or as combination (combi). Blots shown are representative of three independent biological replicates (A). Quantification (B) is relative to IgG control (IgG, 1 µg/mL). One-sample t-test; no indication: not significant
(C-D) Western blot analysis of AKT activity markers after stimulation with recombinant cytokines. Treatment for five days with DMSO or 5 nM dabrafenib (dabra) served as negative and positive control for western blots (C). Blots shown are representative of three biological replicates (C). Quantification
(D) was done relative to untreated samples (dashed line) and is shown as mean±SD (n=3 independent biological replicates). One-sample t-test; no indication: not significant
(E) RT-qPCR analysis of cytokine gene expression after five days treatment with 5 nM dabrafenib (dabra) alone or in combination with increasing concentrations of alpelisib (alp). Quantification was done relative to dabrafenib only treatment (0; dashed line) and is shown as mean±SD (n=3 independent biological replicates). One-sample t-test, * p-value ≤ 0.05 ** p-value ≤ 0.01; no indication: not significant
This figure was adapted from Kocher *et al.*, under review

4.3.2 Effect of increased AKT activity during MAPKi treatment and withdrawal

AKT signaling can have growth promoting effects and upregulation of PI3K/AKT/mTOR signaling during MAPKi treatment is a possible mechanism leading to MAPKi resistance in other tumor entities.[200,209–214] Therefore, the effect of AKT signaling on rebound growth in BT-40 was investigated using the PI3K inhibitor alpelisib or the AKT inhibitor ipatasertib, at concentrations showing on-target effect (Supplementary Figure 7) and within C_{max} concentrations[188,215] (Table 27). PI3K or AKT inhibition in combination with MAPKi treatment did not affect viable cell counts during treatment compared to MAPKi only and furthermore, did not influence rebound growth after treatment withdrawal (Figure 30A-B). Additionally, PI3K or AKT inhibition upon MAPKi withdrawal did not affect tumor cell regrowth either (Figure 30C-D).

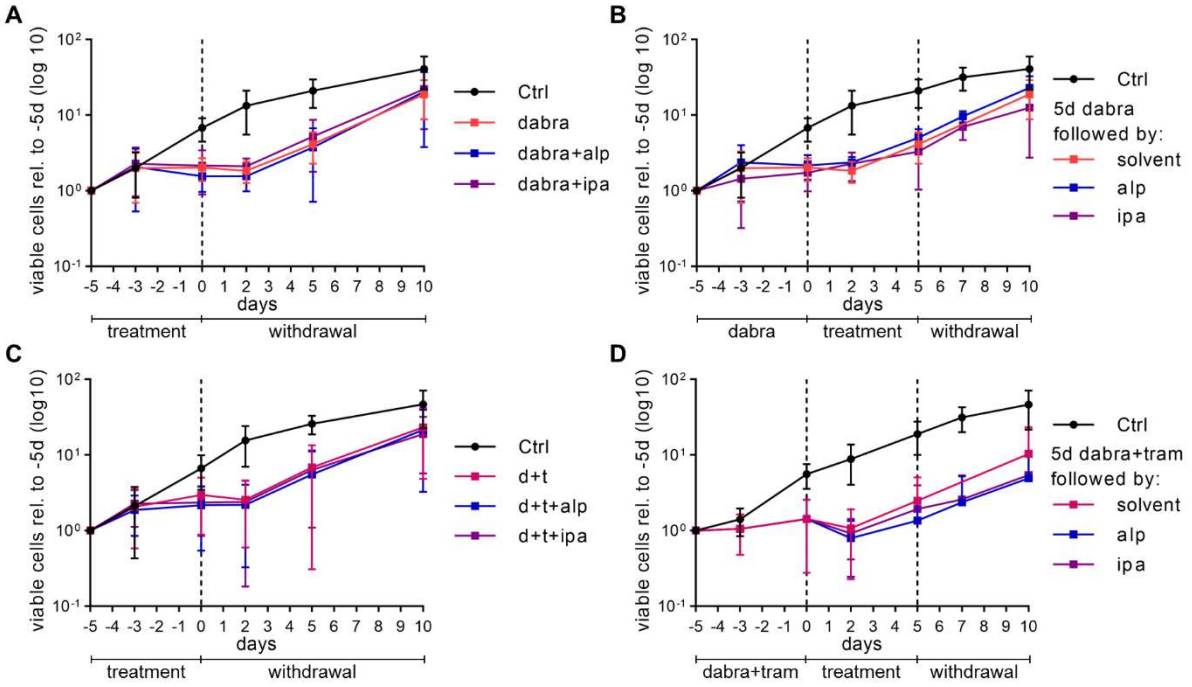

Figure 30 Effect of PI3K/AKT inhibition on rebound growth
(A-B) Viable cell counts during treatment with 5nM dabrafenib (dabra) (A) or 0.3 nM trametinib and 2.7 nM dabrafenib (d+t) (B) alone or in combination with 5 µM alpelisib (alp) or 1 µM ipatasertib (ipa) followed by ten days of withdrawal. Dashed line indicates withdrawal timepoint. Viable cell counts are normalized to treatment start (-5d). Data is shown on a logarithmic scale (base 10) as mean±SD of at least three biological replicates
(C-D) Viable cell counts during treatment with 5 nM dabrafenib (dabra) (C) or 0.3 nM trametinib and 2.7 nM dabrafenib (dabra+tram) (D) followed by withdrawal. During withdrawal cells were either untreated (=solvent) or treated for five days with 5 µM alpelisib (alp) or 1 µM ipatasertib (ipa), followed by five days of withdrawal. Dashed lines indicate withdrawal timepoints. Viable cell counts are normalized to treatment start (-5d). Data is shown on a logarithmic scale (base 10) as mean±SD of at least three biological replicates
This figure was adapted from Kocher *et al.*, under review

Taken together, this suggests that increased AKT signaling does not promote rebound growth in the BT-40 model.

Table 27 Pharmacokinetic data for PI3K/AKT inhibitors used
Plasma-protein-binding was taken from DrugBank[52]
($unbound\ Cmax = Cmax \times \frac{100-PPB}{100}$).
This table was adapted from Kocher *et al.*, under review

Inhibitor	C_{max} [nM]	Plasma-protein-binding (%)	Unbound C_{max} [nM]	Reference for C_{max}
Alpelisip	7243.87	89	796.83	PMID: 37441736
Ipatasertib	1065.5	No information found	N/A	PMID: 32205017

4.3.3 Investigation of autocrine effect of increased CCL2, CX3CL1, CXCL10 and CLL7 expression and secretion during MAPKi treatment and withdrawal

In addition to affecting the tumor microenvironment, cytokines have been shown to have tumor promoting effects on tumor cells directly.[140,141,146,159,160] Therefore, a possible autocrine, rebound-promoting effect of cytokines was investigated. Inhibition of CCL2, CX3CL1, CXCL10 and CCL7 using a combination of neuABs during dabrafenib treatment did not further affect viable cell counts compared to dabrafenib treatment only nor did it influence rebound growth

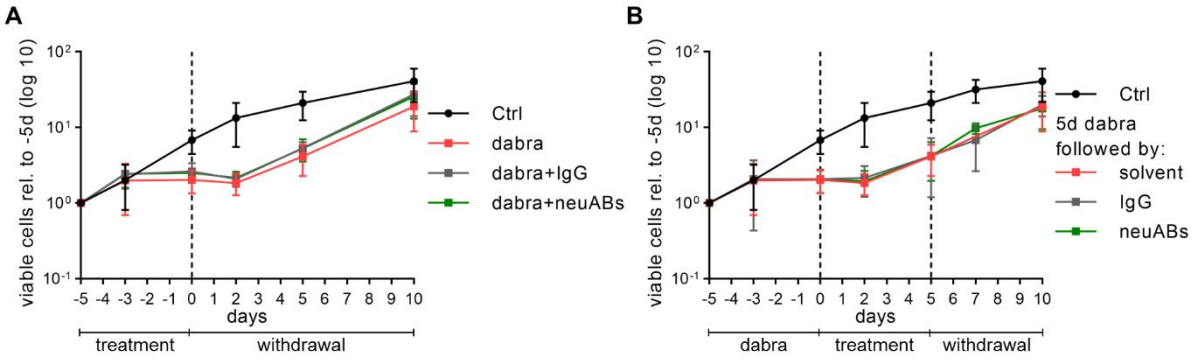

Figure 31 Effect of cytokine inhibition on rebound growth
(A) Viable cell counts during treatment with 5 nM dabrafenib (dabra) alone or in combination with a combination of antibodies neutralizing CCL2 (0.5 µg/mL), CX3CL1 (0.25 µg/mL), CXCL10 (0.25 µg/mL) and CCL7 (0.1 ng/mL) (neuABs) or IgG control (1 µg/mL) followed by ten days of withdrawal. Dashed line indicates withdrawal timepoint. Viable cell counts are normalized to treatment start (-5d). Data is shown on a logarithmic scale (base 10) as mean±SD (n=3 independant biological replicates)
(B) Viable cell counts during treatment with 5 nM dabrafenib (dabra) followed by withdrawal. During withdrawal cells were either untreated (=solvent) or treated for five days with a combination of antibodies neutralizing CCL2 (0.5 µg/mL), CX3CL1 (0.25 µg/mL), CXCL10 (0.25 µg/mL) and CCL7 (0.1 ng/mL) (neuABs) or IgG control (1 µg/mL). Dashed lines indicate withdrawal timepoints. Viable cell counts are normalized to treatment start (-5d). Data is shown on a logarithmic scale (base 10) as mean±SD (n=3 independant biological replicates)
This figure was adapted from Kocher *et al.*, under review

upon treatment withdrawal (Figure 31A). Furthermore, cytokine inhibition during dabrafenib withdrawal did not affect cell regrowth either (Figure 31B).

To summarize, neither inhibition of cytokines, showing increased expression and secretion, nor inhibition of increased AKT activity did affect rebound growth in the BT-40 model, suggesting that neither mechanism has an intrinsic or autocrine rebound growth promoting effect.

4.4 Investigation of a putative tumor cell extrinsic mechanism involving microglia cells

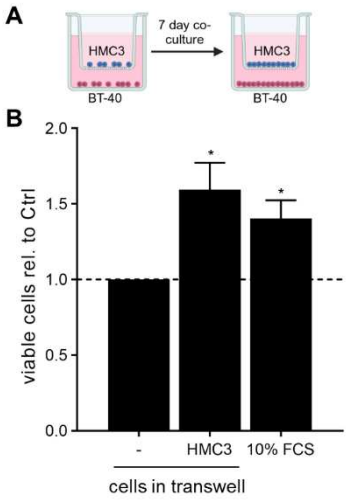

Figure 32 BT-40 – HMC3 transwell co-culture
(A) Schematic of transwell co-culture setup; created using BioRender.com
(B) Viable cell counts of BT-40 after seven days with or without (-) HMC3 co-culture. BT-40 cultured in 10% FCS were used as pos. control. Viable cell counts are shown as mean±SD (n=3 independent biological replicates) relative to control (-). One-sample t-test, * p-value ≤ 0.05

Cytokines, in particular CCL2 and CX3CL1,[216–220] have been shown to attract microglia cells, the main TME cell type in pLGG,[123–125] which have been shown to promote pLGG tumorigenesis *in vivo*.[95] In line with this, I observed increased proliferation of BT-40 cells when co-cultured with the human microglia cell line HMC3 (Figure 32). Therefore, I next investigated whether MAPKi treatment and withdrawal would affect the attraction of microglia cells (Figure 33A), which could possibly exert rebound growth promoting effects.

Indeed, increased migration of the microglia cell line HMC3 was observed when using BT-40 conditioned media (CM) collected during MAPKi treatment and withdrawal compared to CM from untreated cells (Figure 33B,D). Migration of HMC3 cells was not increased using conditioned media from untreated cells compared to fresh media containing 2% FCS, which is also present in the CM (Figure 33B,D). This suggests that BT-40 cells released factors attracting microglia cells upon MAPKi treatment and withdrawal, but not in untreated state.

Increased microglia attraction, observed upon MAPKi treatment withdrawal, was reversed by addition of a combination of antibodies neutralizing CCL2, CX3CL1, CXCL10 and CCL7 to conditioned media (Figure 33C-D), indicating that some or all of these cytokines are involved in mediating the increased microglia attraction.

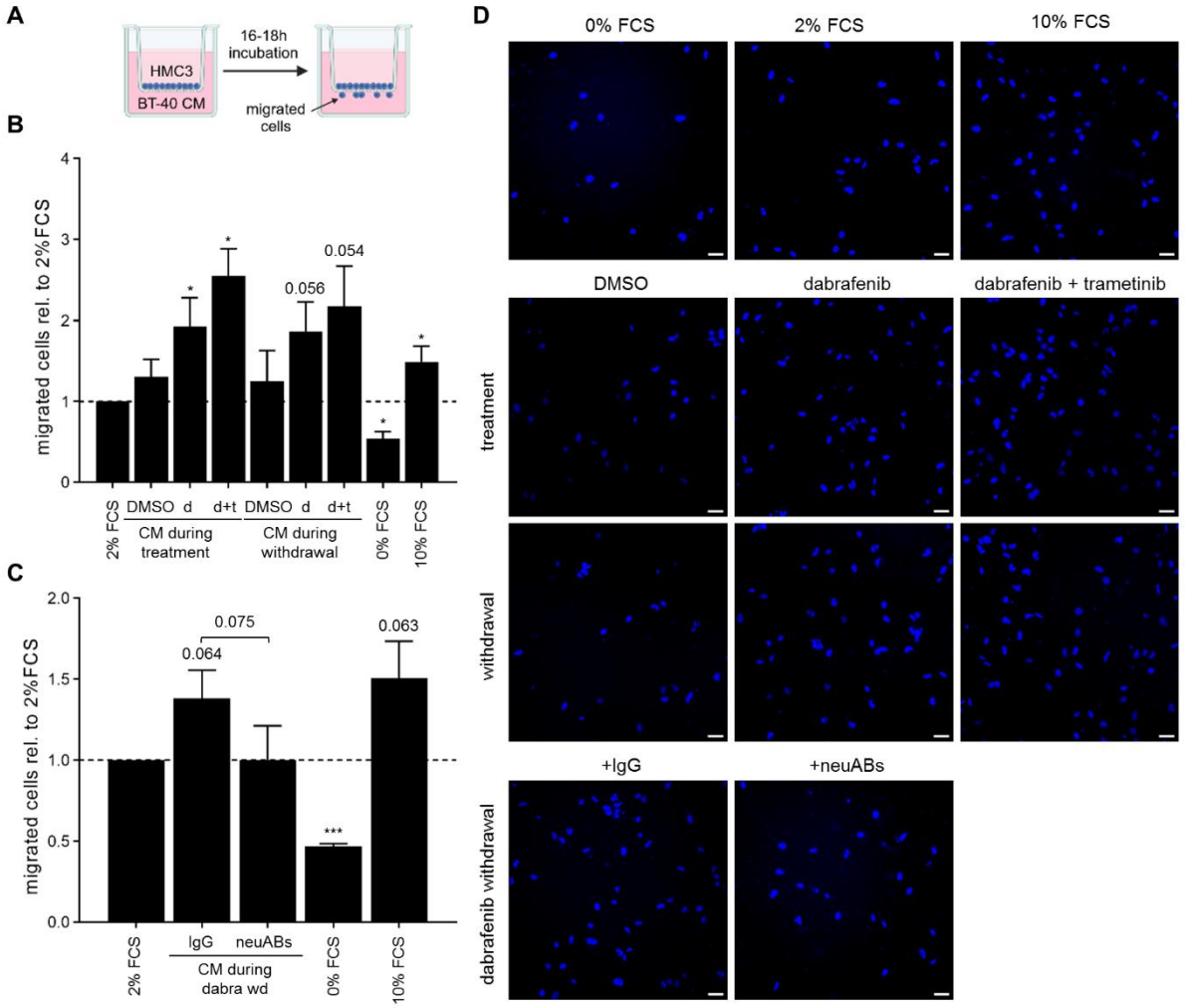

Figure 33 Microglia migration towards BT-40 conditioned media
(A) Schematic of transwell migration assay setup; created using BioRender.com
(B) Transwell migration assay of HMC3 cells towards conditioned media (CM) collected from BT-40 cells after five days treatment with DMSO (solvent control), 5 nM dabrafenib (d) or 2.7 nM dabrafenib and 0.3 nM trametinib (d+t) followed by 24 h of withdrawal. 2% FCS served as baseline control as CM contains 2% FCS, 0% FCS as negative control and 10% FCS as positive control. Quantification of migrated cells is shown as mean±SD (n=3 independent biological replicates) relative to 2% FCS. One-sample t-test, * p-value ≤ 0.05; no indication: not significant
(C) Transwell migration assay of HMC3 cells towards CM collected 24 h after 5 nM dabrafenib withdrawal (dabra wd) containing either a combination of antibodies neutralizing CCL2 (1 µg/mL), CX3CL1 (0.5 µg/mL), CXCL10 (0.5 µg/mL) and CCL7 (0.2 ng/mL) (neuABs) or IgG (2 µg/mL). 2% FCS served as baseline control as CM contains 2% FCS, 0% FCS as negative control and 10% FCS as positive control. Quantification of migrated cells is shown as mean±SD (n=3 independent biological replicates) relative to 2% FCS. One-sample t-test and two-tailed unpaired t-test (comparing IgG to neuABs), * p-value ≤ 0.05 *** p-value ≤ 0.001; no indication: not significant
(D) Representative fluorescence images showing HMC3 migrated through the transwell. Nuclei were stained with DAPI. Scale bar = 50 µM
This figure was adapted from Kocher *et al.*, under review

Taken together, these results suggest a possible paracrine rebound promoting mechanism involving cytokine-mediated microglia attraction, which should be further investigated in future studies using more complex models.

4.5 *In vivo* validation of MAPK pathway reactivation and increased cytokine expression upon dabrafenib treatment and withdrawal

Finally, to investigate the MAPK pathway reactivation upon treatment withdrawal and increased cytokine expression induced by MAPKi treatment *in vivo*, BT-40 cells were engrafted orthotopically in NOD scid gamma (NSG) mice. Treatment with 100 mg/kg dabrafenib once

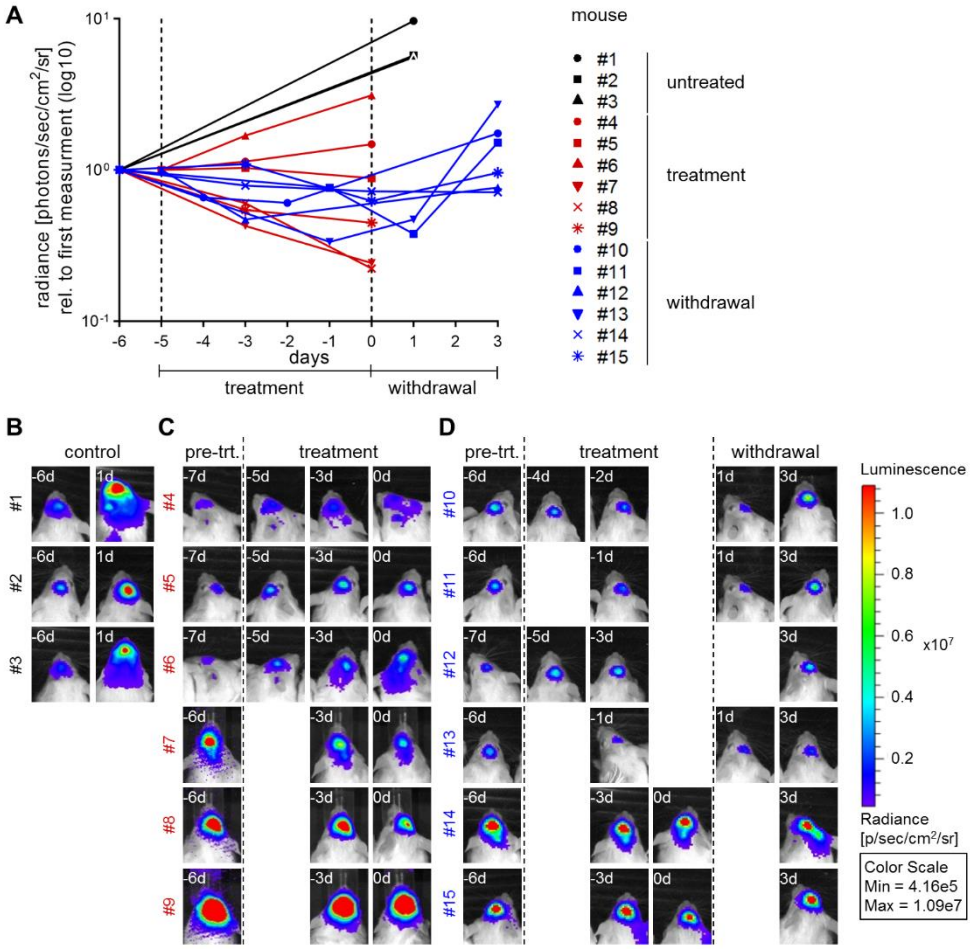

Figure 34 Rebound growth after dabrafenib withdrawal *in vivo*
NOD Scid gamma (NSG) mice carrying orthotopic BT-40 xenograft tumors were treated with 100 mg/kg dabrafenib (treatment; six doses, once daily) followed by three days of withdrawal. Tumor growth was measure by bioluminescence imaging and is shown for each individual animal as radiance in photons/s/cm²/steradian (A). Dashed lines indicate treatment start and stop. Bioluminescence images (B-D) of untreated animals (control, n=3; B), animals undergoing treatment (n=6; C) and animals undergoing treatment followed by withdrawal (n=6; D); pre-trt. = before treatment start.
This figure was adapted from Kocher *et al.*, under review

daily for six days stabilized tumor growth in 10/12 mice (Figure 34). Of note, samples from mice showing tumor progression on treatment (mouse #4 and #6) were excluded from further analysis, as the aim was to investigate gene expression changes during dabrafenib treatment response *in vivo*. Upon treatment stop, tumor regrowth was observed within three days, suggesting rebound growth in the *in vivo* model (Figure 34).

Analysis of gene expression in tumor samples showed decreased *FOS* expression during treatment, indicative of on-target effect, and re-expression during treatment withdrawal compared to untreated tumors (Figure 35A). This is in line with MAPK reactivation patterns observed *in vitro*. Additionally, a trend for increased *CX3CL1* and *CXCL10* expression was observed upon treatment (Figure 35B-C), in line with my *in vitro* data. While *in vitro CX3CL1*

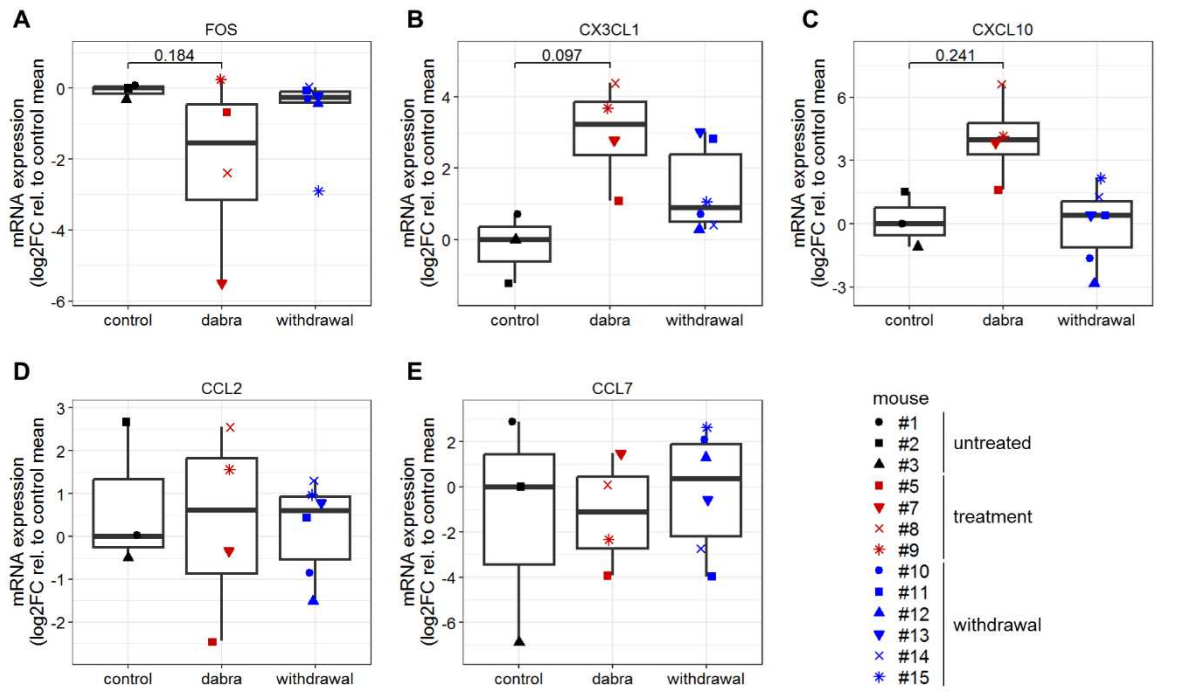

Figure 35 MAPK activity and cytokine gene expression during dabrafenib treatment and withdrawal *in vivo*
RT-qPCR analysis of *FOS* (A), *CX3CL1* (B), *CXCL10* (C), *CCL2* (D) and *CCL7* (E) expression in BT-40 orthotopic xenograft tumors after treatment with dabrafenib (dabra; 100 mg/kg, six doses, once daily) followed by three days of withdrawal (withdrawal). Samples from mice showing tumor progression (#4, #6; Figure 34) during dabrafenib treatment were excluded from the analysis. Quantification was done relative to the median of untreated samples (control). *FOS* (A) was undetected in two samples (#7, #8), *CX3CL1* (B) was undetected in one sample (#2), *CCL2* (D) was undetected in two samples (#2, #7) and *CCL7* (E) was undetected in six samples (#2, #3, #5, #7, #8, #11), for these samples, Ct values were set to 40 (max. number of cycles). Boxplots depict the median, first and third quartiles. Whiskers extend from the hinge to the largest/smallest value no further than 1.5 * IQR from the hinge (where IQR is the interquartile range). Two-tailed unpaired t-test; no indication: not significant (control: n=3 mice, dabra: n=4 mice, withdrawal: n=6 mice)
This figure was adapted from Kocher *et al.*, under review

and *CXCL10* expression was decreased at 72 h of withdrawal compared to earlier withdrawal timepoints, both were still significantly increased at this timepoint (Supplementary Figure 1). In contrast, *in vivo CX3CL1* and *CXCL10* expression was back to baseline levels already after three days of withdrawal (Figure 35B-C). This difference to the *in vitro* data could possibly be explained by differences in drug clearance *in vivo* compared to *in vitro*. Upregulation of *CCL2* and *CCL7*, observed *in vitro*, was not observed upon dabrafenib treatment or withdrawal *in vivo* (Figure 35D-E).

Taken together, these data indicate MAPK pathway reactivation during rebound growth *in vivo* and suggest a possibly increased expression of *CX3CL1* and *CXCL10* upon dabrafenib treatment *in vivo*.

5 Discussion

Rebound growth in pLGG refers to the rapid tumor regrowth observed in a subset of patients after MAPKi treatment stop (Patricia O'Hare et al., Neuro Oncol., under review)[107,117] and constitutes a significant clinical challenge. Rebound growth remains poorly understood and it is neither clear which patients are at risk to experience rebound growth nor how it could be prevented. Both prediction and prevention require a better understanding of the molecular mechanisms driving rebound growth.

5.1 Rebound model development

I successfully modeled tumor rebound growth of pLGG during MAPKi withdrawal *in vitro* using the patient-derived cell line BT-40 (*BRAF*^{V600E}, *CDKN2A/B*del). This model showed 1) response upon MAPKi treatment, and 2) cell regrowth upon treatment withdrawal, which 3) was faster than after SOC chemotherapy treatment, thereby fulfilling my three criteria of a successful rebound model and mimicking what is observed clinically in patients.

In contrast, rebound modeling was not successful in additional patient-derived pLGG models driven by *KIAA1549:BRAF* fusion (DKFZ-BT66, DKFZ-BT308) or *BRAF*^{V600E} mutation (DKFZ-BT314). First of all, in line with previous data,[60,63,64] no effect on viable cell numbers in both proliferating as well as senescent cells was observed during MAPKi treatment using clinically relevant drug concentrations. On the one hand, in proliferating cells, this may be explained by the induction of SV40-TAg which inhibits p53 and pRb[64,85,91] to circumvent OIS otherwise observed in these cells.[64,90] As a consequence, p53-dependant apoptosis is impaired in these cells. Furthermore, pRb is an important cell cycle regulator and its inactivation, which amongst other factors is induced by MAPK activity, is necessary for G1- to S-phase transition.[44,45,221] In case of pRb inhibition through SV40-TAg induction, cell cycle progression can happen independently of MAPK activity, hence MAPK inhibitors are not effective. On the other hand, in senescent cells, the lack of observed effect on viable cell counts upon MAPKi treatment may be explained by their senescent biology. For one, since, by

definition, senescent cells are non-cycling[222] and are arrested most commonly in G1 cell cycle phase,[223] further cell cycle arrest upon MAPKi treatment cannot be observed. Secondly, senescent cells were shown to be resistant to many apoptotic stimuli and generally only undergo apoptosis if treated with so-called senolytic agents, such as BH3-mimetics.[60,63,224] Due to the lack of effect during MAPKi treatment, these models were not suitable to assess presence or absence of rebound growth and they were not further used in this study.

As my rebound model only represents one pLGG tumor entity and molecular background, validation of my discoveries in further models with different genetic backgrounds will be necessary. Given the recent advances in the generation of new pLGG *in vitro* models,[78] this will be possible in future studies. Nevertheless, the BT-40 rebound model represents an important molecular subgroup, as patients with this genetic background (*BRAF*^{V600E} and *CDKN2A/B*del) have the poorest prognosis.[19]

5.2 MAPK overactivation upon treatment withdrawal

Using the BT-40 rebound model, a rapid reactivation (within hours) of the MAPK pathway was observed upon MAPKi withdrawal. As patients experiencing rebound growth usually respond to re-treatment with MAPKi,[107,118] classical resistance mechanism, such as upregulation of PI3K/AKT/mTOR signalling[72,74] or CRAF activity,[76,225] are likely not involved in the rebound growth, making a MAPK-dependent rebound-driving mechanism plausible. Taking this into account, the fast reactivation of the MAPK pathway upon treatment withdrawal is likely to play a role in the rebound growth. While the MAPK pathway is not influenced by chemotherapy treatment and hence active during chemotherapy withdrawal, rapid regrowth is not observed after chemotherapy treatment. This is possibly due to the increased cytotoxicity of chemotherapeutic drugs, which disturb cell division through different mechanisms, e.g. by DNA damage or mitotic anomalies,[226–228] and induce programmed cell death,[227–229] also shown by sub-G0/G1 arrest and increased PARP cleavage in the BT-40 model. Both effects may need longer time to be resolved compared to re-entering of the cell cycle after simple G1-arrest

caused by MAPKi, and therefore possibly cause the observed delayed tumor cell recovery and regrowth after chemotherapy withdrawal compared to MAPKi withdrawal.

The rapid reactivation of the MAPK pathway upon MAPKi withdrawal was additionally associated with a transient overactivation of the pathway observed on the level of MEK phosphorylation and *FOS* gene expression. Pathway overactivation upon drug withdrawal is not uncommon and has been observed with other classes of drugs as well (e.g. METi, PI3Ki or mTORi) where it was associated with upregulation of RTKs or activation of feedback loops involving parallel pathways.[121,230] When it comes to MAPKi, MAPK overactivation after inhibitor withdrawal has also been observed in other MAPK driven tumor entities.[55,231–235] Interestingly, in these studies, focusing on drug resistance and addiction, substantial ERK overactivation, also referred to as pERK rebound, which caused decreased proliferation and cell death, was observed.[55,231–235] Substantial pERK rebound was not observed in the BT-40 rebound model, likely due to the parallel re-expression of DUSP6, a negative regulator of pERK.[236] This highlights a potential vulnerability of pLGGs to DUSP6 inhibitors during MAPKi treatment withdrawal, as it has been shown that DUSP6 inhibition causes cell death due to MAPK overactivation in other models.[237,238] At the moment, no clinically relevant DUSP6 inhibitors are available. Development of phosphatase inhibitors has been challenging due to highly conserved active sites within phosphatase families and the lack of detailed structural information.[239,240] However, improved understanding of phosphatases, including improved structural and mechanistic understanding,[240] as well as advances in drug development, including use of allosteric inhibitors or PROTAC degraders,[239,241] have aided to solve these challenges. This, together with insights into the putative tumor promoting role of DUSPs,[237,238] will likely lead to further investigation of DUSPs as possible anti-cancer drug targets and inhibitors for clinical use may become available in the future.

5.3 Upregulation of AKT signaling upon MAPKi treatment

In addition to rapid MAPK pathway reactivation and overactivation after MAPKi withdrawal, increased AKT signaling was induced in the BT-40 rebound model upon MAPKi and

maintained during early withdrawal. In line with this observation, upregulation of PI3K/AKT/mTOR signaling has also been observed in other tumor types upon MAPK inhibition and usually acts as a compensatory mechanism conferring resistance to MAPKi treatment.[200,209–214,230] Mechanisms described to cause an increased AKT activation upon MAPK inhibition involve increased activation and accumulation of RTKs due to loss of negative feedback regulation mediated by MAPK activity.[201,209,242] Furthermore, active RAS, which may accumulate during MAPK inhibition due to loss of negative feedback regulation,[243,244] can also activate PI3K and thereby lead to increased AKT activity upon MAPKi.[202,245] Indications for increased activity of RTKs or MAPK upstream activators were only observed on the gene expression level (RNAseq) in my multi-omics dataset. Therefore, further investigation is necessary before drawing any conclusions about mechanisms involved in increased AKT activity upon MAPK inhibition in the BT-40 model. Co-targeting of the MAPK and PI3K/AKT/mTOR pathway has shown efficacy across different tumor entities,[214,246–248] even though combination of MAPKi and mTORi has been associated with severe toxicities in adult patients.[248–251] While rebound growth in pLGGs is not associated with resistance,[107,118] increased AKT signaling could still exert growth promoting effects to some extent. Furthermore, combination of MAPKi and mTORi was effective in a pLGG *in vivo* model using subcutaneously injected BT-40 cells.[251] In contrast to this, combination of PI3Ki or AKTi, while showing on-target activity, with MAPKi did not affect cell viability or rebound growth in my BT-40 *in vitro* rebound model. A possible explanation for this could be the lack of microenvironment in the *in vitro* setting, as synergistic activity of mTORi and MEKi in the BT-40 *in vivo* model involved effects related to angiogenesis.[251] Furthermore, in my study, only a PI3K and an AKT inhibitor but no mTOR inhibitor was tested. Differences in efficacy of the different inhibitors as well as the concentrations used could possibly also affect the outcome of the combination treatment.[252]

5.4 Upregulation of cytokines upon MAPKi treatment

Apart from increased AKT activity, MAPK inhibition led to increased cytokine expression and secretion. The mechanisms involved in the increased cytokine expression upon MAPK inhibition in the BT-40 model remain unclear. Inhibition of AKT, which was upregulated upon MAPKi and shown to be involved in the expression of some cytokines,[204,253,254] did not affect the expression of *CCL2, CX3CL1, CXCL10* and *CCL7* in BT-40. Apart from AKT signaling, no strong indications for increased activity of other signaling pathways possibly involved in increased cytokine expression (e.g. JAK/STAT,[255–257] TGF-beta[258–260] or NFkB[208,261–266]) were observed. MAPK activity has been shown to be associated with increased cytokine expression,[204,267–269] meaning its inhibition should decrease cytokine expression. However, few studies also suggest a possible effect of MAPK inhibition on cytokine expression. One study showed that BRAF inhibitors induced IL-1b production in dendritic cells.[270] Another study showed that MAPK inhibition stabilized *CCL2* and *CXCL10* mRNA induced by TNF-alpha in keratinocytes.[271] Whether a similar mechanism is involved in the increased cytokine expression observed in the BT-40 model needs further investigation. Identification of the mechanism leading to increased cytokine expression could be of interest when it comes to targeting cytokine signaling. While inhibitors or antibodies targeting CCL2, CXCL10, CX3CL1 or CCL7 are not clinically available, GPCRs, one of the main receptor type interacting with cytokines,[136] do generally make good drug targets.[272] However, cytokines can often bind to more than one receptor[203] and targeting just one might not be sufficient. Therefore, inhibition of cytokine expression could be a possible way to inhibit cytokine-induced effects. Furthermore, inhibiting cytokine secretion could be a possible strategy. Cytokines can be secreted through exocytosis, involving the endoplasmatic reticulum and golgi apparatus, but also via extracellular vesicles (EVs).[273] The latter may be inhibited by interfering with EV biosynthesis using e.g. sphingomyelinase inhibitors.[274–276]

CCL2,[140–144] CXCL10,[144–151] CX3CL1[156–162] and CCL7[152–155] have been shown to play complex roles in tumor biology and affect both the tumor cells as well as the TME. While all four

chemokines have been shown to have tumor promoting effects on tumor cells,[140,141,146,159,160] inhibition of these chemokines did not affect cell viability or rebound growth in the BT-40 model. While some receptors of these cytokines[203] are expressed in BT-40 based on gene expression, these do not include the canonical receptors for all of the cytokines,[136] which could possibly explain the lack of effect. Furthermore, BT-40 may generally not be dependent on these cytokines. Taken together, my data suggests the absence of an autocrine effect of CCL2, CXCL10, CX3CL1 and CCL7 during rebound growth after MAPKi withdrawal.

5.5 Increased microglia attraction and other influences on the TME

While cytokines did not have an autocrine effect on tumor cell proliferation in the BT-40 rebound model, I could demonstrate increased attraction of microglia cells, mediated by CCL2, CX3CL1, CXCL10 and CCL7, indicating a possible paracrine role during rebound growth. This is in line with their role in attraction of various immune cells,[153,216–220,277–280] including microglia cells in case of CCL2,[216,217,277] CX3CL1[218–220] and CXCL10.[277,278]

Microglia may contribute to the rebound growth by promoting tumor growth, as I observed a growth promoting effect of microglia cells on BT-40 in an untreated state. This is in line with previous data from a study showing the importance of microglia for tumor formation *in vivo*.[95] In this study, it was shown that *BRAF* fusion-driven NSCs produce CCL2 which lead to increased attraction of microglia cells to the tumor site, thereby promoting tumor formation.[95] In contrast to my study, where CCL2 expression was increased upon MAPK inhibition, this study by Chen *et al.* showed that CCL2 expression in NSCs was driven by MAPK activity in connection with NF-kB signaling, and MAPKi treatment abrogated increased CCL2 expression.[95] Possibly, this difference could be explained by the different genetic backgrounds used, *BRAF* fusion vs. mutation. It has been shown that *BRAF*^{V600E}-driven pLGGs have a higher MAPK activity,[82] which could lead to differences in signaling outcomes. Additionally, BT-40 harbor a *CDKN2A/B* deletion, which could further influence differences in molecular outcomes. This highlights the importance of further validation of my results in models with different genetic backgrounds. In addition to different genetic backgrounds used, the study by

Chen *et al.* focused on tumor initiation[95] and differences could also reflect different timepoints in tumor development.

In addition to promoting tumor growth, microglia cells may play a role during MAPKi treatment response, as our group could recently show that increased microglia infiltration correlates with a high predicted MAPK inhibitor sensitivity score (MSS).[82] Furthermore, this study showed that the MSS was high not only in tumor cells but also microglia cells,[82] suggesting that they might also be affected by MAPKi treatment.

MAPK signaling has been shown to be involved in both pro-[281–284] and anti-inflammatory[284-286] effects of monocytic cells, including microglia. This suggests that MAPKi treatment and withdrawal could possibly alter microglia activation states in the pLGG TME, leading to tumor-suppressive effects in case of classical activation (pro-inflammatory, M1-like)[287] or tumor-promoting effects in case of alternative activation (anti-inflammatory, M2-like).[287] Classical/tumor-suppressive activation of microglia upon MAPKi treatment could explain the correlation of a high MSS with microglia infiltration.[82] On the other hand, in case MAPK inhibition or withdrawal would induce alternative/tumor-promoting activation of microglia cells, the use of CSF-1R inhibitors, which induce microglia re-polarization, could be a possible treatment strategy, which has shown efficacy in preclinical glioblastoma models.[288–290] While the CSF-1R inhibitor PLX3397 showed no efficacy in patients with recurrent glioblastoma,[291] preliminary results of a study using the CSF-1R inhibitor BLZ945 in combination with an anti-PD-1 antibody, suggest a possible anti-tumor activity in glioblastoma.[292]

It is important to note that microglia polarization/activation is a complex process and not always as trivial as assigning microglia into M1 or M2 categories. Signatures of both states might co-exist, suggesting that the balance of different stimuli plays an important role in microglia activation.[293–295] Within the TME, microglia cells are exposed to many stimuli, from tumor cells but also other TME cells, such as T cells.[129] In my study, the secretion of only a few cytokines of interest, shown to be upregulated in tumor cells upon MAPKi treatment and during withdrawal, were investigated. CCL2,[296] CXCL10,[278] CX3CL1[297] and CCL7[298] were shown to

induce a rather pro-inflammatory phenotype in microglia/macrophages, which suggests, that microglia cells could be in a tumor-suppressive state during MAPKi treatment and early withdrawal. One should keep in mind though, that my analysis only covered the secretion of selected cytokines, and it is possible that other secreted molecules, not captured in this study, are involved in regulating microglia activation. Additionally, the tumor cell secretome or MAPKi treatment and withdrawal could influence other TME cells, which in turn affect microglia activation. Therefore, future studies will be necessary to investigate the effects of MAPKi treatment and withdrawal on the TME and its interaction with tumor cells, to understand how this may influence response to MAPKi treatment or rebound growth during withdrawal.

In addition to microglia cells, T cells, possibly attracted by CCL10,[280,299] which showed increased expression in my rebound model upon MAPKi treatment both *in vitro* and *in vivo*, could play a role during response to MAPKi treatment and rebound growth upon treatment withdrawal. Depending on the context and type of T cells, they have been shown to exert tumor promoting and suppressing effects in pLGGs. One study, focusing on *NF1*-loss-driven pLGGs, showed that CD8+ T cells, stimulated by neuronal midkine, produced CCL4 which stimulated microglia cells to produce CCL5,[129] critical for NF1-loss-driven glioma growth.[300,301] In contrast, $CD4^+$ T cells were shown to inhibit formation of hiPSC-LGG xenografts through induction of CXCL10 expression in astrocytes.[97] While these studies focused on tumor initiation and growth in untreated states, studies in other MAPK-driven tumors suggest a possible influence of MAPKi treatment on tumor infiltrating T cells. For instance, a study focusing on CRC showed that MAPK inhibition leads to increased T cell infiltration in patient samples.[302] Furthermore, the combination of MAPKi and anti-PD-L1 treatment showed synergistic effects in CRC tumor bearing mice.[302] Another study also suggested synergistic effects of combined MAPKi and anti-PD-L1 treatment and showed that MAPK inhibition did not affect T cell cytotoxicity but protected T cells from exhaustion due to chronic stimulation.[303] Except for one phase I trial suggesting preliminary clinical efficacy of peptide vaccines in recurrent pLGGs,[304] immune therapy has not really been considered for the treatment of pLGGs thus far. Immune

checkpoint inhibition (ICI) in particular was not considered due to the low mutational burden of pLGGs,[305,306] which has been shown to correlate with ICI efficacy in other entities.[307–309] PD-L1 expression was shown to be low in pLGGs, with only some tumors, especially GGs and PXAs, showing a high expression, although these results are based on small sample cohorts.[123,310] While PD-L1 expression is often used as a biomarker for ICI response,[311–313] some studies suggest that it is not a universal biomarker.[314–316] It has been shown that anti-PD-L1 therapy can be beneficial in patients with low PD-L1 expression if used in combination with agents increasing T cell infiltration.[314–316] Taken together, these results indicate a complex role of T cells in anti-tumor immune response and their role during MAPKi treatment and possible combination therapies harnessing anti-tumor T cell responses should be further investigated in pLGGs.

In summary, the above-mentioned studies together with my results suggest a possible complex role of the TME in pLGG biology, including response to MAPKi treatment and rebound growth during treatment withdrawal, which warrants further investigation in future studies. To do so, more complex models, such as organoids or immunocompetent mouse models, will be necessary.

5.6 Limitations

Despite the scarcity of faithful patient-derived pLGG *in vitro* models, I tested several models to generate an *in vitro* rebound model. DKFZ-BT66, DKFZ-BT308 and DKFZ-BT314 did neither respond to treatment nor show rebound growth upon treatment withdrawal when using clinically relevant MAPKi concentrations. Therefore, only BT-40, driven by *BRAF*^{V600E} mutation and *CDKN2A/B*del, could be further used in my study. Validation in newly developed models of different genetic backgrounds is necessary to assess, whether these results also apply to other pLGG molecular subgroups. Additionally, validation in patient samples, important for clinical translation, was not possible at this stage, as tumor samples collected during rebound growth were not available. With the increased use of MAPKi for the treatment of pLGGs, these samples might be available for future studies. Furthermore, my study does not address what

could possibly differentiate patients who experience rebound growth from patients who do not. In order to identify potential biomarkers predicting rebound growth an *in vitro* model showing no rebound growth after effective MAPKi treatment or patient samples would be necessary. Lastly, results indicating a possible involvement of microglia cells were only derived from *in vitro* experiments using an immortalized microglia cell line. Future studies are necessary to investigate this using more suitable models, such as patient-derived/primary microglia, organoids and immunocompetent mouse models.

6 Conclusion and future perspectives

The aim of this project was to describe molecular mechanisms involved in tumor rebound growth after MAPKi withdrawal in pLGG. To do so, I first established an *in vitro* rebound model using the BT-40 cells. Using this model, I could identify a fast MAPK pathway reactivation as a tumor cell intrinsic rebound driving mechanism. Furthermore, increased microglia attraction, mediated by cytokines induced upon MAPKi treatment, was suggested to play a role. Further validation of my findings in additional models and also patient samples is needed.

Nevertheless, this data opens the question whether development of different MAPK inhibitors for treatment of pLGGs is sufficient to improve patient outcome, as MAPK pathway reactivation will most likely occur with any inhibitor upon treatment stop, although exact kinetics might vary across inhibitors. Therefore, investigation of more effective treatment strategies is necessary. These could include the use of different treatment schedules for MAPK inhibitors, including intermittent treatment or drug tapering, to possibly avoid rebound growth due to rapid pathway reactivation. Furthermore, combination treatments, possibly involving DUSP6 inhibition or modulation of the immune microenvironment, which was suggested to play a role by my data, should be considered.

To investigate the role of the TME during MAPKi treatment and withdrawal, additional models are necessary. This should include the use of primary microglia cells instead of an immortalized cell line. Primary microglia can be isolated from rodent brains.[317,318] Furthermore, primary microglia cells can also be isolated from human specimen, such as perioperative or fetal brain tissue as well as tumor samples, although sample availability and frequency may be limited.[317,318] Additionally, microglia cells can be derived through iPSC differentiation.[317,318] Generally, for the study of tumor-immune-interactions, more complex models than “simple” co-cultures are preferred.[318] These can include the use of organotypic slice cultures[318–321] or organoids, a technology that has advanced significantly in the last years.[318,321–323]

In addition to *in vitro* models, *in vivo* models are of importance in studying TME interactions. For this, immunocompetent models are necessary, which at the moment limits the use of PDX

models, as these commonly only engraft in immunocompromised mice.[324] Depending on the model and research question, the use of partially immunocompromised mice lacking functional adaptive immune cells, such as *Rag1* deficient mice,[325] which have been shown to allow pLGG growth,[97] or athymic mice[326] could be useful to study the role of innate immune cells, e.g. microglia. Furthermore, the use of humanized mouse models[78,97,327] or genetically engineered mouse models[78,129,327] are of interest to study TME interactions.

Using some of the above describe models, based on my data together with other published work, it would be of particular interest to further study the role of microglia cells during MAPKi treatment and withdrawal. Questions to answer include the following: What effect does MAPKi treatment and withdrawal have on microglia viability, proliferation, migration and polarization/activation in pLGGs? How does the tumor cell secretome change upon MAPKi treatment and withdrawal and what effect does this have on the interaction between tumor and microglia cells? Could targeting microglia cells be a potential therapeutic option for the treatment of pLGGs, possibly in combination with MAPKi?

Future studies will likely shed more light on this and lead to improved therapeutic strategies, focusing not only on tumor cells but also the TME, to further improve the outcome and especially quality of life of pLGG patients.

7 Supplementary material

7.1 Supplementary Figures

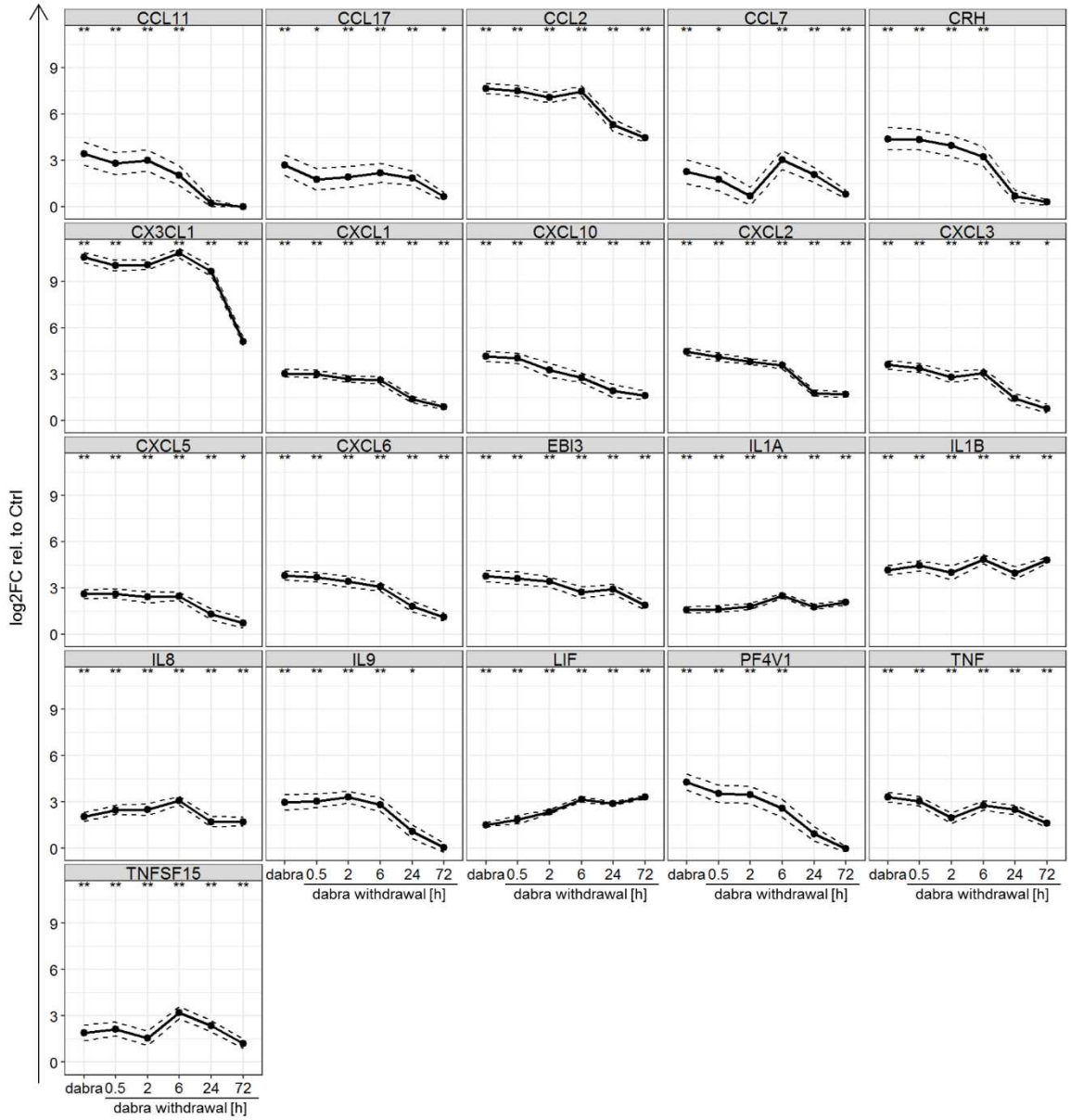

Supplementary Figure 1 Cytokine gene expression in BT-40
Cytokine gene expression, as determined by RNAseq, during treatment for five days with 5 nM dabrafenib (dabra) followed by withdrawal. Data is shown as log2 fold-change (log2FC) relative to solvent control (five days DMSO; Ctrl) as mean±SE (n=3 independent biological replicates). Wald test, Benjamini-Hochberg p-value correction, * adj-p-value ≤ 0.05 ** adj-p-value ≤ 0.01 *** adj-p-value ≤ 0.01; no indication: not significant
This figure was adapted from Kocher *et al.*, under review

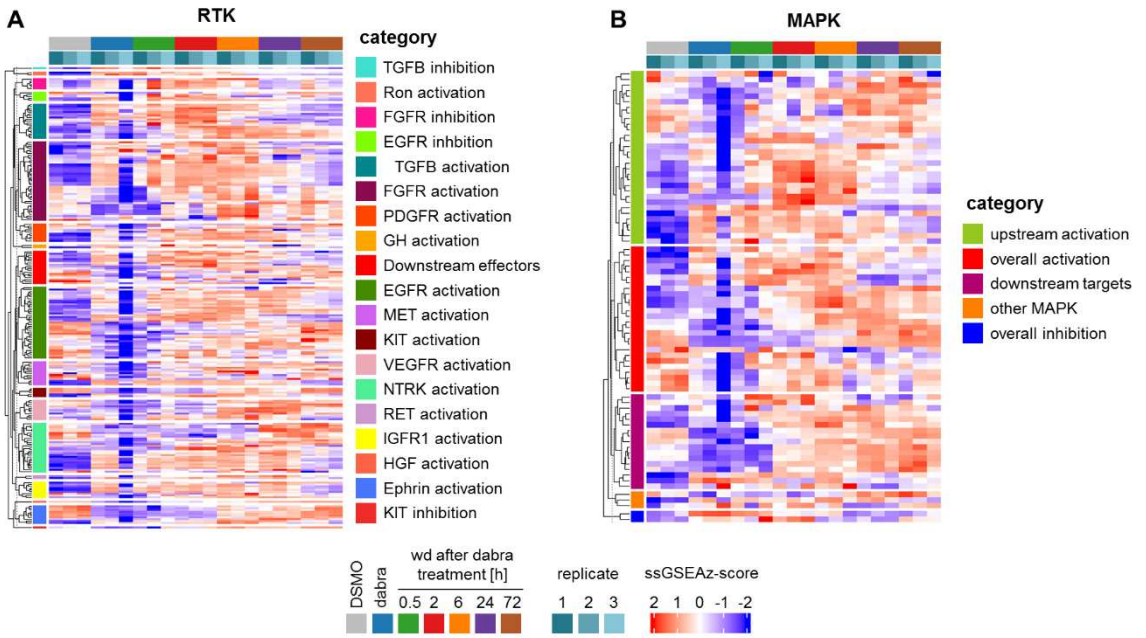

Supplementary Figure 2 ssGSEA analysis of RNAseq dataset
Heatmap showing ssGSEA z-scores for RTK (A) or MAPK (B) related gene signatures taken from the MSigDB C2 subcollection CP (canonical pathways) in RNAseq samples after five days of treatment with DMSO (solvent control) or 5 nM dabrafenib (dabra) followed by withdrawal (wd)

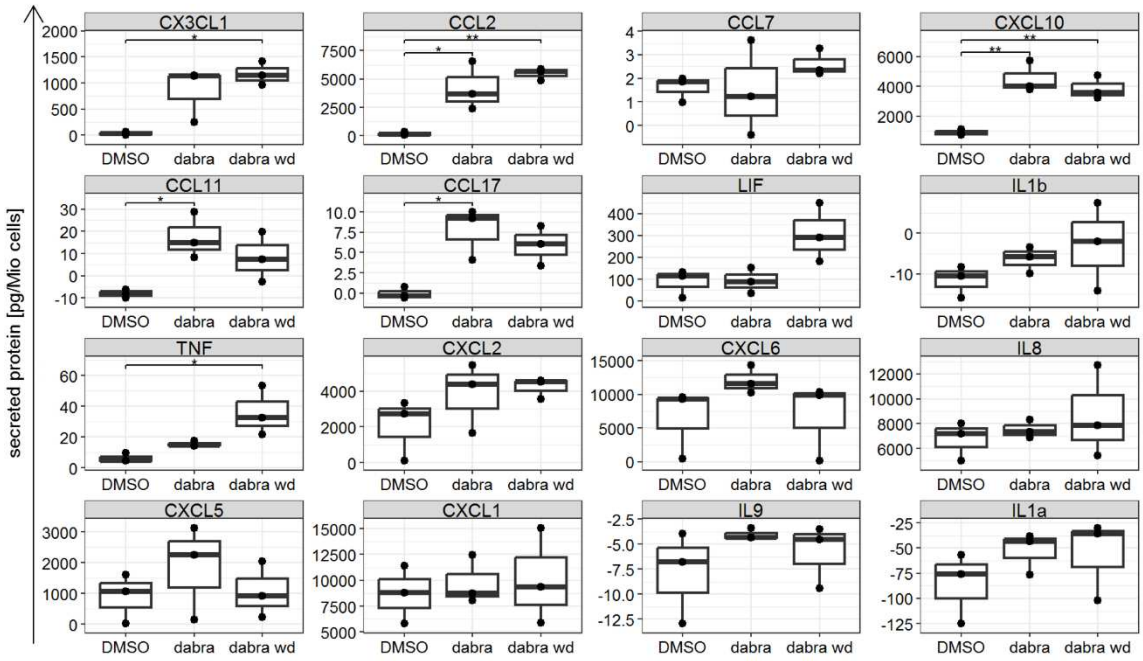

Supplementary Figure 3 Cytokine secretion during dabrafenib treatment and withdrawal in BT-40

Luminex-based multiplex assay results showing cytokine secretion after five days treatment with DMSO (solvent control) or 5 nM dabrafenib (dabra) and 24 h after dabrafenib withdrawal (dabra wd). For all conditions, conditioned media was collected 24 h after the last medium change. Boxplots depict the median, first and third quartiles. Whiskers extend from the hinge to the largest/smallest value no further than 1.5 * IQR from the hinge (where IQR is the interquartile range) n=3 independent biological replicates. One-way ANOVA, Tukey post-hoc test, * adj-p-value ≤ 0.05 ** adj-p-value ≤ 0.01 ** adj-p-value ≤ 0.01; no indication: not significant

This figure was adapted from Kocher *et al.*, under review

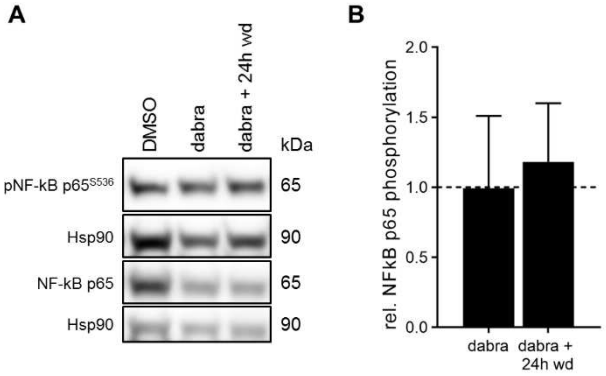

Supplementary Figure 4 NF-kB activity during dabrafenib treatment and withdrawal

Western blot analysis of NF-kB p65 phosphorylation during five days of treatment with DMSO (solvent control) or 5 nM dabrafenib (dabra) followed by 24 h of withdrawal (wd). Blots shown are representative of three biological replicates (A). Quantification (B) was done relative to DMSO (dashed line) and is shown as mean±SD (n=3 independent biological replicates). One-sample t-test; no indication: not significant

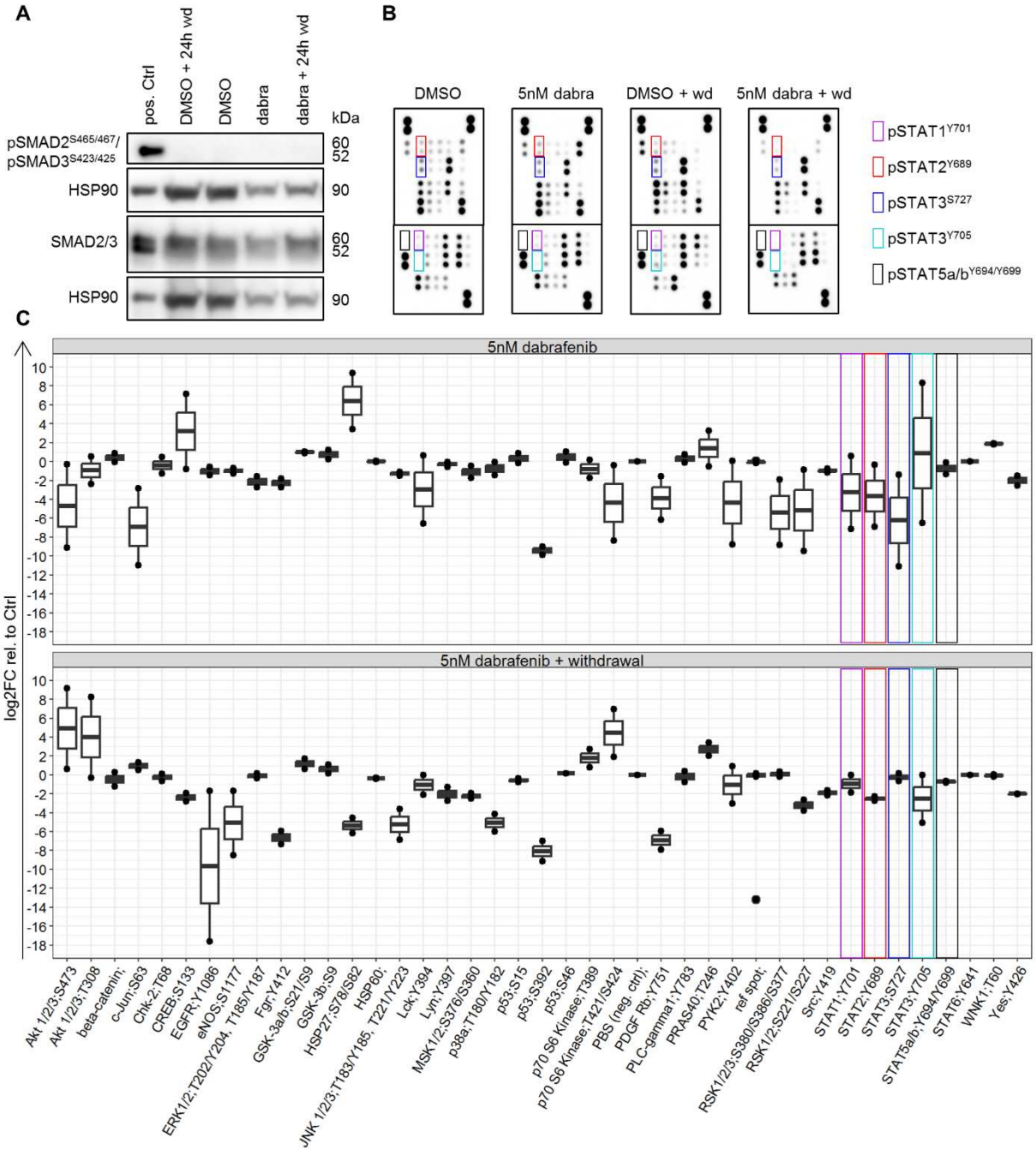

Supplementary Figure 5 Validation of increased TGF-beta and JAK/STAT activity predicted by multi-omics data

(A) Western blot analysis of SMAD2/3 phosphorylation during five days treatment with either DMSO (solvent control) or 5 nM dabrafenib (dabra), followed by 24 h withdrawal (wd). Cell extract of HT-1080 treated with 10 ng/mL TGF-beta for 30 min was used as a positive control (pos. Ctrl). Blots shown are representative of three independent biological replicates.

(B-C) Kinase phosphorylation array of samples treated for five days with 5 nM dabrafenib or DMSO (solvent control) followed by 24 h withdrawal (wd). Arrays (B) consist of two membranes, each target is detected in duplicates. Arrays shown are representative of two biological replicates. Arrays shown are the same as in Figure 28A but at a higher exposure time. Quantification (C) is shown as log2FC relative to the respective DMSO control. Boxplots depict the median, first and third quartiles. Whiskers extend from the hinge to the largest/smallest value no further than 1.5 * IQR from the hinge (where IQR is the interquartile range) n=2 independent biological replicates

This figure was adapted from Kocher *et al.*, under review

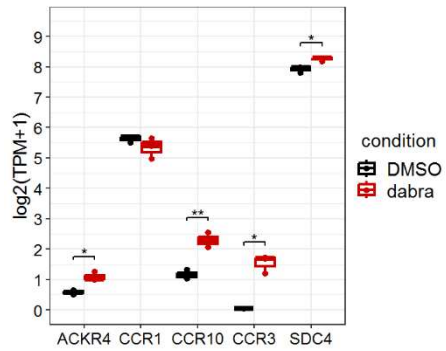

Supplementary Figure 6 Cytokine receptor expression in BT-40

Cytokine receptor gene expression in log2(TPM+1), determined by RNAseq, during treatment for five days with DMSO or 5 nM dabrafenib (dabra). Boxplots depict the median, first and third quartiles. Whiskers extend from the hinge to the largest/smallest value no further than 1.5 * IQR from the hinge (where IQR is the interquartile range) n=3 independent biological replicates. Two-tailed unpaired t-test, p-value ≤ 0.05 ** p-value ≤ 0.01 *** p-value ≤ 0.01; no indication: not significant

This figure was adapted from Kocher *et al.*, under review

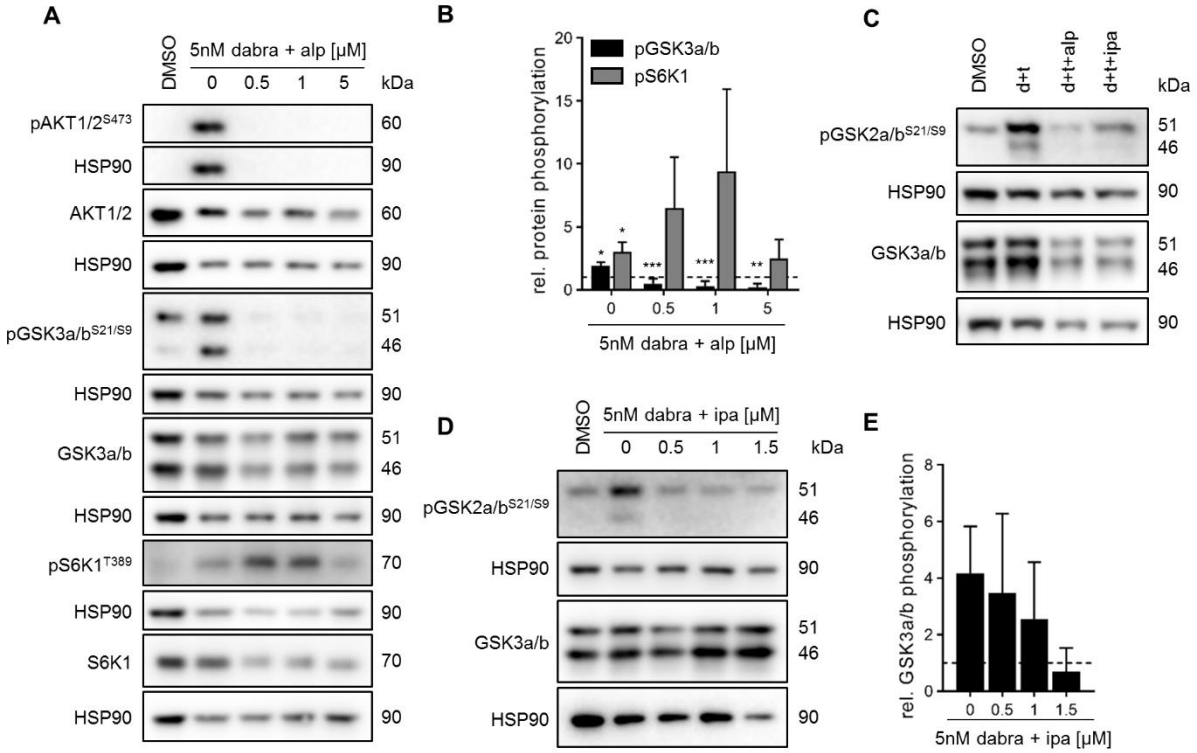

Supplementary Figure 7 Alpelisib and ipatasertib on-target effect

(A-B) Western blot analysis of AKT activity markers after five days treatment with 5 nM dabrafenib (dabra) alone or in combination with alpelisib (alp). Blots shown are representative of three independent biological replicates (A). Quantification (B) is relative to solvent control (DMSO; dashed line) and shown as mean±SD n=3 independent biological replicates). One-sample t-test, p-value ≤ 0.05 ** p-value ≤ 0.01 *** p-value ≤ 0.01

(C) Western blot analysis of GSK3a/b phosphorylation after five days treatment with 2.7 nM dabrafenib and 0.3 nM trametinib (d+t) alone or in combination with either 5 µM alpelisib (alp) or 1 µM ipatasertib (ipa). Blots shown are representative of three independent biological replicates

(D-E) Western blot analysis of GSK3a/b phosphorylation after five days treatment with 5 nM dabrafenib (dabra) alone or in combination with ipatasertib (ipa). Blots shown are representative of three independent biological replicates (D). Quantification (E) is relative to solvent control (DMSO; dashed line) and shown as mean±SD (n=3 independent biological replicates). One-sample t-test; no indication: not significant

This figure was adapted from Kocher *et al.*, under review

7.2 Supplementary Tables

Supplementary Table 1 GO-Term enrichment analysis of upregulated genes
p-value adjusted using Bonferroni step-down
This table was adapted from Kocher *et al.*, under review

GO-Term ID	GO-Term name	% associated genes	p-value	adj-p-value
GO:0004252	serine-type endopeptidase activity	13.91	4.10E-05	2.11E-02
GO:0005102	signaling receptor binding	11.03	3.27E-09	1.73E-06
GO:0005125	cytokine activity	17.12	9.39E-08	4.94E-05
GO:0005126	cytokine receptor binding	14.83	6.75E-06	3.52E-03
GO:0005509	calcium ion binding	11.21	4.55E-05	2.34E-02
GO:0005539	glycosaminoglycan binding	15.12	1.13E-05	5.87E-03
GO:0008009	chemokine activity	28.85	2.80E-06	1.46E-03
GO:0008083	growth factor activity	17.34	7.69E-06	4.00E-03
GO:0008201	heparin binding	16.67	1.25E-05	6.49E-03
GO:0008236	serine-type peptidase activity	13.35	8.70E-05	4.45E-02
GO:0017171	serine hydrolase activity	13.80	2.67E-05	1.38E-02
GO:0019838	growth factor binding	17.73	2.92E-05	1.51E-02
GO:0030020	extracellular matrix structural constituent conferring tensile strength	36.59	8.50E-08	4.48E-05
GO:0030545	signaling receptor regulator activity	13.18	2.40E-07	1.25E-04
GO:0030546	signaling receptor activator activity	13.65	1.19E-07	6.22E-05
GO:0045236	CXCR chemokine receptor binding	55.56	1.05E-07	5.54E-05
GO:0048018	receptor ligand activity	13.86	6.46E-08	3.41E-05
GO:0048407	platelet-derived growth factor binding	81.82	2.75E-09	1.46E-06
GO:0099094	ligand-gated cation channel activity	15.12	8.59E-05	4.41E-02

Supplementary Table 2 GO-Term enrichment analysis of upregulated proteins
p-value adjusted using Bonferroni step-down
This table was adapted from Kocher *et al.*, under review

GO-Term ID	GO-Term name	% associated genes	p-value	adj-p-value
GO:0008093	cytoskeletal anchor activity	12.50	2.57E-04	7.70E-04
GO:0017166	vinculin binding	21.43	4.79E-05	2.40E-04
GO:0019838	growth factor binding	5.67	7.27E-07	5.09E-06
GO:0030145	manganese ion binding	4.05	6.81E-03	6.81E-03
GO:0045295	gamma-catenin binding	16.67	1.06E-04	4.23E-04
GO:0048156	tau protein binding	6.25	2.00E-03	4.01E-03
GO:0050431	transforming growth factor beta binding	14.81	1.11E-05	6.66E-05

Supplementary Table 3 GO-Term enrichment analysis of downregulated genes
p-value adjusted using Bonferroni step-down
This table was adapted from Kocher *et al.*, under review

GO-Term ID	GO-Term name	% associated genes	p-value	adj-p-value
GO:0000079	regulation of cyclin-dependent protein serine/threonine kinase activity	11.57	1.92E-04	4.34E-02
GO:0000166	nucleotide binding	5.75	8.46E-08	2.22E-05
GO:0000217	DNA secondary structure binding	32.43	6.00E-09	1.62E-06
GO:0000400	four-way junction DNA binding	35.29	2.47E-05	5.78E-03
GO:0003677	DNA binding	5.08	1.23E-04	2.84E-02
GO:0003678	DNA helicase activity	24.71	4.42E-12	1.23E-09
GO:0003684	damaged DNA binding	14.29	1.43E-04	3.28E-02
GO:0003688	DNA replication origin binding	38.10	5.25E-07	1.34E-04
GO:0003697	single-stranded DNA binding	16.91	1.51E-09	4.11E-07
GO:0003887	DNA-directed DNA polymerase activity	35.00	9.94E-11	2.73E-08
GO:0003896	DNA primase activity	85.71	1.93E-08	5.16E-06
GO:0004386	helicase activity	12.43	9.54E-07	2.37E-04
GO:0004672	protein kinase activity	7.15	3.77E-09	1.02E-06
GO:0004674	protein serine/threonine kinase activity	7.24	1.07E-06	2.64E-04
GO:0004693	cyclin-dependent protein serine/threonine kinase activity	10.67	1.80E-04	4.09E-02
GO:0005524	ATP binding	6.35	1.80E-07	4.65E-05

GO:0008017	microtubule binding	13.85	5.89E-13	1.64E-10
GO:0008092	cytoskeletal protein binding	7.02	1.82E-07	4.70E-05
GO:0008094	ATP-dependent activity, acting on DNA	16.90	6.74E-10	1.84E-07
GO:0010997	anaphase-promoting complex binding	66.67	2.17E-07	5.58E-05
GO:0015631	tubulin binding	10.76	4.40E-10	1.21E-07
GO:0016301	kinase activity	6.57	3.37E-08	8.97E-06
GO:0016462	pyrophosphatase activity	6.03	1.29E-05	3.11E-03
GO:0016772	transferase activity, transferring phosphorus-containing groups	6.90	6.27E-11	1.73E-08
GO:0016773	phosphotransferase activity, alcohol group as acceptor	6.58	1.26E-07	3.27E-05
GO:0016779	nucleotidyltransferase activity	10.40	2.77E-05	6.42E-03
GO:0016817	hydrolase activity, acting on acid anhydrides	6.01	1.40E-05	3.34E-03
GO:0016818	hydrolase activity, acting on acid anhydrides, in phosphorus-containing anhydrides	6.01	1.40E-05	3.34E-03
GO:0016887	ATP hydrolysis activity	9.49	5.98E-07	1.51E-04
GO:0016888	endodeoxyribonuclease activity, producing 5'-phosphomonoesters	33.33	1.66E-04	3.79E-02
GO:0017076	purine nucleotide binding	5.72	7.32E-07	1.84E-04
GO:0017108	5'-flap endonuclease activity	62.50	3.87E-06	9.48E-04
GO:0017111	nucleoside-triphosphatase activity	6.06	1.55E-05	3.67E-03
GO:0017116	single-stranded DNA helicase activity	56.00	3.23E-14	9.08E-12
GO:0030554	adenyl nucleotide binding	6.35	8.40E-08	2.21E-05
GO:0032147	activation of protein kinase activity	10.18	1.65E-05	3.89E-03
GO:0032553	ribonucleotide binding	5.70	8.65E-07	2.16E-04
GO:0032555	purine ribonucleotide binding	5.71	8.89E-07	2.21E-04
GO:0032559	adenyl ribonucleotide binding	6.40	5.81E-08	1.54E-05
GO:0034061	DNA polymerase activity	15.74	5.97E-07	1.51E-04
GO:0035173	histone kinase activity	33.33	3.58E-05	8.28E-03
GO:0035639	purine ribonucleoside triphosphate binding	5.56	7.60E-06	1.85E-03

GO:0043085	positive regulation of catalytic activity	6.12	1.36E-05	3.25E-03
GO:0043138	3'-5' DNA helicase activity	37.50	1.65E-05	3.88E-03
GO:0043168	anion binding	5.31	6.66E-06	1.63E-03
GO:0043549	regulation of kinase activity	7.37	3.74E-07	9.57E-05
GO:0045859	regulation of protein kinase activity	7.64	5.83E-07	1.48E-04
GO:0048256	flap endonuclease activity	55.56	8.44E-06	2.04E-03
GO:0051338	regulation of transferase activity	8.48	3.27E-12	9.09E-10
GO:0051347	positive regulation of transferase activity	8.59	1.18E-08	3.17E-06
GO:0071900	regulation of protein serine/threonine kinase activity	8.11	2.56E-05	5.96E-03
GO:0140097	catalytic activity, acting on DNA	13.13	5.42E-13	1.52E-10
GO:1900262	regulation of DNA-directed DNA polymerase activity	57.14	9.81E-09	2.64E-06
GO:1900264	positive regulation of DNA-directed DNA polymerase activity	57.14	9.81E-09	2.64E-06
GO:1901265	nucleoside phosphate binding	5.75	8.67E-08	2.26E-05
GO:1903932	regulation of DNA primase activity	100.00	7.60E-08	2.01E-05
GO:1903934	positive regulation of DNA primase activity	100.00	7.60E-08	2.01E-05
GO:1904666	regulation of ubiquitin protein ligase activity	26.67	1.12E-05	2.69E-03
GO:1904668	positive regulation of ubiquitin protein ligase activity	50.00	2.17E-06	5.33E-04

Supplementary Table 4 GO-Term enrichment analysis of downregulated genes
p-value adjusted using Bonferroni step-down
This table was adapted from Kocher *et al.*, under review

GO-Term ID	GO-Term name	% associated genes	p-value	adj-p-value
GO:0003678	DNA helicase activity	8.24	5.25E-06	3.67E-05
GO:0003688	DNA replication origin binding	14.29	5.96E-04	1.19E-03
GO:0003697	single-stranded DNA binding	5.15	1.11E-04	4.43E-04
GO:0004386	helicase activity	5.08	1.26E-05	6.30E-05
GO:0008094	ATP-dependent activity, acting on DNA	6.34	2.09E-06	1.67E-05
GO:0016796	exonuclease activity, active with either ribo- or deoxyribonucleic acids and producing 5'-phosphomonoesters	4.62	1.52E-02	1.52E-02
GO:0016887	ATP hydrolysis activity	4.34	4.38E-08	4.38E-07
GO:0017116	single-stranded DNA helicase activity	24.00	3.65E-08	4.01E-07
GO:0035173	histone kinase activity	16.67	3.72E-04	1.12E-03
GO:0043138	3'-5' DNA helicase activity	25.00	6.58E-06	3.95E-05
GO:0140097	catalytic activity, acting on DNA	4.18	4.99E-07	4.50E-06

8 References

1. Ferlay, J. *et al.* Global Cancer Observatory: Cancer Today. *Lyon, France: International Agency for Research on Cancer* https://gco.iarc.fr/today (2020). Accessed: 15.01.2024

2. Siegel, D. A. *et al.* Counts, incidence rates, and trends of pediatric cancer in the United States, 2003-2019. *JNCI J. Natl. Cancer Inst.* **115**, 1337–1354 (2023).

3. Steliarova-Foucher, E. *et al.* International incidence of childhood cancer, 2001–10: a population-based registry study. *Lancet Oncol.* **18**, 719–731 (2017).

4. Ostrom, Q. T. *et al.* CBTRUS Statistical Report: Pediatric Brain Tumor Foundation Childhood and Adolescent Primary Brain and Other Central Nervous System Tumors Diagnosed in the United States in 2014–2018. *Neuro. Oncol.* **24**, iii1–iii38 (2022).

5. Louis, D. N. *et al.* The 2021 WHO classification of tumors of the central nervous system: A summary. *Neuro. Oncol.* **23**, 1231–1251 (2021).

6. Manoharan, N., Liu, K. X., Mueller, S., Haas-Kogan, D. A. & Bandopadhayay, P. Pediatric low-grade glioma: Targeted therapeutics and clinical trials in the molecular era. *Neoplasia (United States)* **36**, 100857 (2023).

7. Jones, D. T. W., Bandopadhayay, P. & Jabado, N. The Power of Human Cancer Genetics as Revealed by Low-Grade Gliomas. *Annu. Rev. Genet.* **53**, 483–503 (2019).

8. Bandopadhayay, P. *et al.* Long-term outcome of 4,040 children diagnosed with pediatric low-grade gliomas: An analysis of the Surveillance Epidemiology and End Results (SEER) database. *Pediatr. Blood Cancer* **61**, 1173–1179 (2014).

9. Krishnatry, R. *et al.* Clinical and treatment factors determining long-term outcomes for adult survivors of childhood low-grade glioma: A population-based study. *Cancer* **122**, 1261–1269 (2016).

10. Armstrong, G. T. *et al.* Survival and long-term health and cognitive outcomes after low-grade glioma. *Neuro. Oncol.* **13**, 223–234 (2011).

11. Ryall, S. *et al.* Integrated Molecular and Clinical Analysis of 1,000 Pediatric Low-Grade Gliomas. *Cancer Cell* **37**, 569-583.e5 (2020).

12. Shapiro, J. A. *et al.* OpenPBTA: The Open Pediatric Brain Tumor Atlas. *Cell Genomics* **3**, 100340 (2023).

13. Hardin, E. C. *et al.* LOGGIC Core BioClinical Data Bank: Added clinical value of RNA-Seq in an international molecular diagnostic registry for pediatric low-grade glioma patients. *Neuro. Oncol.* **25**, 2087–2097 (2023).

14. Sturm, D. *et al.* Multiomic neuropathology improves diagnostic accuracy in pediatric neuro-oncology. *Nat. Med.* **29**, 917–926 (2023).

15. Jones, D. T. W. *et al.* Tandem duplication producing a novel oncogenic BRAF fusion gene defines the majority of pilocytic astrocytomas. *Cancer Res.* **68**, 8673–8677 (2008).

16. Tran, N. H., Wu, X. & Frost, J. A. B-Raf and Raf-1 are regulated by distinct autoregulatory mechanisms. *J. Biol. Chem.* **280**, 16244–16253 (2005).

17. Cin, H. *et al.* Oncogenic FAM131B-BRAF fusion resulting from 7q34 deletion comprises an alternative mechanism of MAPK pathway activation in pilocytic astrocytoma. *Acta Neuropathol.* **121**, 763–774 (2011).

18. Roth, J. J. *et al.* Chromosome band 7q34 deletions resulting in KIAA1549-BRAF and

FAM131B-BRAF fusions in pediatric low-grade gliomas. *Brain Pathol.* **25**, 182–192 (2015).

19. Lassaletta, A. *et al.* Therapeutic and Prognostic Implications of BRAF V600E in Pediatric Low-Grade Gliomas. *J. Clin. Oncol.* **35**, 2934–2941 (2017).

20. Khatua, S., Gutmann, D. H. & Packer, R. J. Neurofibromatosis type 1 and optic pathway glioma: Molecular interplay and therapeutic insights. *Pediatr. Blood Cancer* **65**, e26838 (2018).

21. Plotnikov, A., Zehorai, E., Procaccia, S. & Seger, R. The MAPK cascades: Signaling components, nuclear roles and mechanisms of nuclear translocation. *Biochim. Biophys. Acta - Mol. Cell Res.* **1813**, 1619–1633 (2011).

22. Coulombe, P. & Meloche, S. Atypical mitogen-activated protein kinases: Structure, regulation and functions. *Biochimica et Biophysica Acta - Molecular Cell Research* vol. 1773 1376–1387 (2007).

23. Lavoie, H., Gagnon, J. & Therrien, M. ERK signalling: a master regulator of cell behaviour, life and fate. *Nature Reviews Molecular Cell Biology* vol. 21 607–632 (2020).

24. Schlessinger, J. How receptor tyrosine kinases activate ras. *Trends Biochem. Sci.* **18**, 273–275 (1993).

25. Boriack-Sjodin, P. A., Margarit, S. M., Bar-Sagi, D. & Kuriyan, J. The structural basis of the activation of Ras by Sos. *Nature* **394**, 337–343 (1998).

26. Cargnello, M. & Roux, P. P. Activation and Function of the MAPKs and Their Substrates, the MAPK-Activated Protein Kinases. *Microbiol. Mol. Biol. Rev.* **75**, 50–83 (2011).

27. Wei, Z. & Liu, H. T. MAPK signal pathways in the regulation of cell proliferation in mammalian cells. *Cell Res.* **12**, 9–18 (2002).

28. Terrell, E. M. & Morrison, D. K. Ras-Mediated Activation of the Raf Family Kinases. *Cold Spring Harb. Perspect. Med.* **9**, (2019).

29. Marshall, C. J. Ras effectors. *Curr. Opin. Cell Biol.* **8**, 197–204 (1996).

30. Kyriakis, J. M. *et al.* Raf-1 activates MAP kinase-kinase. *Nature* **358**, 417–421 (1992).

31. Crews, C. M. & Erikson, R. L. Purification of a marine protein-tyrosine/threonine kinase that phosphorylates and activates the Erk-1 gene product: Relationship to the fission yeast byr1 gene product. *Proc. Natl. Acad. Sci. U. S. A.* **89**, 8205–8209 (1992).

32. Liu, F., Yang, X., Geng, M. & Huang, M. Targeting ERK, an Achilles' Heel of the MAPK pathway, in cancer therapy. *Acta Pharmaceutica Sinica B* vol. 8 552–562 (2018).

33. Hauge, C. & Frödin, M. RSK and MSK in MAP kinase signalling. *J. Cell Sci.* **119**, 3021–3023 (2006).

34. Li, Q. J. *et al.* MAP kinase phosphorylation-dependent activation of Elk-1 leads to activation of the co-activator p300. *EMBO J.* **22**, 281–291 (2003).

35. Yang, S. H., Shore, P., Willingham, N., Lakey, J. H. & Sharrocks, A. D. The mechanism of phosphorylation-inducible activation of the ETS-domain transcription factor Elk-1. *EMBO J.* **18**, 5666–5674 (1999).

36. Ram, A. *et al.* A guide to ERK dynamics, part 2: downstream decoding. *Biochem. J.* **480**, 1909–1928 (2023).

37. Wu, Z., Nicoll, M. & Ingham, R. J. AP-1 family transcription factors: a diverse family of proteins that regulate varied cellular activities in classical hodgkin lymphoma and ALK+

ALCL. *Experimental Hematology and Oncology* vol. 10 1–12 (2021).

38. Lake, D., Corrêa, S. A. L. & Müller, J. Negative feedback regulation of the ERK1/2 MAPK pathway. *Cell. Mol. Life Sci.* **73**, 4397–4413 (2016).

39. Dougherty, M. K. *et al.* Regulation of Raf-1 by direct feedback phosphorylation. *Mol. Cell* **17**, 215–224 (2005).

40. Eblen, S. T. *et al.* Mitogen-Activated Protein Kinase Feedback Phosphorylation Regulates MEK1 Complex Formation and Activation during Cellular Adhesion. *Mol. Cell. Biol.* **24**, 2308–2317 (2004).

41. Brunet, A., Pagès, G. & Pouysségur, J. Growth factor-stimulated MAP kinase induces rapid retrophosphorylation and inhibition of MAP kinase kinase (MEK1). *FEBS Lett.* **346**, 299–303 (1994).

42. Kidger, A. M. *et al.* Dual-specificity phosphatase 5 controls the localized inhibition, propagation, and transforming potential of ERK signaling. *Proc. Natl. Acad. Sci. U. S. A.* **114**, E317–E326 (2017).

43. Lao, D. H. *et al.* A Src homology 3-binding sequence on the C terminus of sprouty2 is necessary for inhibition of the Ras/ERK pathway downstream of fibroblast growth factor receptor stimulation. *J. Biol. Chem.* **281**, 29993–30000 (2006).

44. Klein, E. A. & Assoian, R. K. Transcriptional regulation of the cyclin D1 gene at a glance. *J. Cell Sci.* **121**, 3853–3857 (2008).

45. Topacio, B. R. *et al.* Cyclin D-Cdk4,6 Drives Cell-Cycle Progression via the Retinoblastoma Protein's C-Terminal Helix. *Mol. Cell* **74**, 758-770.e4 (2019).

46. Bonni, A. *et al.* Cell survival promoted by the Ras-MAPK signaling pathway by transcription-dependent and -independent mechanisms. *Science (80-.).* **286**, 1358–1362 (1999).

47. Enarsson, M., Erlandsson, A., Larsson, H. & Forsberg-Nilsson, K. Extracellular Signal-Regulated Protein Kinase Signaling Is Uncoupled From Initial Differentiation of Central Nervous System Stem Cells to Neurons. (2002).

48. Sanchez-Vega, F. *et al.* Oncogenic Signaling Pathways in The Cancer Genome Atlas. *Cell* **173**, 321-337.e10 (2018).

49. Burotto, M., Chiou, V. L., Lee, J. M. & Kohn, E. C. The MAPK pathway across different malignancies: A new perspective. *Cancer* **120**, 3446–3456 (2014).

50. Bahar, M. E., Kim, H. J. & Kim, D. R. Targeting the RAS/RAF/MAPK pathway for cancer therapy: from mechanism to clinical studies. **8**, 1–38 (2023).

51. Du, Z. & Lovly, C. M. Mechanisms of receptor tyrosine kinase activation in cancer. *Molecular Cancer* vol. 17 (2018).

52. Yaeger, R. & Corcoran, R. B. Targeting alterations in the RAF–MEK pathway. *Cancer Discov.* **9**, 329–341 (2019).

53. Cichowski, K. & Jacks, T. NF1 tumor suppressor gene function: Narrowing the GAP. *Cell* vol. 104 593–604 (2001).

54. Serrano, M., Lin, A. W., McCurrach, M. E., Beach, D. & Lowe, S. W. Oncogenic ras provokes premature cell senescence associated with accumulation of p53 and p16(INK4a). *Cell* **88**, 593–602 (1997).

55. Leung, G. P. *et al.* Hyperactivation of MAPK Signaling Is Deleterious to RAS/RAF-mutant Melanoma. *Mol. Cancer Res.* **17**, 199–211 (2019).

56. Chen, J. Y. *et al.* Multi-range ERK responses shape the proliferative trajectory of single cells following oncogene induction. *Cell Rep.* **42**, 112252 (2023).

57. Jacob, K. *et al.* Genetic aberrations leading to MAPK pathway activation mediate oncogene-induced senescence in sporadic pilocytic astrocytomas. *Clin. Cancer Res.* **17**, 4650–4660 (2011).

58. Coppé, J. P., Desprez, P. Y., Krtolica, A. & Campisi, J. The senescence-associated secretory phenotype: The dark side of tumor suppression. *Annual Review of Pathology: Mechanisms of Disease* vol. 5 99–118 (2010).

59. Liu, X., Ding, J. & Meng, L. Oncogene-induced senescence : a double edged sword in cancer. *Acta Pharmacol. Sin.* **39**, 1553–1558 (2018).

60. Buhl, J. L. *et al.* The Senescence-associated Secretory Phenotype Mediates Oncogene-induced Senescence in Pediatric Pilocytic Astrocytoma. *Clin. Cancer Res.* **25**, 1851–1866 (2019).

61. Sengupta, S. *et al.* A study of histopathological spectrum and expression of Ki-67, TP53 in primary brain tumors of pediatric age group. *Indian J. Med. Paediatr. Oncol.* **33**, 25–31 (2012).

62. Carreno, G., Guiho, R. & Martinez-Barbera, J. P. Cell senescence in neuropathology: A focus on neurodegeneration and tumours. *Neuropathology and Applied Neurobiology* vol. 47 359–378 (2021).

63. Selt, F. *et al.* BH3 mimetics targeting BCL-XL impact the senescent compartment of pilocytic astrocytoma. *Neuro. Oncol.* **25**, 735–747 (2023).

64. Selt, F. *et al.* Establishment and application of a novel patient-derived KIAA1549: BRAF-driven pediatric pilocytic astrocytoma model for preclinical drug testing. *Oncotarget* **8**, 11460–11479 (2017).

65. Karoulia, Z., Gavathiotis, E. & Poulikakos, P. I. New perspectives for targeting RAF kinase in human cancer. *Nature Reviews Cancer* vol. 17 676–691 (2017).

66. Agianian, B. & Gavathiotis, E. Current Insights of BRAF Inhibitors in Cancer. *Journal of Medicinal Chemistry* vol. 61 5775–5793 (2018).

67. Zhang, C. *et al.* RAF inhibitors that evade paradoxical MAPK pathway activation. *Nature* **526**, 583–586 (2015).

68. Sun, Y. *et al.* A brain-penetrant RAF dimer antagonist for the noncanonical BRAF oncoprotein of pediatric low-grade astrocytomas. *Neuro. Oncol.* **19**, 774–785 (2017).

69. Akinleye, A., Furqan, M., Mukhi, N., Ravella, P. & Liu, D. MEK and the inhibitors: From bench to bedside. *Journal of Hematology and Oncology* vol. 6 27 (2013).

70. Wallace, E., Lyssikatos, J., Yeh, T., Winkler, J. & Koch, K. Progress Towards Therapeutic Small Molecule MEK Inhibitors for Use in Cancer Therapy. *Curr. Top. Med. Chem.* **5**, 215–229 (2005).

71. Sammons, R. M., Ghose, R., Tsai, K. Y. & Dalby, K. N. Targeting ERK beyond the boundaries of the kinase active site in melanoma. *Mol. Carcinog.* **58**, 1551–1570 (2019).

72. Kun, E., Tsang, Y. T. M., Ng, C. W., Gershenson, D. M. & Wong, K. K. MEK inhibitor resistance mechanisms and recent developments in combination trials. *Cancer Treatment Reviews* vol. 92 102137 (2021).

73. Thakuri, P. S., Gupta, M., Joshi, R., Singh, S. & Tavana, H. Synergistic Inhibition of Kinase Pathways Overcomes Resistance of Colorectal Cancer Spheroids to Cyclic

Targeted Therapies. *ACS Pharmacol. Transl. Sci.* **2**, 275–284 (2019).

74. Wang, B. *et al.* Targeting mTOR signaling overcomes acquired resistance to combined BRAF and MEK inhibition in BRAF-mutant melanoma. *Oncogene* **40**, 5590–5599 (2021).

75. Grilley-Olson, J. E. *et al.* A phase Ib dose-escalation study of the MEK inhibitor trametinib in combination with the PI3K/mTOR inhibitor GSK2126458 in patients with advanced solid tumors. *Invest. New Drugs* **34**, 740–749 (2016).

76. Goetz, E. M. & Garraway, L. A. Mechanisms of Resistance to Mitogen-Activated Protein Kinase Pathway Inhibition in BRAF-Mutant Melanoma. *Am. Soc. Clin. Oncol. Educ. B.* 680–684 (2012) doi:10.14694/edbook_am.2012.32.189.

77. Milde, T. *et al.* Reimagining pilocytic astrocytomas in the context of pediatric low-grade gliomas. *Neuro. Oncol.* (2021) doi:10.1093/neuonc/noab138.

78. Milde, T. *et al.* Optimizing preclinical pediatric low-grade glioma models for meaningful clinical translation. *Neuro. Oncol.* **25**, 1920–1931 (2023).

79. Raabe, E. H. *et al.* BRAF activation induces transformation and then senescence in human neural stem cells: A pilocytic astrocytoma model. *Clin. Cancer Res.* **17**, 3590–3599 (2011).

80. Kolb, E. A. *et al.* Initial testing (stage 1) of AZD6244 (ARRY-142886) by the pediatric preclinical testing program. *Pediatr. Blood Cancer* **55**, 668–677 (2010).

81. Sigaud, R. *et al.* The first-in-class ERK inhibitor ulixertinib shows promising activity in mitogen-activated protein kinase (MAPK)-driven pediatric low-grade glioma models. *Neuro. Oncol.* (2022) doi:10.1093/neuonc/noac183.

82. Sigaud, R. *et al.* MAPK inhibitor sensitivity scores predict sensitivity driven by the immune infiltration in pediatric low-grade gliomas. *Nat. Commun.* **14**, (2023).

83. Arnold, A. *et al.* Synergistic activity of mTORC1/2 kinase and MEK inhibitors suppresses pediatric low-grade glioma tumorigenicity and vascularity. 1–12 (2020) doi:10.1093/neuonc/noz230.

84. Bid, H. K. *et al.* Development, characterization, and reversal of acquired resistance to the MEK1 inhibitor selumetinib (AZD6244) in an in vivo model of childhood astrocytoma. *Clin. Cancer Res.* **19**, 6716–6729 (2013).

85. Usta, D. *et al.* A cell-based MAPK reporter assay reveals synergistic MAPK pathway activity suppression by MAPK inhibitor combination in BRAF-driven pediatric low-grade glioma cells. *Mol. Cancer Ther.* **19**, 1736–1750 (2020).

86. Rayess, H., Wang, M. B. & Srivatsan, E. S. Cellular senescence and tumor suppressor gene p16. *Int. J. Cancer* **130**, 1715–1725 (2012).

87. Kogiso, M. *et al.* Xenotransplantation of pediatric low grade gliomas confirms the enrichment of BRAF V600E mutation and preservation of CDKN2A deletion in a novel orthotopic xenograft mouse model of progressive pleomorphic xanthoastrocytoma. *Oncotarget* **8**, 87455–87471 (2017).

88. He, C. *et al.* Patient-derived models recapitulate heterogeneity of molecular signatures and drug response in pediatric high-grade glioma. *Nat. Commun.* **12**, (2021).

89. Selt, F. *et al.* Establishment and application of a novel patient-derived KIAA1549: BRAF-driven pediatric pilocytic astrocytoma model for preclinical drug testing. *Oncotarget* **8**, 11460–11479 (2017).

90. Selt, F. *et al.* Generation of patient-derived pediatric pilocytic astrocytoma in-vitro models using SV40 large T: evaluation of a modeling workflow. *J. Neurooncol.* **165**, 467–478 (2023).

91. Ahuja, D., Sáenz-Robles, M. T. & Pipas, J. M. SV40 large T antigen targets multiple cellular pathways to elicit cellular transformation. *Oncogene* vol. 24 7729–7745 (2005).

92. Yuan, M. *et al.* Conditional reprogramming culture conditions facilitate growth of lower-grade glioma models. *Neuro. Oncol.* **23**, 770–782 (2021).

93. Chiacchiarini, M. *et al.* Pediatric low-grade gliomas: molecular characterization of patient-derived cellular models. *Child's Nerv. Syst.* **37**, 771–778 (2021).

94. Rota, C. M. *et al.* Synthetic extracellular matrices and astrocytes provide a supportive microenvironment for the cultivation and investigation of primary pediatric gliomas. *Neuro-Oncology Adv.* **4**, (2022).

95. Chen, R., Keoni, C., Waker, C. A., Lober, R. M. & Gutmann, D. H. KIAA1549-BRAF Expression Establishes a Permissive Tumor Microenvironment Through NFκB-Mediated CCL2 Production. *Neoplasia (United States)* **21**, 52–60 (2019).

96. Kaul, A., Chen, Y. H., Emnett, R. J., Gianino, S. M. & Gutmann, D. H. Conditional KIAA1549: BRAF mice reveal brain region- and cell type-specific effects. *Genesis* vol. 51 708–716 (2013).

97. Anastasaki, C. *et al.* Human induced pluripotent stem cell engineering establishes a humanized mouse platform for pediatric low-grade glioma modeling. *Acta Neuropathol. Commun.* **10**, (2022).

98. Packer, R. J. *et al.* Carboplatin and vincristine chemotherapy for children with newly diagnosed progressive low-grade gliomas. *J. Neurosurg.* **86**, 747–754 (1997).

99. Ater, J. L. *et al.* Randomized study of two chemotherapy regimens for treatment of low-grade glioma in young children: A report from the Children's Oncology Group. *J. Clin. Oncol.* **30**, 2641–2647 (2012).

100. Lassaletta, A. *et al.* Phase II weekly vinblastine for chemotherapy-naïve children with progressive low-grade glioma: A Canadian pediatric brain tumor consortium study. *J. Clin. Oncol.* **34**, 3537–3543 (2016).

101. Barbato, M. I. *et al.* FDA Approval Summary: Dabrafenib in combination with trametinib for BRAF V600E mutation-positive low-grade glioma. *Clin. Cancer Res.* **30**, OF1–OF6 (2023).

102. Cherlow, J. M. *et al.* Conformal Radiation Therapy for Pediatric Patients with Low-Grade Glioma: Results from the Children's Oncology Group Phase 2 Study ACNS0221. *Int. J. Radiat. Oncol. Biol. Phys.* **103**, 861–868 (2019).

103. Greenberger, B. A. *et al.* Clinical outcomes and late endocrine, neurocognitive, and visual profiles of proton radiation for pediatric low-grade gliomas. *Int. J. Radiat. Oncol. Biol. Phys.* **89**, 1060–1068 (2014).

104. Merchant, T. E., Conklin, H. M., Wu, S., Lustig, R. H. & Xiong, X. Late effects of conformal radiation therapy for pediatric patients with low-grade glioma: Prospective evaluation of cognitive, endocrine, and hearing deficits. *J. Clin. Oncol.* **27**, 3691–3697 (2009).

105. Sait, S. F., Giantini-Larsen, A. M., Tringale, K. R., Souweidane, M. M. & Karajannis, M. A. Treatment of Pediatric Low-Grade Gliomas. *Current Neurology and Neuroscience Reports* vol. 23 185–199 (2023).

106. Bitterman, D. S. *et al.* Revisiting the role of radiation therapy for pediatric low-grade glioma. *J. Clin. Oncol.* **37**, 3335–3339 (2019).

107. Nobre, L. *et al.* Outcomes of BRAF V600E Pediatric Gliomas Treated With Targeted BRAF Inhibition. *JCO Precis. Oncol.* 561–571 (2020) doi:10.1200/po.19.00298.

108. Hargrave, D. R. *et al.* Efficacy and Safety of Dabrafenib in Pediatric Patients with BRAF V600 Mutation-Positive Relapsed or Refractory Low-Grade Glioma: Results from a Phase I/IIa Study. *Clin. Cancer Res.* **25**, 7303–7311 (2019).

109. Bouffet, E. *et al.* Dabrafenib plus Trametinib in Pediatric Glioma with BRAF V600 Mutations. *N. Engl. J. Med.* **389**, 1108–1120 (2023).

110. Bergqvist, C. & Wolkenstein, P. MEK inhibitors in RASopathies. *Current Opinion in Oncology* vol. 33 110–119 (2021).

111. Fangusaro, J. *et al.* A phase II trial of selumetinib in children with recurrent optic pathway and hypothalamic low-grade glioma without NF1: a Pediatric Brain Tumor Consortium study. *Neuro. Oncol.* **23**, 1777–1788 (2021).

112. Fangusaro, J. *et al.* Selumetinib in paediatric patients with BRAF-aberrant or neurofibromatosis type 1-associated recurrent, refractory, or progressive low-grade glioma: a multicentre, phase 2 trial. *Lancet Oncol.* **20**, 1011–1022 (2019).

113. Ullrich, N. J. *et al.* A phase II study of continuous oral mTOR inhibitor everolimus for recurrent, radiographic-progressive neurofibromatosis type 1–associated pediatric low-grade glioma: a Neurofibromatosis Clinical Trials Consortium study. *Neuro. Oncol.* **22**, 1527–1535 (2020).

114. Cacchione, A. *et al.* Upfront treatment with mTOR inhibitor everolimus in pediatric low-grade gliomas: A single-center experience. *Int. J. Cancer* **148**, 2522–2534 (2021).

115. Haas-Kogan, D. A. *et al.* Everolimus for Children With Recurrent or Progressive Low-Grade Glioma: Results From the Phase II PNOC001 Trial. *J. Clin. Oncol.* (2023) doi:10.1200/jco.23.01838.

116. Morin, E. *et al.* LGG-48. The influence of different FGFR1 alterations on pediatric low-grade glioma tumor biology and targeted therapy response. *Neuro. Oncol.* **24**, i99–i99 (2022).

117. Tsai, J. W. *et al.* Integrated response analysis of pediatric low-grade gliomas during and after targeted therapy treatment. *Neuro-Oncology Adv.* **5**, (2023).

118. Selt, F. *et al.* Response to trametinib treatment in progressive pediatric low-grade glioma patients. *J. Neurooncol.* **149**, 499–510 (2020).

119. Mastri, M. *et al.* A Transient Pseudosenescent Secretome Promotes Tumor Growth after Antiangiogenic Therapy Withdrawal. *Cell Rep.* **25**, 3706-3720.e8 (2018).

120. Pupo, E. *et al.* Rebound effects caused by withdrawal of MET Kinase inhibitor are quenched by a MET Therapeutic antibody. *Cancer Res.* **76**, 5019–5029 (2016).

121. Faes, S., Santoro, T., Troquier, L., De Souza Silva, O. & Dormond, O. Rebound pathway overactivation by cancer cells following discontinuation of PI3K or mTOR inhibition promotes cancer cell growth. *Biochem. Biophys. Res. Commun.* **513**, 546–552 (2019).

122. Rasmussen, L. A. *et al.* Time from incident primary cancer until recurrence or second primary cancer: Risk factors and impact in general practice. *Eur. J. Cancer Care (Engl).* **28**, e13123 (2019).

123. Reitman, Z. J. *et al.* Mitogenic and progenitor gene programmes in single pilocytic

astrocytoma cells. *Nat. Commun.* **10**, (2019).

124. Simmons, G. W. *et al.* Neurofibromatosis-1 heterozygosity increases microglia in a spatially and temporally restricted pattern relevant to mouse optic glioma formation and growth. *J. Neuropathol. Exp. Neurol.* **70**, 51–62 (2011).

125. Gutmann, D. H. *et al.* Somatic neurofibromatosis type 1 (NF1) inactivation characterizes NF1-associated pilocytic astrocytoma. *Genome Res.* **23**, 431–439 (2013).

126. Robinson, M. H. *et al.* Subtype and grade-dependent spatial heterogeneity of T-cell infiltration in pediatric glioma. *J. Immunother. Cancer* **8**, (2020).

127. Pong, W. W., Higer, S. B., Gianino, S. M., Emnett, R. J. & Gutmann, D. H. Reduced microglial CX3CR1 expression delays neurofibromatosis-1 glioma formation. *Ann. Neurol.* **73**, 303–308 (2013).

128. Daginakatte, G. C., Gianino, S. M., Zhao, N. W., Parsadanian, A. S. & Gutmann, D. H. Increased c-Jun-NH2-kinase signaling in neurofibromatosis-1 heterozygous microglia drives microglia activation and promotes optic glioma proliferation. *Cancer Res.* **68**, 10358–10366 (2008).

129. Guo, X. *et al.* Midkine activation of CD8+ T cells establishes a neuron–immune–cancer axis responsible for low-grade glioma growth. *Nat. Commun.* **11**, 1–15 (2020).

130. Faget, D. V., Ren, Q. & Stewart, S. A. Unmasking senescence: context-dependent effects of SASP in cancer. *Nature Reviews Cancer* vol. 19 439–453 (2019).

131. Iannello, A., Thompson, T. W., Ardolino, M., Lowe, S. W. & Raulet, D. H. p53-dependent chemokine production by senescent tumor cells supports NKG2D-dependent tumor elimination by natural killer cells. *J. Exp. Med.* **210**, 2057–2069 (2013).

132. Kang, T. W. *et al.* Senescence surveillance of pre-malignant hepatocytes limits liver cancer development. *Nature* **479**, 547–551 (2011).

133. Ruhland, M. K. *et al.* Stromal senescence establishes an immunosuppressive microenvironment that drives tumorigenesis. *Nat. Commun.* **7**, 1–18 (2016).

134. Eggert, T. *et al.* Distinct Functions of Senescence-Associated Immune Responses in Liver Tumor Surveillance and Tumor Progression. *Cancer Cell* **30**, 533–547 (2016).

135. Liu, C. *et al.* Cytokines: From Clinical Significance to Quantification. *Advanced Science* vol. 8 2004433 (2021).

136. Griffith, J. W., Sokol, C. L. & Luster, A. D. Chemokines and chemokine receptors: Positioning cells for host defense and immunity. *Annual Review of Immunology* vol. 32 659–702 (2014).

137. Hughes, C. E. & Nibbs, R. J. B. A guide to chemokines and their receptors. *FEBS J.* **285**, 2944–2971 (2018).

138. Nolte, E. *et al.* Abstract 4725: Elevated co-expression of CCL2 and CX3CL1 is associated with apoptosis and good prognosis in soft tissue sarcoma patients. *Cancer Res.* **74**, 4725–4725 (2014).

139. Nakayama, A. *et al.* Suppression of CCL2 angiocrine function by adrenomedullin promotes tumor growth. *J. Exp. Med.* **220**, (2023).

140. Tang, C. H. & Tsai, C. C. CCL2 increases MMP-9 expression and cell motility in human chondrosarcoma cells via the Ras/Raf/MEK/ERK/NF-κB signaling pathway. *Biochem. Pharmacol.* **83**, 335–344 (2012).

141. Dagouassat, M. *et al.* Monocyte chemoattractant protein-1 (MCP-1)/CCL2 secreted by

hepatic myofibroblasts promotes migration and invasion of human hepatoma cells. *Int. J. Cancer* **126**, 1095–1108 (2010).

142. Mizutani, K. *et al.* The chemokine CCL2 increases prostate tumor growth and bone metastasis through macrophage and osteoclast recruitment. *Neoplasia* **11**, 1235–1242 (2009).

143. Koide, N., Nishio, A., Sato, T., Sugiyama, A. & Miyagawa, S. I. Significance of macrophage chemoattractant protein-1 expression and macrophage infiltration in squamous cell carcinoma of the esophagus. *Am. J. Gastroenterol.* **99**, 1667–1674 (2004).

144. Shono, K. *et al.* Downregulation of the CCL2/CCR2 and CXCL10/CXCR3 axes contributes to antitumor effects in a mouse model of malignant glioma. *Sci. Rep.* **10**, 1–10 (2020).

145. Maru, S. V. *et al.* Chemokine production and chemokine receptor expression by human glioma cells: Role of CXCL10 in tumour cell proliferation. *J. Neuroimmunol.* **199**, 35–45 (2008).

146. Datta, D. *et al.* Ras-induced modulation of CXCL10 and its receptor splice variant CXCR3-B in MDA-MB-435 and MCF-7 cells: Relevance for the development of human breast cancer. *Cancer Res.* **66**, 9509–9518 (2006).

147. Lu, X., Jiang, X., Liu, R. & Zhang, S. The enhanced anti-angiogenic and antitumor effects of combining flk1-based DNA vaccine and IP-10. *Vaccine* **26**, 5352–5357 (2008).

148. Fujita, M. *et al.* Effective immunotherapy against murine gliomas using type 1 polarizing dendritic cells-significant roles of CXCL10. *Cancer Res.* **69**, 1587–1595 (2009).

149. Jiang, X. bing, Lu, X. ling, Hu, P. & Liu, R. en. Improved therapeutic efficacy using vaccination with glioma lysate-pulsed dendritic cells combined with IP-10 in murine glioma. *Vaccine* **27**, 6210–6216 (2009).

150. Reschke, R. *et al.* Immune cell and tumor cell-derived CXCL10 is indicative of immunotherapy response in metastatic melanoma. *J. Immunother. Cancer* **9**, (2021).

151. Spranger, S., Dai, D., Horton, B. & Gajewski, T. F. Tumor-Residing Batf3 Dendritic Cells Are Required for Effector T Cell Trafficking and Adoptive T Cell Therapy. *Cancer Cell* **31**, 711-723.e4 (2017).

152. Zhang, M. *et al.* CCL7 recruits cDC1 to promote antitumor immunity and facilitate checkpoint immunotherapy to non-small cell lung cancer. *Nat. Commun.* **11**, 1–17 (2020).

153. Wetzel, K. *et al.* Transduction of human MCP-3 by a parvoviral vector induces leukocyte infiltration and reduces growth of human cervical carcinoma cell xenografts. *J. Gene Med.* **3**, 326–337 (2001).

154. Wyler, L. *et al.* Brain metastasis in renal cancer patients: Metastatic pattern, tumour-associated macrophages and chemokine/chemoreceptor expression. *Br. J. Cancer* **110**, 686–694 (2014).

155. Lee, Y. S. *et al.* Crosstalk between CCL7 and CCR3 promotes metastasis of colon cancer cells via ERK-JNK signaling pathways. *Oncotarget* **7**, 36842–36853 (2016).

156. Batool, A., Wang, Y. Q., Hao, X. X., Chen, S. R. & Liu, Y. X. A miR-125b/CSF1-CX3CL1/tumor-associated macrophage recruitment axis controls testicular germ cell tumor growth. *Cell Death Dis.* **9**, 1–14 (2018).

157. Reed, J. R. *et al.* Fibroblast Growth Factor Receptor 1 Activation in Mammary Tumor

Cells Promotes Macrophage Recruitment in a CX3CL1-Dependent Manner. *PLoS One* **7**, (2012).

158. Ishida, Y. *et al.* Pivotal Involvement of the CX3CL1-CX3CR1 Axis for the Recruitment of M2 Tumor-Associated Macrophages in Skin Carcinogenesis. *J. Invest. Dermatol.* **140**, 1951-1961.e6 (2020).

159. Tardáguila, M. *et al.* CX3CL1 promotes breast cancer via transactivation of the EGF pathway. *Cancer Res.* **73**, 4461–4473 (2013).

160. Tang, J. *et al.* CX3CL1 increases invasiveness and metastasis by promoting epithelial-to-mesenchymal transition through the TACE/TGF-/EGFR pathway in hypoxic androgen independent prostate cancer cells. *Oncol. Rep.* **35**, 1153–1162 (2016).

161. Cohen, C. *et al.* CX3CL1 as potential immunotherapeutic tool for bone metastases in lung cancer: A preclinical study. *Adv. Cancer Biol. - Metastasis* **6**, 100069 (2022).

162. Gong, Q. *et al.* CX3CL1 promotes cell sensitivity to ferroptosis and is associated with the tumor microenvironment in clear cell renal cell carcinoma. *BMC Cancer* **22**, 1184 (2022).

163. Reisinger, E. *et al.* OTP: An automatized system for managing and processing NGS data. *Journal of Biotechnology* vol. 261 53–62 (2017).

164. Cox, J. & Mann, M. MaxQuant enables high peptide identification rates, individualized p.p.b.-range mass accuracies and proteome-wide protein quantification. *Nat. Biotechnol.* **26**, 1367–1372 (2008).

165. Zhang, X. *et al.* Proteome-wide identification of ubiquitin interactions using UbIA-MS. *Nat. Protoc.* **13**, 530–550 (2018).

166. Kim, H. J., Kim, T., Xiao, D. & Yang, P. Protocol for the processing and downstream analysis of phosphoproteomic data with PhosR. *STAR Protoc.* **2**, 100585 (2021).

167. Kim, H. J. *et al.* PhosR enables processing and functional analysis of phosphoproteomic data. *Cell Rep.* **34**, 108771 (2021).

168. Molania, R., Gagnon-Bartsch, J. A., Dobrovic, A. & Speed, T. P. A new normalization for Nanostring nCounter gene expression data. *Nucleic Acids Res.* **47**, 6073–6083 (2019).

169. R Core Team. R: A Language and Environment for Statistical Computing. (2022).

170. Wickham, H. *ggplot2: Elegant Graphics for Data Analysis*. (Springer-Verlag New York, 2016).

171. Vu, V. Q. & Friendly, M. ggbiplot: A Grammar of Graphics Implementation of Biplots. (2023).

172. Wagle, M.-C. *et al.* A transcriptional MAPK Pathway Activity Score (MPAS) is a clinically relevant biomarker in multiple cancer types. *npj Precis. Oncol.* **2**, 7 (2018).

173. Love, M. I., Huber, W. & Anders, S. Moderated estimation of fold change and dispersion for RNA-seq data with DESeq2. *Genome Biol.* **15**, 550 (2014).

174. Reich, M. *et al.* GenePattern 2.0 [2]. *Nature Genetics* vol. 38 500–501 (2006).

175. Genolini, C., Alacoque, X., Sentenac, M. & Arnaud, C. {kml} and {kml3d}: {R} Packages to Cluster Longitudinal Data. *J. Stat. Softw.* **65**, 1–34 (2015).

176. Caliński, T. & Harabasz, J. A Dendrite Method Foe Cluster Analysis. *Commun. Stat.* **3**, 1–27 (1974).

177. Bindea, G. *et al.* ClueGO: A Cytoscape plug-in to decipher functionally grouped gene ontology and pathway annotation networks. *Bioinformatics* **25**, 1091–1093 (2009).

178. Shannon, P. *et al.* Cytoscape: A software Environment for integrated models of biomolecular interaction networks. *Genome Res.* **13**, 2498–2504 (2003).

179. Barbie, D. A. *et al.* Systematic RNA interference reveals that oncogenic KRAS-driven cancers require TBK1. *Nature* **462**, 108–112 (2009).

180. Gu, Z. Complex heatmap visualization. *iMeta* **1**, e43 (2022).

181. Gu, Z., Eils, R. & Schlesner, M. Complex heatmaps reveal patterns and correlations in multidimensional genomic data. *Bioinformatics* **32**, 2847–2849 (2016).

182. Maxwell, M. J. *et al.* Unbiased proteomic and phosphoproteomic analysis identifies response signatures and novel susceptibilities after combined MEK and mTOR inhibition in BRAFV600E Mutant Glioma. *Mol. Cell. Proteomics* **20**, (2021).

183. Krug, K. *et al.* A Curated Resource for Phosphosite-specific Signature Analysis. *Mol. Cell. Proteomics* **18**, 576–593 (2019).

184. Wiredja, D. D., Koyutürk, M. & Chance, M. R. The KSEA App: a web-based tool for kinase activity inference from quantitative phosphoproteomics. *Bioinformatics* **33**, 3489–3491 (2017).

185. Horn, H. *et al.* KinomeXplorer: An integrated platform for kinome biology studies. *Nature Methods* vol. 11 603–604 (2014).

186. Hornbeck, P. V. *et al.* PhosphoSitePlus, 2014: Mutations, PTMs and recalibrations. *Nucleic Acids Res.* **43**, D512–D520 (2015).

187. Casado, P. *et al.* Kinase-substrate enrichment analysis provides insights into the heterogeneity of signaling pathway activation in leukemia cells. *Science Signaling* vol. 6 (2013).

188. Jamaladdin, N. *et al.* Key Pharmacokinetic Parameters of 74 Pediatric Anticancer Drugs Providing Assistance in Preclinical Studies. *Clin. Pharmacol. Ther.* **114**, 904–913 (2023).

189. van de Velde, M. E. *et al.* Population pharmacokinetics of vincristine related to infusion duration and peripheral neuropathy in pediatric oncology patients. *Cancers (Basel).* **12**, 1–15 (2020).

190. Riccardi, R. *et al.* Clinical pharmacokinetics of carboplatin in children. *Cancer Chemother. Pharmacol.* **33**, 477–483 (1994).

191. Tewari, M. *et al.* Yama/CPP32β, a mammalian homolog of CED-3, is a CrmA-inhibitable protease that cleaves the death substrate poly(ADP-ribose) polymerase. *Cell* **81**, 801–809 (1995).

192. Plesca, D., Mazumder, S. & Almasan, A. Chapter 6 DNA Damage Response and Apoptosis. *Methods in Enzymology* vol. 446 107–122 (2008).

193. Pratilas, C. A. *et al.* V600EBRAF is associated with disabled feedback inhibition of RAF-MEK signaling and elevated transcriptional output of the pathway. *Proc. Natl. Acad. Sci. U. S. A.* **106**, 4519–4524 (2009).

194. Liu, T., Zhang, L., Joo, D. & Sun, S. C. NF-κB signaling in inflammation. *Signal Transduction and Targeted Therapy* vol. 2 1–9 (2017).

195. Ghosh, S. & Karin, M. Missing pieces in the NF-κB puzzle. *Cell* vol. 109 S81–S96 (2002).

196. Dan, H. C. *et al.* Akt-dependent regulation of NF-κB is controlled by mTOR and Raptor in association with IKK. *Genes Dev.* **22**, 1490–1500 (2008).

197. Manning, B. D. & Toker, A. AKT/PKB Signaling: Navigating the Network. *Cell* **169**, 381–405 (2017).

198. Samuels, Y. *et al.* High Frequency of Mutations of the PIK3CA Gene in Human Cancers. *Science (80-.).* **304**, 554 (2004).

199. He, Y. *et al.* Targeting PI3K/Akt signal transduction for cancer therapy. *Signal Transduction and Targeted Therapy* vol. 6 1–17 (2021).

200. Corrales, E. *et al.* PI3K/AKT signaling allows for MAPK/ERK pathway independency mediating dedifferentiation-driven treatment resistance in melanoma. *Cell Commun. Signal.* **20**, 187 (2022).

201. Gopal, Y. N. V. *et al.* Basal and treatment-induced activation of AKT mediates resistance to cell death by AZD6244 (ARRY-142886) in Braf-mutant human cutaneous melanoma cells. *Cancer Res.* **70**, 8736–8747 (2010).

202. Cao, Z. *et al.* AKT and ERK dual inhibitors: The way forward? *Cancer Letters* vol. 459 30–40 (2019).

203. Shao, X. *et al.* CellTalkDB: a manually curated database of ligand–receptor interactions in humans and mice. *Brief. Bioinform.* **22**, (2021).

204. Ito, S., Sawada, M., Haneda, M., Ishida, Y. & Isobe, K. ichi. Amyloid-β peptides induce several chemokine mRNA expressions in the primary microglia and Ra2 cell line via the PI3K/Akt and/or ERK pathway. *Neurosci. Res.* **56**, 294–299 (2006).

205. Arimura, Y. *et al.* Akt Is a Neutral Amplifier for Th Cell Differentiation. *J. Biol. Chem.* **279**, 11408–11416 (2004).

206. Qian, Y., Ding, P., Xu, J., Nie, X. & Lu, B. CCL2 activates AKT signaling to promote glycolysis and chemoresistance in glioma cells. *Cell Biol. Int.* **46**, 819–828 (2022).

207. Fang, Y. *et al.* Chemokine CXCL10 regulates pain behaviors via PI3K-AKT signaling pathway in mice. *Neuropeptides* **93**, 102243 (2022).

208. Wang, H. *et al.* Fractalkine/CX3CR1 induces apoptosis resistance and proliferation through the activation of the AKT/NF-κB cascade in pancreatic cancer cells. *Cell Biochem. Funct.* **35**, 315–326 (2017).

209. Turke, A. B. *et al.* MEK inhibition leads to PI3K/AKT activation by relieving a negative feedback on ERBB receptors. *Cancer Res.* **72**, 3228–3237 (2012).

210. Grossauer, S. *et al.* Concurrent MEK targeted therapy prevents MAPK pathway reactivation during BRAFV600E targeted inhibition in a novel syngeneic murine glioma model. *Oncotarget* **7**, 75839–75853 (2016).

211. Obenauf, A. C. *et al.* Therapy-induced tumour secretomes promote resistance and tumour progression. *Nature* **520**, 368–372 (2015).

212. Shi, H. *et al.* Acquired resistance and clonal evolution in melanoma during BRAF inhibitor therapy. *Cancer Discov.* **4**, 80–93 (2014).

213. Shi, H. *et al.* A novel AKT1 mutant amplifies an adaptive melanoma response to BRAF inhibition. *Cancer Discov.* **4**, 69–79 (2014).

214. Shi, H., Kong, X., Ribas, A. & Lo, R. S. Combinatorial treatments that overcome PDGFRβ-driven resistance of melanoma cells to V600EB-RAF inhibition. *Cancer Res.* **71**, 5067–5074 (2011).

215. Isakoff, S. J. *et al.* Antitumor activity of ipatasertib combined with chemotherapy: results from a phase Ib study in solid tumors. *Ann. Oncol.* **31**, 626–633 (2020).

216. Bose, S. *et al.* Effect of CCL2 on BV2 microglial cell migration: Involvement of probable signaling pathways. *Cytokine* **81**, 39–49 (2016).

217. He, M. *et al.* Astrocyte-derived CCL2 is associated with m1 activation and recruitment of cultured microglial cells. *Cell. Physiol. Biochem.* **38**, 859–870 (2016).

218. Hulshof, S. *et al.* CX3CL1 and CX3CR1 Expression in Human Brain Tissue: Noninflammatory Control versus Multiple Sclerosis. *J. Neuropathol. Exp. Neurol.* **62**, 899–907 (2003).

219. Held-Feindt, J. *et al.* CX3CR1 promotes recruitment of human glioma-infiltrating microglia/macrophages (GIMs). *Exp. Cell Res.* **316**, 1553–1566 (2010).

220. Maciejewski-Lenoir, D., Chen, S., Feng, L., Maki, R. & Bacon, K. B. Characterization of Fractalkine in Rat Brain Cells: Migratory and Activation Signals for CX3CR-1-Expressing Microglia. *J. Immunol.* **163**, 1628–1635 (1999).

221. Giacinti, C. & Giordano, A. RB and cell cycle progression. *Oncogene 2006 2538* **25**, 5220–5227 (2006).

222. McHugh, D. & Gil, J. Senescence and aging: Causes, consequences, and therapeutic avenues. *Journal of Cell Biology* vol. 217 65–77 (2018).

223. Huang, W., Hickson, L. T. J., Eirin, A., Kirkland, J. L. & Lerman, L. O. Cellular senescence: the good, the bad and the unknown. *Nat. Rev. Nephrol. 2022 1810* **18**, 611–627 (2022).

224. Soto-Gamez, A., Quax, W. J. & Demaria, M. Regulation of Survival Networks in Senescent Cells: From Mechanisms to Interventions. *Journal of Molecular Biology* vol. 431 2629–2643 (2019).

225. Montagut, C. *et al.* Elevated CRAF as a potential mechanism of acquired resistance to BRAF inhibition in melanoma. *Cancer Res.* **68**, 4853–4861 (2008).

226. Rupa, D. S., Schuler, M. & Eastmond, D. A. Detection of hyperdiploidy and breakage affecting the 1cen-1q12 region of cultured interphase human lymphocytes treated with various genotoxic agents. *Environ. Mol. Mutagen.* **29**, 161–167 (1997).

227. Filippi-Chiela, E. C., Vargas, J. E., Bueno e Silva, M. M., Thomé, M. P. & Lenz, G. Vincristine promotes differential levels of apoptosis, mitotic catastrophe, and senescence depending on the genetic background of glioblastoma cells. *Toxicol. Vitr.* **85**, 105472 (2022).

228. Rabik, C. A. & Dolan, M. E. Molecular mechanisms of resistance and toxicity associated with platinating agents. *Cancer Treatment Reviews* vol. 33 9–23 (2007).

229. Harmon, B. V., Takano, Y. S., Winterford, C. M. & Potten, C. S. Cell death induced by vincristine in the intestinal crypts of mice and in a human Burkitt's lymphoma cell line. *Cell Prolif.* **25**, 523–536 (1992).

230. Altintas, D. M. *et al.* An mTOR feedback loop mediates the 'flare' ('rebound') response to MET tyrosine kinase inhibition. *Sci. Rep.* **13**, 1–10 (2023).

231. Hong, A. *et al.* Exploiting drug addiction mechanisms to select against mapki-resistant melanoma. *Cancer Discov.* **8**, 74–93 (2018).

232. Kong, X. *et al.* Cancer drug addiction is relayed by an ERK2-dependent phenotype switch. *Nature* **550**, 270–274 (2017).

233. Moriceau, G. *et al.* Tunable-combinatorial Mechanisms of Acquired Resistance Limit the Efficacy of BRAF/MEK Co-targeting but Result in Melanoma Drug Addiction. *Cancer Cell* **27**, 240–256 (2015).

234. Chiou, L. W., Chan, C. H., Jhuang, Y. L., Yang, C. Y. & Jeng, Y. M. DNA replication stress and mitotic catastrophe mediate sotorasib addiction in KRASG12C-mutant cancer. *J. Biomed. Sci.* **30**, 50 (2023).

235. Farnsworth, D. A. *et al.* MEK inhibitor resistance in lung adenocarcinoma is associated with addiction to sustained ERK suppression. *npj Precis. Oncol.* **6**, 1–15 (2022).

236. Pratilas, C. A. *et al.* V600EBRAF is associated with disabled feedback inhibition of RAF-MEK signaling and elevated transcriptional output of the pathway. *Proc. Natl. Acad. Sci. U. S. A.* **106**, 4519–4524 (2009).

237. Ito, T. *et al.* Paralog knockout profiling identifies DUSP4 and DUSP6 as a digenic dependence in MAPK pathway-driven cancers. *Nat. Genet.* **53**, 1664–1672 (2021).

238. Ecker, V. *et al.* Negative feedback regulation of MAPK signaling is an important driver of chronic lymphocytic leukemia progression. *Cell Rep.* **42**, 113017 (2023).

239. Vainonen, J. P., Momeny, M. & Westermarck, J. Druggable cancer phosphatases. *Sci. Transl. Med.* **13**, (2021).

240. Köhn, M. Turn and Face the Strange: § A New View on Phosphatases. *ACS Cent. Sci.* **6**, 467–477 (2020).

241. Elhassan, R. M., Hou, X. & Fang, H. Recent advances in the development of allosteric protein tyrosine phosphatase inhibitors for drug discovery. *Medicinal Research Reviews* vol. 42 1064–1110 (2022).

242. Prahallad, A. *et al.* Unresponsiveness of colon cancer to BRAF(V600E) inhibition through feedback activation of EGFR. *Nature* **483**, 100–104 (2012).

243. Agazie, Y. M. & Hayman, M. J. Molecular Mechanism for a Role of SHP2 in Epidermal Growth Factor Receptor Signaling. *Mol. Cell. Biol.* **23**, 7875–7886 (2003).

244. Montagner, A. *et al.* A novel role for Gab1 and SHP2 in epidermal growth factor-induced Ras activation. *J. Biol. Chem.* **280**, 5350–5360 (2005).

245. Pacold, M. E. *et al.* Crystal structure and functional analysis of Ras binding to its effector phosphoinositide 3-kinase γ. *Cell* **103**, 931–944 (2000).

246. Steinbrunn, T. *et al.* Combined targeting of MEK/MAPK and PI3K/Akt signalling in multiple myeloma. *Br. J. Haematol.* **159**, 430–440 (2012).

247. Schreck, K. C., Allen, A. N., Wang, J. & Pratilas, C. A. Combination MEK and mTOR inhibitor therapy is active in models of glioblastoma. *Neuro-Oncology Adv.* **2**, (2020).

248. Schram, A. M. *et al.* A phase Ib dose-escalation and expansion study of the oral MEK inhibitor pimasertib and PI3K/MTOR inhibitor voxtalisib in patients with advanced solid tumours. *Br. J. Cancer* **119**, 1471–1476 (2018).

249. Mita, M. *et al.* Phase I trial of MEK 1/2 inhibitor pimasertib combined with mTOR inhibitor temsirolimus in patients with advanced solid tumors. *Invest. New Drugs* **35**, 616–626 (2017).

250. Tolcher, A. W. *et al.* A phase IB trial of the oral MEK inhibitor trametinib (GSK1120212) in combination with everolimus in patients with advanced solid tumors. *Ann. Oncol.* **26**, 58–64 (2015).

251. Arnold, A. *et al.* Synergistic activity of mTORC1/2 kinase and MEK inhibitors suppresses

pediatric low-grade glioma tumorigenicity and vascularity. *Neuro. Oncol.* (2019) doi:10.1093/neuonc/noz230.

252. Zhao, L., Au, J. L.-S. & Wientjes, M. G. Method to Assess Interactivity of Drugs with Nonparallel Concentration Effect Relationships. *Curr. Cancer Drug Targets* **17**, (2017).

253. Kitaura, J. *et al.* Akt-dependent cytokine production in mast cells. *J. Exp. Med.* **192**, 729–739 (2000).

254. Strassheim, D. *et al.* Phosphoinositide 3-Kinase and Akt Occupy Central Roles in Inflammatory Responses of Toll-Like Receptor 2-Stimulated Neutrophils. *J. Immunol.* **172**, 5727–5733 (2004).

255. Qin, H. *et al.* Inhibition of the JAK/STAT pathway protects against α-synuclein-induced neuroinflammation and dopaminergic neurodegeneration. *J. Neurosci.* **36**, 5144–5159 (2016).

256. Nurieva, R. *et al.* Essential autocrine regulation by IL-21 in the generation of inflammatory T cells. *Nature* **448**, 480–483 (2007).

257. Zhou, L. *et al.* IL-6 programs TH-17 cell differentiation by promoting sequential engagement of the IL-21 and IL-23 pathways. *Nat. Immunol.* **8**, 967–974 (2007).

258. Schmitt, E. *et al.* IL-9 production of naive CD4+ T cells depends on IL-2, is synergistically enhanced by a combination of TGF-beta and IL-4, and is inhibited by IFN-gamma. *J. Immunol.* (1994).

259. Veldhoen, M. *et al.* Transforming growth factor-β 'reprograms' the differentiation of T helper 2 cells and promotes an interleukin 9-producing subset. *Nat. Immunol.* **9**, 1341–1346 (2008).

260. Xu, J. *et al.* The Cytokine TGF-β Induces Interleukin-31 Expression from Dermal Dendritic Cells to Activate Sensory Neurons and Stimulate Wound Itching. *Immunity* **53**, 371-383.e5 (2020).

261. Richmond, A. NF-κB, chemokine gene transcription and tumour growth. *Nature Reviews Immunology* vol. 2 664–674 (2002).

262. Chandrasekar, B. *et al.* Fractalkine (CX3CL1) stimulated by nuclear factor κB (NF-κB)-dependent inflammatory signals induces aortic smooth muscle cell proliferation through an autocrine pathway. *Biochem. J.* **373**, 547–558 (2003).

263. Yeruva, S., Ramadori, G. & Raddatz, D. NF-κB-dependent synergistic regulation of CXCL10 gene expression by IL-1β and IFN-γ in human intestinal epithelial cell lines. *Int. J. Colorectal Dis.* **23**, 305–317 (2008).

264. Deng, X. *et al.* Transcriptional regulation of increased CCL2 expression in pulmonary fibrosis involves nuclear factor-κB and activator protein-1. *Int. J. Biochem. Cell Biol.* **45**, 1366–1376 (2013).

265. Khorooshi, R., Babcock, A. A. & Owens, T. NF-κB-Driven STAT2 and CCL2 Expression in Astrocytes in Response to Brain Injury. *J. Immunol.* **181**, 7284–7291 (2008).

266. Thompson, W. L. & Van Eldik, L. J. Inflammatory cytokines stimulate the chemokines CCL2/MCP-1 and CCL7/MCP-7 through NFκB and MAPK dependent pathways in rat astrocytes. *Brain Res.* **1287**, 47–57 (2009).

267. Turner, M. D., Nedjai, B., Hurst, T. & Pennington, D. J. Cytokines and chemokines: At the crossroads of cell signalling and inflammatory disease. *Biochimica et Biophysica Acta - Molecular Cell Research* vol. 1843 2563–2582 (2014).

268. Carter, A. B., Monick, M. M. & Hunninghake, G. W. Both Erk and p38 Kinases Are Necessary for Cytokine Gene Transcription. *Am. J. Respir. Cell Mol. Biol.* **20**, 751–758 (1999).

269. Hyo, W. J., Yoo, S. C., Yoon, S. K. & Park, Y. K. Celastrol inhibits production of nitric oxide and proinflammatory cytokines through MAPK signal transduction and NF-κB in LPS-stimulated BV-2 microglial cells. *Exp. Mol. Med.* **39**, 715–721 (2007).

270. Hajek, E. *et al.* BRAF inhibitors stimulate inflammasome activation and interleukin 1 beta production in dendritic cells. *Oncotarget* **9**, 28294–28308 (2018).

271. Pastore, S. *et al.* ERK1/2 Regulates Epidermal Chemokine Expression and Skin Inflammation. *J. Immunol.* **174**, 5047–5056 (2005).

272. Hauser, A. S., Attwood, M. M., Rask-Andersen, M., Schiöth, H. B. & Gloriam, D. E. Trends in GPCR drug discovery: New agents, targets and indications. *Nat. Rev. Drug Discov.* **16**, 829–842 (2017).

273. Duitman, E. H., Orinska, Z. & Bulfone-Paus, S. Mechanisms of cytokine secretion: A portfolio of distinct pathways allows flexibility in cytokine activity. *European Journal of Cell Biology* vol. 90 476–483 (2011).

274. Essandoh, K. *et al.* Blockade of exosome generation with GW4869 dampens the sepsis-induced inflammation and cardiac dysfunction. *Biochim. Biophys. Acta - Mol. Basis Dis.* **1852**, 2362–2371 (2015).

275. Kornhuber, J. *et al.* Identification of new functional inhibitors of acid sphingomyelinase using a structure-property-activity relation model. *J. Med. Chem.* **51**, 219–237 (2008).

276. Menck, K. *et al.* Neutral sphingomyelinases control extracellular vesicles budding from the plasma membrane. *J. Extracell. Vesicles* **6**, (2017).

277. Cross, A. K. & Woodroofe, M. N. Chemokines induce migration and changes in actin polymerization in adult rat brain microglia and a human fetal microglial cell line in vitro. *J. Neurosci. Res.* **55**, 17–23 (1999).

278. Clarner, T. *et al.* CXCL10 Triggers Early Microglial Activation in the Cuprizone Model. **194**, 3400–3413 (2015).

279. Tsou, C. L. *et al.* Critical roles for CCR2 and MCP-3 in monocyte mobilization from bone marrow and recruitment to inflammatory sites. *J. Clin. Invest.* **117**, 902–909 (2007).

280. Yoneyama, H. *et al.* Pivotal role of dendritic cell-derived CXCL10 in the retention of T helper cell 1 lymphocytes in secondary lymph nodes. *J. Exp. Med.* **195**, 1257–1266 (2002).

281. Chen, M. J. *et al.* Extracellular signal-regulated kinase regulates microglial immune responses in Alzheimer's disease. *J. Neurosci. Res.* **99**, 1704–1721 (2021).

282. Long, Y. *et al.* Minocycline and antipsychotics inhibit inflammatory responses in BV-2 microglia activated by LPS via regulating the MAPKs/ JAK-STAT signaling pathway. *BMC Psychiatry* **23**, 1–12 (2023).

283. Lv, H. *et al.* Docosahexaenoic acid promotes M2 microglia phenotype via activating PPARγ-mediated ERK/AKT pathway against cerebral ischemia-reperfusion injury. *Brain Res. Bull.* **199**, 110660 (2023).

284. Quero, L., Hanser, E., Manigold, T., Tiaden, A. N. & Kyburz, D. TLR2 stimulation impairs anti-inflammatory activity of M2-like macrophages, generating a chimeric M1/M2 phenotype. *Arthritis Res. Ther.* **19**, 1–13 (2017).

285. Mohanraj, M., Sekar, P., Liou, H. H., Chang, S. F. & Lin, W. W. The Mycobacterial Adjuvant Analogue TDB Attenuates Neuroinflammation via Mincle-Independent PLC-γ1/PKC/ERK Signaling and Microglial Polarization. *Mol. Neurobiol.* **56**, 1167–1187 (2019).

286. Yu, Z. *et al.* Icaritin inhibits neuroinflammation in a rat cerebral ischemia model by regulating microglial polarization through the GPER–ERK–NF-κB signaling pathway. *Mol. Med.* **28**, 1–15 (2022).

287. Wu, S. Y. & Watabe, K. The roles of microglia/macrophages in tumor progression of brain cancer and metastatic disease. *Front. Biosci. (Landmark Ed.* **22**, 1805 (2017).

288. Fermi, V. *et al.* Effective Reprogramming of Patient-Derived M2-Polarized Glioblastoma-Associated Microglia/ Macrophages by Treatment with GW2580. *Clin. Cancer Res.* **29**, 4685–4697 (2023).

289. Stafford, J. H. *et al.* Colony stimulating factor 1 receptor inhibition delays recurrence of glioblastoma after radiation by altering myeloid cell recruitment and polarization. *Neuro. Oncol.* **18**, 797–806 (2016).

290. Pyonteck, S. M. *et al.* CSF-1R inhibition alters macrophage polarization and blocks glioma progression. *Nat. Med. 2013 1910* **19**, 1264–1272 (2013).

291. Butowski, N. *et al.* Orally administered colony stimulating factor 1 receptor inhibitor PLX3397 in recurrent glioblastoma: an Ivy Foundation Early Phase Clinical Trials Consortium phase II study. *Neuro. Oncol.* **18**, 557–564 (2015).

292. Lin, C.-C. *et al.* Abstract CT171: Phase I study of BLZ945 alone and with spartalizumab (PDR001) in patients (pts) with advanced solid tumors. *Cancer Res.* **80**, CT171–CT171 (2020).

293. Ransohoff, R. M. A polarizing question: Do M1 and M2 microglia exist. *Nature Neuroscience* vol. 19 987–991 (2016).

294. Gottlieb, A. *et al.* Time dependent analysis of rat microglial surface markers in traumatic brain injury reveals dynamics of distinct cell subpopulations. *Sci. Rep.* **12**, 1–10 (2022).

295. Martinez, F. O. & Gordon, S. The M1 and M2 paradigm of macrophage activation: time for reassessment. *F1000Prime Rep.* **6**, (2014).

296. Joly-Amado, A. *et al.* CCL2 Overexpression in the Brain Promotes Glial Activation and Accelerates Tau Pathology in a Mouse Model of Tauopathy. *Front. Immunol.* **11**, 997 (2020).

297. Tang, Z. *et al.* CX3CR1 deficiency suppresses activation and neurotoxicity of microglia/macrophage in experimental ischemic stroke. *J. Neuroinflammation* **11**, 1–13 (2014).

298. Xue, J. *et al.* Astrocyte-derived CCL7 promotes microglia-mediated inflammation following traumatic brain injury. **99**, 107975 (2021).

299. Gerlza, T., Nagele, M., Gschwandtner, M., Winkler, S. & Kungl, A. Designing an improved T-cell mobilising CXCL10 mutant through enhanced GAG binding affinity. *Protein Eng. Des. Sel.* **32**, 367–373 (2019).

300. Pan, Y. *et al.* Athymic mice reveal a requirement for T-cell-microglia interactions in establishing a microenvironment supportive of Nf1 low-grade glioma growth. *Genes Dev.* **32**, 491–496 (2018).

301. Solga, A. C. *et al.* RNA Sequencing of Tumor-Associated Microglia Reveals Ccl5 as a Stromal Chemokine Critical for Neurofibromatosis-1 Glioma Growth. *Neoplasia (United*

States) **17**, 776–788 (2015).

302. Tian, J. *et al.* Combined PD-1, BRAF and MEK inhibition in BRAFV600E colorectal cancer: a phase 2 trial. *Nat. Med.* **29**, 458–466 (2023).

303. Ebert, P. J. R. *et al.* MAP Kinase Inhibition Promotes T Cell and Anti-tumor Activity in Combination with PD-L1 Checkpoint Blockade. *Immunity* **44**, 609–621 (2016).

304. Pollack, I. F. *et al.* Immune responses and outcome after vaccination with glioma-associated antigen peptides and poly-ICLC in a pilot study for pediatric recurrent low-grade gliomas. *Neuro. Oncol.* **18**, 1157–1168 (2016).

305. Johnson, A. *et al.* Comprehensive Genomic Profiling of 282 Pediatric Low- and High-Grade Gliomas Reveals Genomic Drivers, Tumor Mutational Burden, and Hypermutation Signatures. *Oncologist* **22**, 1478–1490 (2017).

306. Packer, R. J. *et al.* Pediatric low-grade gliomas: Implications of the biologic era. *Neuro. Oncol.* **19**, 750–761 (2017).

307. Samstein, R. M. *et al.* Tumor mutational load predicts survival after immunotherapy across multiple cancer types. *Nature Genetics* vol. 51 202–206 (2019).

308. Bouffet, E. *et al.* Immune checkpoint inhibition for hypermutant glioblastoma multiforme resulting from germline biallelic mismatch repair deficiency. *J. Clin. Oncol.* **34**, 2206–2211 (2016).

309. Le, D. T. *et al.* Mismatch repair deficiency predicts response of solid tumors to PD-1 blockade. *Science (80-.).* **357**, 409–413 (2017).

310. Martin, A. M. *et al.* PD-L1 Expression in Pediatric Low-Grade Gliomas Is Independent of BRAF V600E Mutational Status. *J. Neuropathol. Exp. Neurol.* **79**, 74–85 (2020).

311. Cottrell, T. R. & Taube, J. M. PD-L1 and Emerging Biomarkers in Immune Checkpoint Blockade Therapy. *Cancer Journal (United States)* vol. 24 41–46 (2018).

312. Reck, M. *et al.* Pembrolizumab versus Chemotherapy for PD-L1–Positive Non–Small-Cell Lung Cancer. *N. Engl. J. Med.* **375**, 1823–1833 (2016).

313. Ansell, S. M. *et al.* PD-1 Blockade with Nivolumab in Relapsed or Refractory Hodgkin's Lymphoma. *N. Engl. J. Med.* **372**, 311–319 (2015).

314. Larkin, J. *et al.* Combined Nivolumab and Ipilimumab or Monotherapy in Untreated Melanoma. *N. Engl. J. Med.* **373**, 23–34 (2015).

315. Berry, S. & Taube, J. M. Innate vs. Adaptive: PD-L1-mediated immune resistance by melanoma. *Oncoimmunology* **4**, (2015).

316. Ribas, A. & Hu-Lieskovan, S. What does PD-L1 positive or negative mean? *J. Exp. Med.* **213**, 2835–2840 (2016).

317. Timmerman, R., Burm, S. M. & Bajramovic, J. J. An overview of in vitro methods to study microglia. *Frontiers in Cellular Neuroscience* vol. 12 242 (2018).

318. Warden, A. S. *et al.* Tools for studying human microglia: In vitro and in vivo strategies. *Brain, Behavior, and Immunity* vol. 107 369–382 (2023).

319. Mann, B. *et al.* A living ex vivo platform for functional, personalized brain cancer diagnosis. *Cell Reports Med.* **4**, (2023).

320. Ravi, V. M. *et al.* Human organotypic brain slice culture: A novel framework for environmental research in neuro-oncology. *Life Sci. Alliance* **2**, (2019).

321. Pasqualini, C. *et al.* Modeling the Interaction between the Microenvironment and Tumor Cells in Brain Tumors. *Neuron* **108**, 1025–1044 (2020).

322. Xia, T., Du, W. L., Chen, X. Y. & Zhang, Y. N. Organoid models of the tumor microenvironment and their applications. *Journal of Cellular and Molecular Medicine* vol. 25 5829–5841 (2021).

323. Wen, J. *et al.* Applications of organoid technology to brain tumors. *CNS Neuroscience and Therapeutics* vol. 29 2725–2743 (2023).

324. Liu, Y. *et al.* Patient-derived xenograft models in cancer therapy: technologies and applications. *Signal Transduction and Targeted Therapy* vol. 8 1–24 (2023).

325. Mombaerts, P. *et al.* RAG-1-deficient mice have no mature B and T lymphocytes. *Cell* **68**, 869–877 (1992).

326. Szadvari, I., Krizanova, O. & Babula, P. Athymic nude mice as an experimental model for cancer treatment. *Physiological Research* vol. 65 S441–S453 (2016).

327. Srivastava, R. *et al.* Development of a human glioblastoma model using humanized DRAG mice for immunotherapy. *Antib. Ther.* **6**, 253–264 (2023).